RCA REVIEW

a technical journal

Published quarterly by
RCA LABORATORIES
in cooperation with all subsidiaries and divisions of
RADIO CORPORATION OF AMERICA

VOLUME XXVII SEPTEMBER 1966 NUMBER 3

CONTENTS

RCA REVIEW is regularly abstracted and indexed by *Abstracts of Photographic Science and Engineering Literature, Applied Science and Technology Index, Bulletin Signalétique des Télécommunications, Chemical Abstracts, Electronic and Radio Engineer, Mathematical Reviews. and Science Abstracts* (I.E.E.-Brit.).

RCA REVIEW

BOARD OF EDITORS

GALLIUM-ARSENIDE ELECTRO-OPTIC MODULATORS*

By

T. E. Walsh

RCA Electronic Components and Devices
Princeton, N. J.

Summary—*Practical electro-optic modulators for the infrared region 0.9 to 16 microns have been constructed using large single crystals of high-resistivity GaAs. These modulators operate from d-c to several hundred megahertz and have been used to transmit television signals on infrared beams.*

The electro-optic coefficient of GaAs has been measured over the wavelength 0.9 to 16 microns at frequencies from d-c to 1.7 gigahertz. The existence of an electro-optic effect at gigahertz frequencies, together with the low value of loss tangent measured here suggests that gigahertz bandwidth microwave modulation could be achieved with GaAs. The measured microwave dielectric constant is very nearly equal to the square of the infrared index of refraction, indicating that phase matching of the infrared and microwave beams can be achieved in simple TEM transmission lines.

Introduction

THE INVENTION of the laser has renewed interest in devices for the modulation of light beams. Applications of modulated light beams include optical computers, radars, display systems, short-range wide-band terrestrial communication links, and deep-space communication systems. Laboratory uses include high-speed photography, response-time measurements of photosensitive materials and devices, and optical dispersion measurements in gases.

Electro-Optic Modulation

In the electro-optic effect, an electric field induces a change in the optical indices of refraction of a crystal. There is no satisfactory microscopic theory that predicts the magnitude of the effect from the crystal properties, although Heilmeier[1] has presented a theory for the molecular crystal hexamethylenetetramine that gives good agreement

* The work reported here was sponsored by the National Aeronautics and Space Administration, Goddard Space Flight Center, Greenbelt, Md., under Contract NAS5-10144, and NAS5-9620 and by the Electronic Technology Division, Air Force Avionics Laboratory, Research and Technology Division, Air Force Systems Command, Wright Patterson Air Force Base, Ohio, under Contract AF33 (615)-1096.

[1] G. Heilmeier, "The Dielectric and Electro-Optical Properties of the Molecular Crystal Hexamine," *Appl. Optics*, Vol. 3, p. 1281, Nov. 1964.

with the observed value. There is, however, a complete phenomenological theory[2] so that once the electro-optic coefficients of a material are measured, the effect of an electric field in the crystal on the transmittance of a light beam through the crystal can be predicted for any orientation of the crystal axes with respect to both the electric field and the light beam. A review of the theory for cubic crystals such as gallium arsenide is given by Namba[3] and by Sterzer et al.[4]

A cubic electro-optical crystal such as GaAs is optically isotropic in the absence of an electric field. The application of an electric field along certain crystal directions causes the crystal to become birefringent by an amount proportional to the electric field. The crystal is therefore an optical wave plate with a voltage-controlled retardation and can be used in various optical systems to electrically modulate the intensity, phase, or polarization of a light beam. Three such configurations are shown in Figure 1.

The following physical properties of an electro-optic crystal are important for modulators such as those of Figure 1.

(1) The index of refraction N, which determines the speed of light in the crystal and the reflection loss at its surfaces.

(2) The relative dielectric constant K, which determines the capacitance of the crystal and the speed of propagation of electric fields in the crystal.

(3) The electro-optic coefficient r_{41}, which relates the induced birefringence ΔN to the applied electric field E. For the modulators of Figures 1(a) and 1(c), $\Delta N = N^3 r_{41} E$. For the moduluator of Figure 1(b), $\Delta N = (1/2) N^3 r_{41} E$.

(4) The optical absorption coefficient k, which determines the optical loss in the crystal.

(5) The dielectric loss tangent, tan δ, which determines the electrical loss in the crystal.

(6) The crystal strain, which must be low to allow a cooperative electro-optic effect in adjacent areas of the crystal.

(7) The "hardness," which determines the resistance of the crystals to straining during cutting and polishing.

(8) The solubility, which determines the ability to withstand moist ambient conditions.

---

[2] W. P. Mason, "Optical Properties and the Electro-Optic and Photoelastic Effects in Crystals Expressed in Tensor Form," *Bell System Tech. Jour.*, Vol. 29, p. 161, April 1950.

[3] S. Namba, "Electro-Optical Effect of Zincblende," *Jour. Opt. Soc. Amer.*, Vol. 51, p. 76, Jan. 1961.

[4] F. Sterzer, D. Blattner, and S. Miniter, "Cuprous Chloride Light Modulators," *Jour. Opt. Soc. Amer.*, Vol. 34, p. 62, Jan. 1964.

(9) The thermal conductivity, which determines the deleterious birefringence due to thermal gradients in a crystal heated by electrical or optical absorption.

The values of these parameters for the GaAs crystals used here are discussed in the next section.

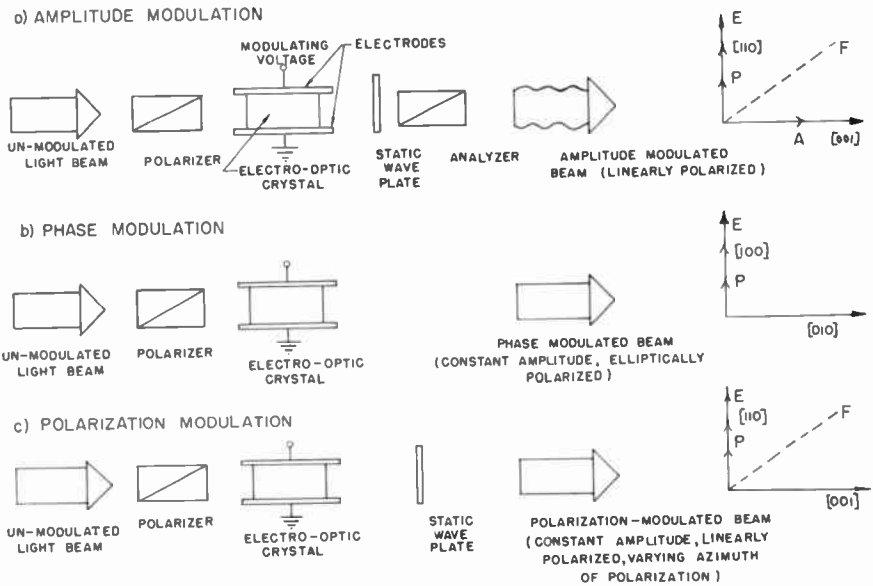

Fig. 1—Optical systems for producing (a) amplitude modulation (b) phase modulation (c) polarization modulation using an electro-optic crystal. The diagrams at the right indicate the orientation of the crystal axes relative to the electric field E, the polarizer azimuth P, the analyzer azimuth A, and the fast axis of the waveplate F, as seen looking in the direction of the light beam.

Crystal Growth and Properties

Growth

The crystals are "boat grown" in a horizontal Bridgman furnace from elemental gallium and arsenic. They are doped with iron during growth to raise their resistivity above 10^6 ohm-cm over the entire length of the ingot. A typical ingot and a modulator crystal cut from the ingot are shown in Figure 2. The ingot is 1½ cm in diameter and 8 cm long. It has been seeded to make most of its length useful for modulator crystals. The crystals are hard, nonhygroscopic, and possess a relatively high thermal conductivity. They are virtually strain free

as grown and are easily cut and polished flat to 1/10 wavelength of visible light without introducing appreciable strain. The extinction ratio of 1-cm-thick crystals between crossed polarizers is greater than 100 to 1 after all cutting and polishing operations, and additional strain is not introduced by normal handling. Since the crystals are insoluble in water and dissociate at 800°C, no special precautions are necessary with regard to ambient temperature and humidity.

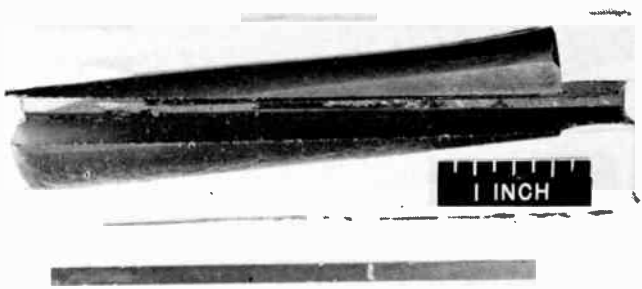

Fig. 2—Ingot of high-resistivity GaAs and a modulator crystal cut from the ingot.

Optical Properties

The crystals are opaque in the visible region, but are transparent in the infrared between 0.9 and 16 microns. The excellent optical quality of the crystals in the infrared is illustrated in Figure 3, which is a photograph of a GaAs crystal on a metal scale. The photograph was taken with the aid of an infrared image converter sensitive to wavelengths near 1 micron. The optical quality is comparable to that of good optical glass.

The optical absorption coefficient k was determined by measuring the transmittance of a crystal that was polished on four faces to provide two unequal path lengths through the crystal. This permits correction for the reflection losses that are equal for the two directions. The absorption coefficient determined in this manner is shown as a with three cavities at frequencies of 2.5, 5.6, and 10 gigahertz. No

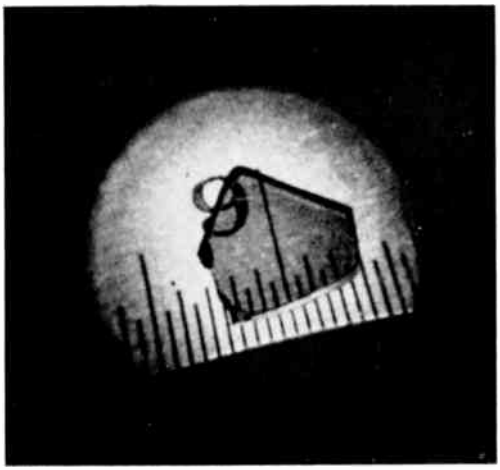

Fig. 3—Infrared photograph of a GaAs crystal on a metal scale.

function of wavelength in Figure 4. The smallest absorption coefficient that could be measured on the spectrometers used was 0.01 cm^{-1}.

At those wavelengths where negligible absorption exists, reflection losses limit the external transmittance of a plane-parallel plate of GaAs to 55%. This low transmittance is due to the high index of refraction of GaAs, as shown in Figure 5. The external transmittance T is given in terms of the refractive index N by the expression

$$T = 2N/(N^2 + 1). \tag{1}$$

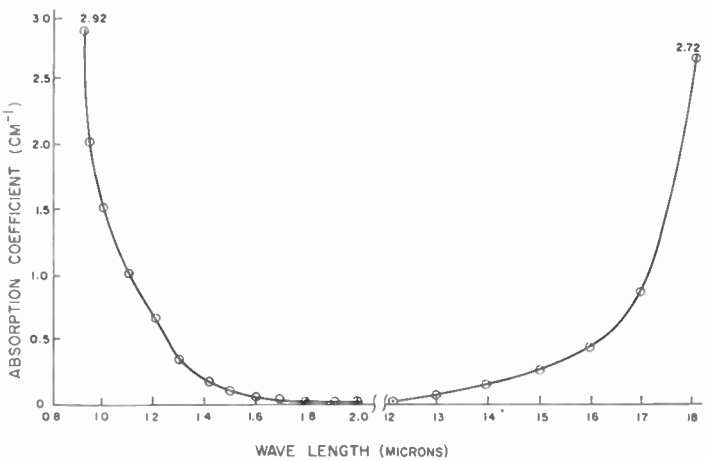

Fig. 4—Absorption coefficient of GaAs versus wavelength.

This transmittance has been increased to over 99% by anti-reflection coating for operation at a single wavelength.

Electrical Properties

The dielectric constant and loss tangent were measured at microwave frequencies by a resonant cavity perturbation technique.[5] Samples of GaAs were inserted into a resonant cavity, causing a change in the resonant frequency and cavity Q. The change in resonant frequency is related to the crystal dielectric constant and the change in cavity Q is related to the loss tangent. The measurements were made

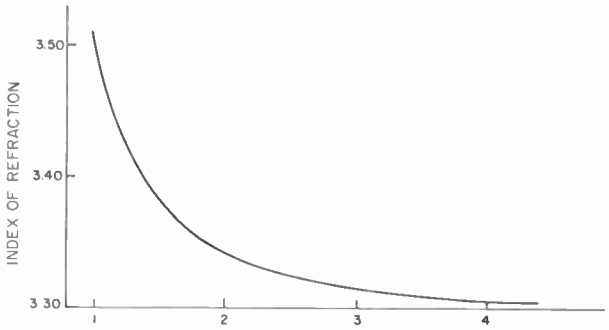

Fig. 5—Index of refraction of GaAs versus wavelength.

with three cavities at frequencies of 2.5, 5.6, and 10 gigahertz. No change in either the dielectric constant or loss tangent was observed over this frequency range. The relative dielectric constant was 11.0 and the loss tangent was 0.001. This value of loss tangent gives a microwave resistivity in agreement with the observed d-c resistivity of the crystals.

Electro-Optic Coefficient

The unclamped electro-optic coefficient r_{41} of GaAs was measured in the wavelength range 0.9 to 2.5 microns by placing the crystal between parallel polarizers and measuring the decrease in transmittance when a d-c voltage was applied to the crystal. In this case, the transmittance is given by

$$T = T_0 \cos^2 \phi$$

where

$$\phi = \frac{2\pi l}{\lambda} N^3 r_{41} \frac{V}{d}$$

[5] N. Ogasawara and Y. Shikata, "Improved Permittivity and Permeability Measurements," *Microwaves*, Oct. 1962.

is the retardation of the GaAs crystal with voltage V applied. In these equations,

T = transmittance with voltage V applied

T_0 = transmittance when $V = 0$

N = index of refraction at wavelength λ

d = crystal thickness in the direction of the electric field

l = crystal length in the direction of the light beam.

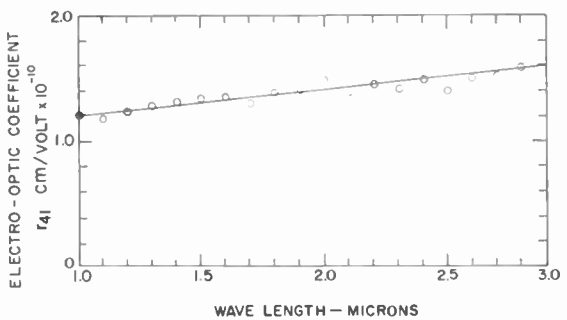

Fig. 6—Electro-optic coefficient r_{41} of GaAs in the wavelength range 1 to 3 microns.

The solution of these equations for r_{41} is

$$r_{41} = \frac{\lambda d}{2\pi l V N^3} \sin^{-1} \sqrt{\frac{T_0 - T}{T_0}}. \tag{2}$$

The values of r_{41} calculated from Equation (2) are shown in Figure 6. Although the refractive index changes considerably in this region, r_{41} remains nearly constant. These results may be compared with those of Buhrer and Ho,[6] who obtained values of r_{41} ranging from 0.29 to 1.7×10^{-10} cm/v at wavelengths between 1.0 and 1.7 microns.

The sensitivity of the preceding method of measurement decreases as the wavelength increases because the change in transmittance $T_0 - T$ decreases with wavelength for a fixed voltage V. For wavelengths greater than 2.5 microns, the following method was used. The

[6] L. Ho and C. Buhrer, "Electro-Optic Effect of Gallium Arsenide," *Appl. Optics*, Vol. 2, p. 647, 1963.

GaAs crystal was placed between parallel polarizers as before, but a thick wave plate of CdS was also placed between the parallel polarizers and oriented with its fast axis at 45° to the plane of passage of the polarizers. The phase retardation produced by the CdS wave plate was 5/4 wavelength at 9.0 microns, 7λ/4 at 7.1 microns, 9λ/4 at 5.6 microns, and so on toward shorter wavelengths. At these wavelengths. the transmittance of the configuration is given by

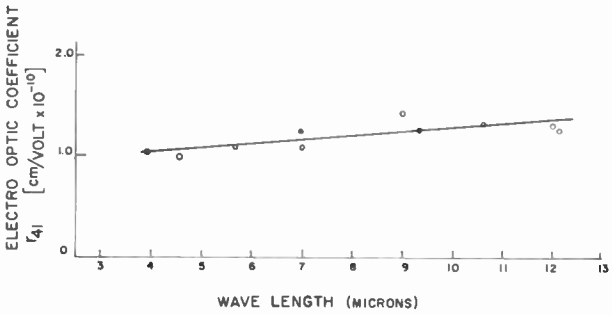

Fig. 7—Electro-optic coefficient r_{41} of GaAs in the wavelength range 4 to 12 microns.

$$T = T_0 \cos^2\left[\frac{\phi}{2} + (2M+1)\frac{\pi}{4}\right] (M = 1,2,3,4,\cdots)$$

$$= \frac{1}{2} T_0 \left\{1 + \cos\left[\phi + (2M+1)\frac{\pi}{2}\right]\right\}$$

$$= \frac{1}{2} T_0 (1 + \sin\phi).$$

The change in transmittance $T - (T_0/2)$ is proportional to $\sin\phi$ instead of $\cos^2\phi$ as in the preceding method. For small values of ϕ this means a larger change in transmittance to offset the decrease due to the longer wavelength. These equations are solved for r_{41}:

$$r_{41} = \frac{\lambda d}{2\pi l V N^3} \sin^{-1}\left[\frac{T - \frac{T_0}{2}}{\frac{T_0}{2}}\right]. \qquad (3)$$

The values of r_{41} obtained by this method are shown in Figure 7.

The measurements of r_{41} versus wavelength shown in Figures 6 and 7 were made with d-c voltages applied to the crystals. The dependence of r_{41} on the frequency of the modulating electric field was determined at the fixed infrared wavelength of 1 micron using the configuration shown in Figure 1(a). The modulating frequency was varied from d-c to 20 MHz and the modulation was detected with a 7102 photomultiplier terminated with a 50-ohm resistor. The observed modulation was constant over this frequency range except near the piezoelectric resonances of the crystal. At a resonance the modulation increases by about three orders of magnitude due to the photoelastic contribution, so that only about one volt of modulating signal is required to change the transmittance of a modulator from zero to 100%. The magnitude of the electro-optic effect above the resonance is the same as the value below the resonance, i.e., the clamped and unclamped electro-optic coefficients are the same.

In addition, a microwave measurement of r_{41} was made at 2.36 microns on a GaAs crystal in a re-entrant cavity resonant at 1.7 GHz. The crystal was placed between crossed polarizers and the micro-wave signal was amplitude modulated at 1000 cps. With this arrangement, the modulated infrared beam leaving the cavity contained a 1000 Hz signal component, which was detected with a slow but sensitive PbS infrared detector. The peak microwave voltage across the crystal was calculated from the equation,

$$V = 27.5 \left[\frac{b_1}{\lambda_0} PQ \ln \frac{a_1}{a_2} \right]^{1/2} \quad \text{volts.} \tag{4}$$

In this equation, P is the rms power in watts absorbed in the cavity, λ_0 is the free-space resonant wavelength of the cavity, a_1 is the inside diameter of the cavity, a_2 is the diameter of the cavity post, b_1 is the cavity height, and Q is the cavity Q. The value of r_{41} calculated from the observed modulation and the voltage given by Equation (4) was 0.94×10^{-10} cm/v, in good agreement with the low-frequency results.

Design Equations and Modulator Performance

In this section the design equations for electro-optic amplitude modulators are presented and the performance data for two modulators are given.

Design Equations

The basic question concerning an electro-optic modulator is what voltage is required to produce a given change in transmittance. For

the configuration shown in Figure 1(a), the transmittance is given by

$$T = T_0 \sin^2 \left[\frac{\phi}{2} + \frac{\psi}{2} \right] \tag{5}$$

where ψ is the static retardation of the wave plate. The factor T_0 includes the effects of any reflection and absorption losses in the crystal, polarizers, and wave plate. The greatest change in T for small values of V occurs when $\psi = \pi/2$. This can be seen by taking the derivative of T with respect to V in Equation 5 and then finding the maximum value of this derivative as a function of ψ. This maximum occurs for $\phi + \psi = \pi/2$. For ϕ small compared to ψ, as it must be to avoid distortion in the modulation, this reduces to $\psi = \pi/2$. This value of ψ gives not only the greatest sensitivity, but also the greatest linearity, since it is an inflection point on the T versus ϕ curve. With $\psi = \pi/2$, Equation (5) becomes

$$\frac{T - \frac{T_0}{2}}{\frac{T_0}{2}} = \sin \phi. \tag{6}$$

The left side of Equation (6) is the modulation index[7] m of the amplitude modulated beam. In terms of the crystal parameters and the voltage,

$$m = \sin \frac{2\pi N^3 r_{41} l}{\lambda d} V. \tag{7}$$

Equation (7) shows that the depth of modulation decreases as the wavelength increases. It also shows that the decrease may be offset by using a crystal with a larger length-to-width ratio l/d. The final point to be made is that the relatively low value of r_{41} for GaAs is compensated for by its large index of refraction, which is cubed in Equation (7).

Modulator Construction and Performance

Figure 8 is a cross-sectional drawing of a GaAs modulator designed to operate in the range 0.9 to 3 microns. The GaAs crystal is mounted

[7] F. Terman, *Electronic and Radio Engineering*, p. 523, McGraw-Hill Book Co., Inc., New York, 1955.

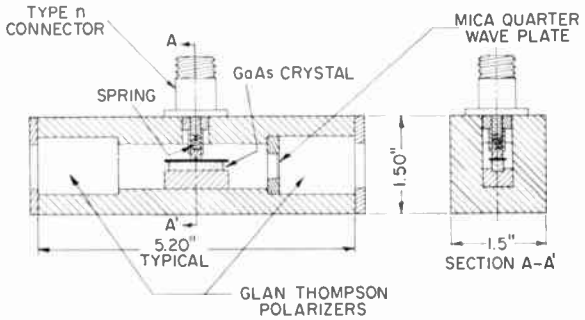

Fig. 8—Cross section of the J2036 infrared modulator for the wavelength range 1 to 3 microns.

between spring-loaded parallel plates at the end of a 50-ohm coaxial transmission line and presents a 3-picofarad capacitive load to the line. The polarizer and analyzer are 1-cm-aperture calcite Glan–Thompson prisms and the quarter-wave plate is mica. The aluminum body of the modulator encloses the crystal to minimize radiation of the modulating signal. A photograph of the modulator is shown in Figure 9.

The performance of this modulator as a function of infrared wavelength is shown in Figure 10. The crystal used to obtain these data was 1.7 cm long with a 3 × 3 mm aperture, and the wave plate gave a quarter-wave retardation at 1.2 microns. The lower curve of Figure 9 shows the effect on the transmittance of the modulator produced by 600-volt d-c of each polarity. The upper graph shows the difference between the transmittance for +600 volts and —600 volts, which cor-

Fig. 9—Photograph of the J2036 infrared modulator (dimensions: 1.5 × 2.3 × 5.2 inches).

responds to an a-c signal of 425 volts rms. Except for a piezoelectric resonance at 700 kilohertz, the modulator response was observed to be flat from d-c to 20 MHz. It is expected that the frequency response should extend to several hundred megahertz. A modulator similar in construction to this one was successfully used to transmit a television picture on an infrared beam.[8]

The upper limit to the operating wavelength of the preceding modulator was set by absorption in the calcite polarizers and the mica

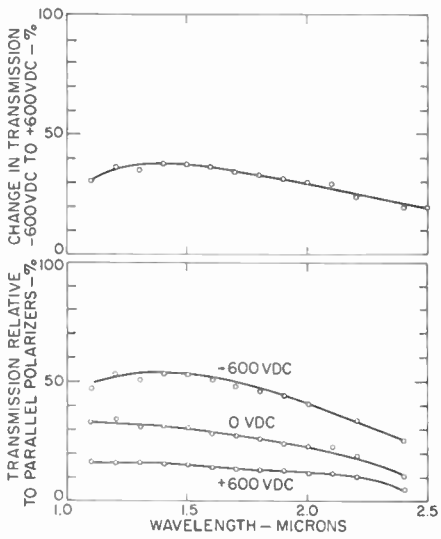

Fig. 10—Performance of the J2036 modulator. The lower curve shows the effect on the transmittance produced by 600 volts of each polarity. The upper curve shows the difference between the transmittance for +600 volts and —600 volts.

wave plate. A modulator designed for operation in the range 2 to 12 microns is shown in Figure 11. The GaAs crystal is 3 × 3 mm in cross section and 6.7 cm long. Each polarizer consists of two plates of high-resistivity germanium set at Brewster's angle. Two plates are sufficient to polarize over 99% of the incident radiation because of the high index of refraction of germanium ($N = 4$). The wave plate is CdS. The electrodes are insulated from the aluminum body of the modulator and their position allows the modulator to be connected directly between the plate terminals of two push–pull output tubes of the driving amplifier. The total capacitance of the modulator is 14

[8] J. Bordogna, W. Hannan, T. Penn, and T. Walsh, "Electro-Optic TV Communications System," *Proc. IEEE*, Vol. 53, p. 171, Feb. 1965.

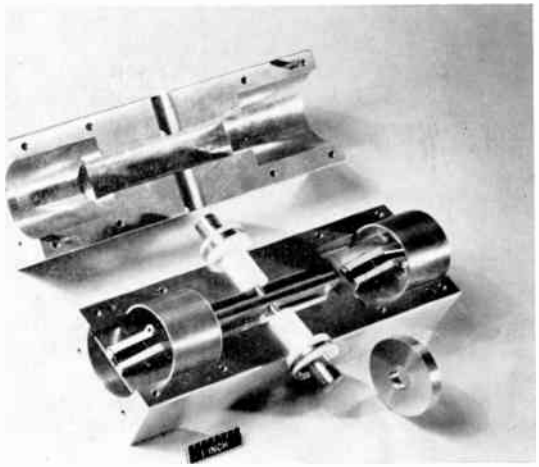

Fig. 11—Photograph of the J2036A infrared modulator. For clarity, the covers of the polarizers have been cut away and the wave plate has been removed and placed beside the body of the modulator.

picofarads. The performance of the modulator is illustrated in Figure 12, which shows the depth of modulation for a peak applied signal of 600 volts.

This modulator has been used to amplitude modulate the output of a 10 watt CO_2 gas laser operating continuously at 10.6 microns. A modulation depth of 70% was obtained with 1000-volt-peak modulating signal. The upper limit to the operating wavelength of this modulator is set by absorption in the GaAs. An upper wavelength limit of 16 microns has been attained using shorter crystals at the expense of higher modulating voltage.

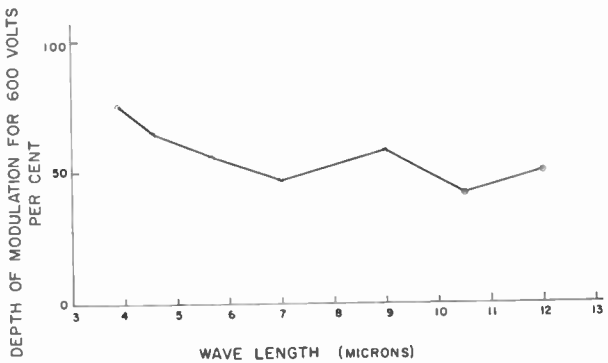

Fig. 12—Performance of the J2036A infrared modulator. The depth of modulation versus wavelength is shown for a peak applied signal of 600 volts.

AVALANCHE AND TUNNELING CURRENTS IN GALLIUM ARSENIDE*

By

Richard Williams

RCA Laboratories
Princeton, N. J.

Summary—Curves have been computed for avalanche multiplication and Zener tunneling for gallium arsenide specimens of various thicknesses. There are two cleanly separated regions based on specimen thickness. For thicknesses greater than about 10^{-4} cm, avalanche multiplication is the predominant process. For thinner specimens, tunneling predominates. Results are presented in a form that facilitates analysis of a wide variety of experimental results.

Introduction

There are increasing applications for devices in which a semiconductor is maintained at a field near dielectric breakdown. Examples of these are semiconductor particle counters and avalanche-transit-time diodes. The ultimate dielectric breakdown is most frequently due either to impact ionization multiplication of hot carriers or to Zener tunneling of electrons from valence band to conduction band. Which of these mechanisms predominates in a given case depends on the material and the experimental conditions, particularly the sample dimensions.[1,2] For a proper understanding of experimental data it is necessary to know the source of the breakdown current. For gallium arsenide sufficient data are available to calculate both the avalanche current and the tunneling current for various specimen thicknesses. It will be seen that there is a fairly sharp division between specimens in which avalanche multiplication predominates and those in which tunneling predominates, depending on the specimen thickness. The results of these calculations are presented here in a form that, it is believed, will facilitate analysis of a variety of experimental results.

* The research reported in this paper was sponsored by the United States Army Electronics Command, Fort Belvoir, Va., under Contract No. DA 44-009-AMC-1276(T) and RCA Laboratories, Princeton, N. J.

[1] A. G. Chynoweth and K. G. McKay, "Internal Field Emission in Silicon P-N Junctions," *Phys. Rev.*, Vol. 106, p. 418, May 1, 1957.

[2] R. Williams, "Dielectric Breakdown in Cadmium Sulfide," *Phys. Rev.*, Vol. 125, p. 850, Feb. 1, 1962.

Avalanche Multiplication

We shall consider the avalanche multiplication of carriers passing through a Schottky barrier or its equivalent, a step junction. This situation is close to what is found in many experimental cases and has the advantage of being analytically tractable.

The multiplication, M, experienced by a carrier passing through a region of thickness, W, in which there is a high electric field, $E(x)$, is related to the ionization rate, $\alpha(E)$, by the equation[3]

$$1 - \frac{1}{M} = \int_0^W \alpha(E)\, dx. \tag{1}$$

The ionization rate, $\alpha(E)$, has been determined experimentally.[4-6] The assembled data presented in Reference (6) may be fitted closely by the empirical equation

$$\alpha(E) = A \exp(-b/E) \quad \text{cm}^{-1} \tag{2}$$

where $A = 1.0 \times 10^6$ cm^{-1} and $b = 1.72 \times 10^6$ volts/cm. This equation holds over the range of fields from 2.0×10^5 to 8.0×10^5 volts/cm, which is the range of interest here. A theoretical model giving this form of field dependence for $\alpha(E)$ has been described by Shockley.[7] We assume throughout that the value of $\alpha(E)$ is the same for both holes and electrons.

The integral in Equation (1) may be evaluated by making use of the fact that, in a Schottky barrier or step junction, the field is a linear function of distance.[8] In particular,

$$E(x) = \frac{E_m x}{W}. \tag{3}$$

---

[3] K. G. McKay, "Avalanche Breakdown in Silicon," *Phys. Rev.*, Vol. 94, p. 877, May 15, 1954.

[4] R. A. Logan, A. G. Chynoweth, and B. G. Cohen, "Avalanche Breakdown in Gallium Arsenide P-N Junctions," *Phys. Rev.*, Vol. 128, p. 2518, Dec. 15, 1962.

[5] M. Weinstein and A. I. Mlavsky, "The Voltage Breakdown of GaAs Abrupt Junctions," *Appl. Phys. Letters*, Vol. 2, p. 97, 1 March 1963.

[6] H. Kressel, *Int. Jour. Elec.* (to be published).

[7] W. Shockley, "Problems Related to p-n Junctions in Silicon," *Solid-State Electronics*, Vol. 2, No. 1, p. 35, 1961.

[8] H. K. Henisch, *Rectifying Semiconductor Contacts*, p. 179, Oxford Univ. Press, New York, 1957.

Here E_m is the maximum field at one end of the high-field region and x is measured from the other end where the field goes to zero. Combining Equations (1), (2) and (3), we obtain

$$dx = \frac{W}{E_m}\, dE,$$

and

$$\int_0^W \alpha(E)\, dx = \frac{AW}{E_m} \int_0^{E_m} e^{-b/E}\, dE = I(E_m) \tag{4}$$

$$I(E_m) = AW \left\{ e^{-b/E_m} + \frac{b}{E_m}\, \mathcal{E}i\left(-\frac{b}{E_m}\right) \right\}. \tag{5}$$

$\mathcal{E}i(-b/E_m)$ is the exponential integral defined as

$$-\mathcal{E}i(x) = \int_x^\infty \frac{e^{-u}}{u}\, du.$$

Using tabulated numerical values of the integral[9] we can obtain M as a function of E_m for various values of W. These values of W correspond to Schottky barriers in crystals having different free-carrier concentrations.

Figure 1 shows plots of M as a function of E_m for four different values of W. Strictly speaking, in a given specimen, W is a weak function of the field so that the curve shown for a fixed thickness could not actually refer to a single specimen. Since the range of field covered by a given curve is rather small, no serious distortion is introduced by thinking of each curve as referring to a single specimen with an average thickness corresponding to the range of field covered.

Zener Tunneling

The Zener tunneling current may be estimated from a formula cited by Chynoweth;[10]

---

[9] *Tables of Sine, Cosine and Exponential Integrals*, Vol. II, National Bureau of Standards, 1940.

[10] A. G. Chynoweth, "Internal Field Emission," *Progress in Semiconductors*, Vol. 4, p. 97, John Wiley & Sons, Inc., New York, 1960.

$$j = \frac{zq^2EW}{a^2h} f, \tag{6}$$

where z is the number of electrons/unit cell, q is the charge on the electron, a is the unit cell dimension, h is Planck's constant, and

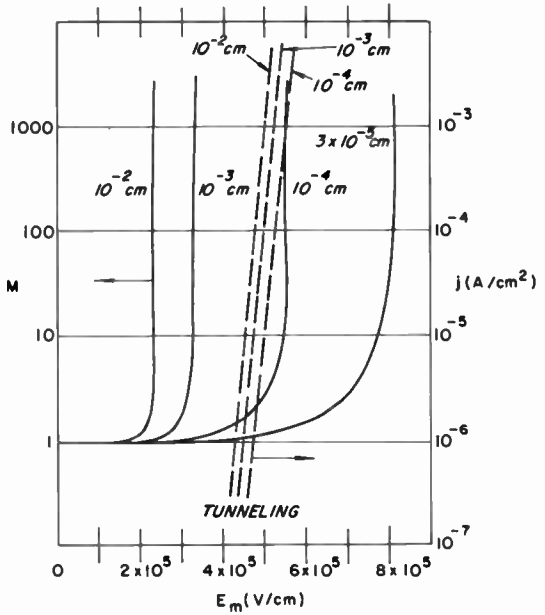

Fig. 1—Curves of multiplication versus field for different specimen thicknesses calculated for gallium arsenide. Also shown are curves of current density versus field for Zener tunneling in GaAs for different specimen thicknesses. Dashed lines show tunneling-current densities, and solid lines show avalanche multiplications.

$$f = \exp\left(-\frac{\pi^2\sqrt{2m^*}}{2qh}\frac{\epsilon_i^{3/2}}{E}\right), \tag{7}$$

where m^* is electron effective mass and ϵ_i is the forbidden energy gap. Equation (6) applies to a slab of material of thickness W in which there is a uniform field, E. Putting the numerical values of the constants into Equation (6) give the following expression for j:

$$\log_{10} j = \log_{10}(5.3\times10^{10}\times EW) - 1.75\times10^7\left(\frac{m^*}{m}\right)^{1/2}\frac{\epsilon_i^{3/2}}{E}, \tag{8}$$

where j is in amperes cm^2, E in volts/cm, W in cm, and ϵ_i in eV.

The tunneling current is proportional to the specimen thickness because the total number of electrons available for tunneling is proportional to the thickness. All electron–hole pairs created anywhere in the volume are collected at the electrodes. For the case of the Schottky barrier it is possible to consider the material within the barrier to be made up of thin slabs of material of thickness dW, each with the appropriate field. Since the total current is the result of adding up contributions from each such element of volume within the barrier, it is possible to integrate the exponential tunneling function over the field distribution found in the Schottky barrier as was done with the similar function in Equation (5).

Tabulated values of the exponential integral are not available, however, over the range of values required to obtain numerical results. For this reason we resort to an approximation as follows. It is assumed that all the tunneling takes place within the last ten per cent of the Schottky barrier at the end where the field is highest. This region is the effective specimen thickness, and it is further assumed that the field is uniform within this region and equal to the maximum value at the surface. Used with Equation (6), this effective thickness permits an estimate of the tunnel-current density for a high-field region having a *total* thickness ten times as large. It is the total thickness that is used to label the curves in Figure 1. Thus tunneling and avalanche curves both refer to the same total thicknesses. From Equation (6), it is seen that the tunneling-current density is proportional to the specimen thickness. In GaAs, the effective mass ratio is[11] 0.072 for electrons and 0.085 for holes, and the room temperature energy gap is 1.4 eV. Using these values we obtain the tunneling-current density as a function of E_m for several specimen thicknesses. These values are compared with the avalanche curves in Figure 1. The avalanche curves are given as pure numbers and may be compared directly with the tunneling curves by choosing the unit of current density to be 1 microampere/cm^2 at low fields, where $M = 1$.

Conclusions

As can be seen from Figure 1, there is a rather sharp division between specimens in which tunneling predominates and specimens in which impact ionization multiplication predominates. By a proper choice of specimen thickness, either process may be favored. This has been discussed in earlier works,[1,2] but is rarely considered explicitly in discussions of high-field devices, where the breakdown is usually assumed without detailed argument to proceed purely by one mechanism or the other.

[11] O. Madelung, *Physics of 3-5 Compounds*, p. 352, John Wiley and Sons, New York, 1964.

AUTOMATIC DISPLAY OF MIS CAPACITANCE VERSUS BIAS CHARACTERISTICS

By

KARL H. ZAININGER

RCA Laboratories
Princeton, N. J.

Summary—This paper describes instrumentation that permits the automatic and rapid measurement of capacitance-versus-bias characteristics of metal–insulator–semiconductor MIS structures at 1 MHz over a wide range of biases and sweep speeds and under a variety of experimental conditions. The instrument is a valuable tool in research on insulator–semiconductor interfaces. The apparatus consists primarily of standard laboratory equipment, does not require a phase-sensitive detector, is easily assembled and tested, and provides a graphic output.

INTRODUCTION

AN MIS capacitor (or diode) can be defined as a structure consisting of an n or p-type semiconductor covered by a thin film of insulating material (often oxide), with a metal electrode* on top of the insulator and an ohmic contact to the semiconductor. Such devices can be important research tools because their capacitance-versus-bias (C-V) characteristics contain information about the surface states† present in the device.[1-5] Because of the ease

---

* The metal electrode is often referred to as the gate to conform with MIS transistor terminology.

† The term *surface states* is used here in a completely operational manner; it lumps together the effect of work-function difference and oxide charge, as well as interface states, i.e., traps and disorder within the interface region.

[1] L. M. Terman, "An Investigation of Surface States at a Silicon/Silicon Oxide Interface Employing Metal-Oxide-Silicon Diodes," *Solid-State Electronics*, Vol. 5, p. 285, Sept.-Oct. 1962.

[2] K. Lehovec, A. Slobodskoy, and J. L. Sprague, "Field-Effect-Capacitance Analysis of Surface States on Silicon," *Physica Status Solidi*, Vol. 3, p. 447, No. 3, 1963.

[3] K. Lehovec and A. Slobodskoy, "Impedance of Semiconductor-Insulator-Metal Capacitors," *Solid-State Electronics*, Vol. 7, p. 59, Jan.-Feb. 1964.

[4] K. H. Zaininger and G. Warfield, "Limitations of the MOS Capacitance Method for the Determination of Semiconductor Surface Properties," *Trans. IEEE Electron Devices*, Vol. ED-12, p. 179, April 1965.

[5] A. S. Grove, B. E. Deal, E. H. Snow, and C. T. Sah, "Investigation of Thermally Oxidized Silicon Surfaces Using Metal-Oxide-Semiconductor Structures," Solid-State Electronics, Vol. 8, p. 145, Feb. 1965.

of fabrication, simplicity of structure, and the sensitivity of the *C-V* characteristics to physical properties, MIS capacitors can advantageously be used as a test vehicle for the study of the influence of process parameters on properties of insulating films on semiconductors, and insulator–semiconductor interfaces.

Capacitance-versus-bias measurements are normally carried out on a point-by-point basis using a capacitance bridge. To get meaningful results and reasonable accuracy, the capacitance of each diode must be determined for many different bias settings, and many diodes on a wafer must be investigated to get statistically significant data. Then the data must be plotted. Such a procedure is extremely cumbersome, time-consuming, and subject to error. The instrumentation described in the present paper allows the automatic and rapid measurement of the continuous MIS capacitance-versus-bias characteristics at 1 MHz over a wide range of biases and sweep speeds. It has a range of 500 pF/inch to 0.1 pF/inch, an accuracy better than 2%, provides a graphical output, does not require a phase-sensitive detector, and can be built from standard laboratory equipment.

The theory of the high-frequency MIS capacitance method for the determination of surface states is first briefly summarized. The principle of operation of the measuring equipment is then discussed, followed by a description of the circuitry and the various modes of operation.

Determination of Surface States by *C-V* Measurements

The small-signal differential admittance of an ideal MIS capacitor, i.e., one with an ideal insulating film and no surface states, consists of the insulator capacitance,* C_i, in series with the surface space-charge-layer capacitance,[1,6] C_{sc}. C_i is independent of frequency as is C_{sc} in the accumulation and depletion regimes (up to 10^{11} Hz). In the inversion regime, however, C_{sc} takes on different forms depending on whether or not the minority carriers can follow the applied a-c and/or d-c signals. The dependence of this ideal MIS capacitance on effective bias is shown in Figure 1 for the case of an Me-SiO_2–Si structure. In all cases this capacitance is uniquely determined by the semiconductor surface potential, ψ_s. For an actual MIS diode in which surface states

* Throughout this paper, except where specifically mentioned otherwise, all surface charges, surface-state densities, and capacitances are for unit area.

[6] K. H. Zaininger, "Semiconductor Surface Physics," pp. 17-56 in *Field Effect Transistors*, ed. by J. T. Wallmark and H. Johnson, Prentice Hall, Inc., Englewood Cliffs, N. J., 1966.

are present but in which loss mechanisms are neglected, the above equivalent circuit is modified by adding the surface-state capacitance, C_{ss}, in parallel with C_{si}. The dependence of C_{ss} on frequency and surface potential is a function of the density of surface states and their spatial and energy distribution. Since the density and distribution are, in general, not known, little information about the physical prop-

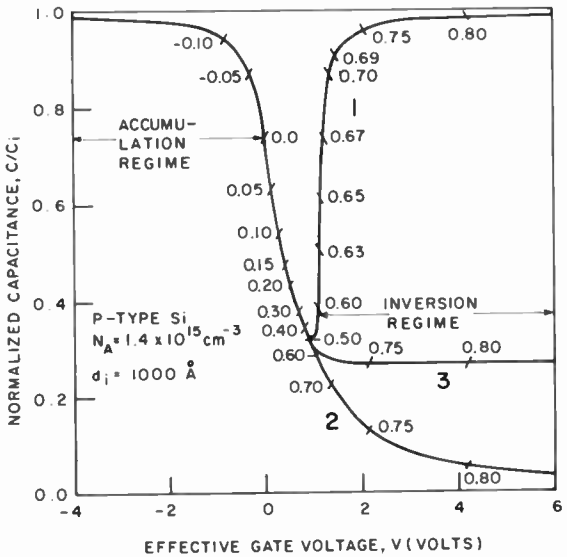

Fig. 1—Normalized MIS capacitance versus gate voltage for the case of no surface states. In the inversion regime curve (1) holds if the minority carriers follow both a-c and d-c signals, curve (2) if they cannot accumulate at the surface (Schottky depletion layer capacitance), curve (3) if they follow d-c but not a-c signals. The value of the silicon surface potential is shown for several values of capacitance.

erties of the interface can be obtained from an analysis of the MIS C-V characteristics obtained at an arbitrary frequency. However, if the measurement frequency is sufficiently high so that surface states cannot follow† ($f \gtrsim 50$ MHz), then the surface-state capacitance becomes zero and the MIS capacitance reduces to its high-frequency form,

† It has been established by W. L. Brown (*Phys. Rev.*, Vol. 91, p. 518, 1953) that 50 MHz is sufficiently high so that surface states cannot follow. In our own work we find that, in most cases, 1 MHz satisfies this condition, especially for p-type samples. For some n-type samples with states close to the conduction band, an operating frequency up to 50 MHz might be necessary. The present apparatus can be modified to operate at higher frequencies, but only at the expense of a reduced range, increased difficulty in calibration, and more care in experimental conditions and operation.

i.e., the series combination of C_i and C_{ss}. When this condition is satisfied, then the MIS capacitance is unambiguously related to the semiconductor surface potential. However, there is a difference between an experimentally determined high-frequency C-V characteristic and one computed for an identical structure without surface states, and that is the voltage due to the total charge in surface states. By finding the difference between the measured voltage for a given capacitance (and thereby ψ_s) and its "ideal" value, ΔV, one can determine the

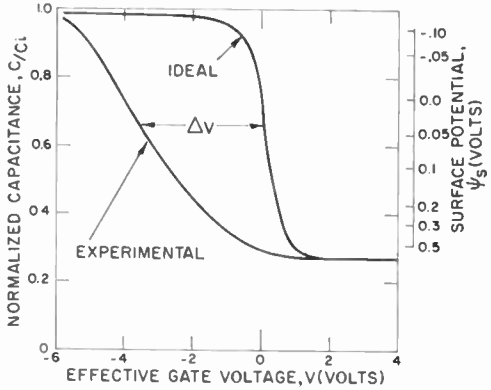

Fig. 2—Comparison between experimental and ideal C-V curves for the structure described in Figure 1.

total charge that can be trapped in surface states during the measurement period and the surface-state density as a function of ψ_s (or energy). The effective density of surface states, as reflected to the insulator–semiconductor interface, N_{ss}, is then given for any particular value of capacitance (and thereby ψ_s) as

$$N_{ss} = \frac{C_i \Delta V}{1.6 \times 10^{-19}} = \frac{\epsilon_i \Delta V}{1.6 \times 10^{-19} d_i}. \qquad (1)$$

where ϵ_i and d_i are the insulator dielectric constant and thickness, respectively. If the experimental curve is to the left of the ideal one, the charge in surface states is positive; if it is to the right, the charge is negative. A typical example of a comparison between experimental and ideal curves is shown in Figure 2.

In the past, the use of the MIS capacitance method in the study of surface properties has involved various approximations and assump-

tions that are not always justified. However, it has been shown[4,7] that MIS capacitance measurements can yield interesting and meaningful results if the proper experimental conditions are established, and if care is taken in the interpretation of the experimental results. Some specific applications of MIS capacitance-versus-bias measurements are described in the appendices.

Principle of Operation

The basic assumption made in the design of this equipment is that the MIS diodes to be measured are almost lossless. In this case it is

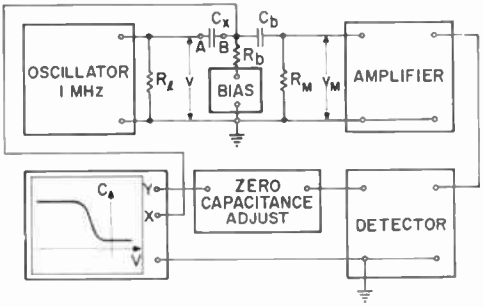

Fig. 3—Simplified schematic of measuring apparatus. $R_I = 50$ ohms, $R_b = 10{,}000$ ohms, and $C_b = 0.01$ μF. All other components are discussed in the text.

sufficient to measure the magnitude of the MIS admittance, and there is no need for a phase-sensitive detector.[8] A schematic of the basic measuring circuit is shown in Figure 3. If a constant a-c voltage is applied across the MIS diode, then the current is essentially determined by the reactance of the diode, and the voltage across the measuring resistor R_M (which must be small with respect to the diode reactance) can be used as a measure of the capacitance. Specifically, if the conditions

$$R_M \ll \frac{1}{\omega C_x} \ll R_b \tag{2}$$

[7] A. G. Revesz and K. H. Zaininger, "The Influence of Oxidation Rate and Heat Treatment on the Si Surface Potential in the Si-SiO, System," *Trans. IEEE Electron Devices*, Vol. ED-13, p. 246, Feb. 1966.

[8] M. Zerbst and H. E. Longo, "Kapazitive Untersuchungen an Halbeiter-Insulator-Grenzflächen," *Zeit, Angew. Physik*, Vol. 19, p. 85, April 1965.

and

$$C_b \gg C_x \tag{3}$$

are satisfied, the magnitude of the a-c voltage appearing across R_M is

$$|v_M| = |v|\,\omega R_M C_x. \tag{4}$$

Here, C_x is the equivalent parallel capacitance of the MIS diode, C_b is a blocking capacitor, and ω is the frequency of operation. $|v|$ is the magnitude of the a-c signal from the oscillator, which is adjusted so that the signal across C_x is never larger than 20 mV. If the condition

$$\frac{1}{\omega C_x} \gg 50 \text{ ohms} \tag{5}$$

is satisfied, then $|v|$ is essentially constant and $|v_M|$ is proportional to C_x, i.e., $|v_M|$ can be used as a measure of the MIS capacitance.

A sawtooth voltage is applied to the MIS capacitor through a parallel branch which is a-c shorted by the series combination of C_b and R_M, to provide a smoothly varying bias. A 1 MHz oscillator is used as the signal source. If v_M is displayed as a function of the applied bias, then the envelope of the resulting curve is the C-V characteristic. However, because of the condition in Equation (2), the magnitude of v_M is about 0.2 mV, necessitating amplification. The amplifier indicated in Figure 3 has a gain of about 100 db. The amplified signal is then detected and the d-c voltage, which is proportional to capacitance, can be exhibited as a function of the applied bias on either an X-Y recorder or an X-Y oscilloscope, depending on the rate of change of bias.

As can be seen from Figure 3, the experimental arrangement allows a so-called three-terminal capacitance measurement, thus excluding all stray capacitances that may exist to other parts of the structure. MIS capacitors are, however, not ideal, lossless devices, and thus there is a differential conductance associated with them.[1-4] Since the measurement method employed here is not phase sensitive, this conductance will introduce an error in the measured capacitance. Actually, what is measured is the absolute value of the MIS admittance, given by

$$|Y| = \sqrt{G^2 + (\omega C)^2}, \tag{6}$$

where G and C are the equivalent parallel MIS conductance and

capacitance, respectively. If it is assumed that this admittance is solely due to an effective capacitance, C', which can be expressed as

$$C' = C + \Delta C. \tag{7}$$

where ΔC is the error, then the percent error in the MIS capacitance is

$$\text{Percent Error} = 100\,\frac{\Delta C}{C} = 100\left(\sqrt{\frac{1}{Q^2} - 1} - 1\right) \tag{8}$$

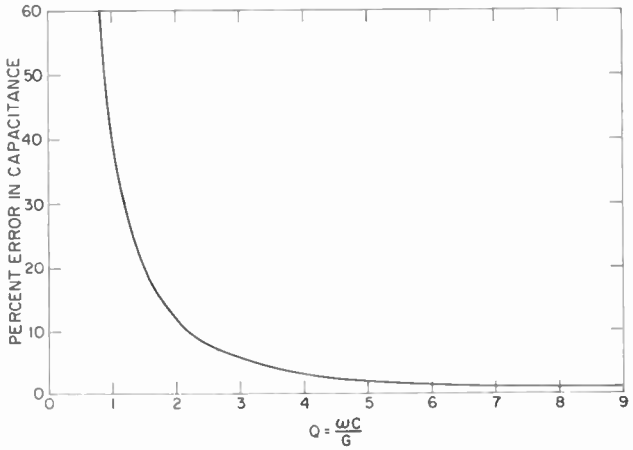

Fig. 4—Percent error in the measured capacitance due to presence of losses associated with the MIS capacitor, as a function of Q.

where $Q = \omega C/G$. From Figure 4, where this error is shown as a function of Q, it can be seen that the error in capacitance can be kept below 5% if the Q is somewhat better than 3. This is possible in many MIS structures produced with present-day technology, and the excellent agreement with bridge measurement is shown in Figure 5. Of course, if considerable series resistance is present, as, for example, in the case of semi-transparent gates in photoresponse measurements or with nonohmic back contacts or when G is large because the insulating film is leaky or broken down, the error becomes excessive.

Circuits

Measuring Circuit

The actual measuring circuit is shown in Figures 3 and 6. Calibration is achieved by a precision (10 pF) capacitor that can be con-

nected across the measurement terminals by means of switch S-1 (see Figure 6a). Another switch (S-2) allows the capacitor under test to be short-circuited so that it is not stored or heated under charged conditions. The measuring resistor, R_M, is 1500 ohms shunted by the very low (about 3-ohm) input impedance of a common-base transistor amplifier, which is the first stage of amplification. Thus, the actual measuring resistor is about 3 ohms, easily satisfying the condition in Equation (2).

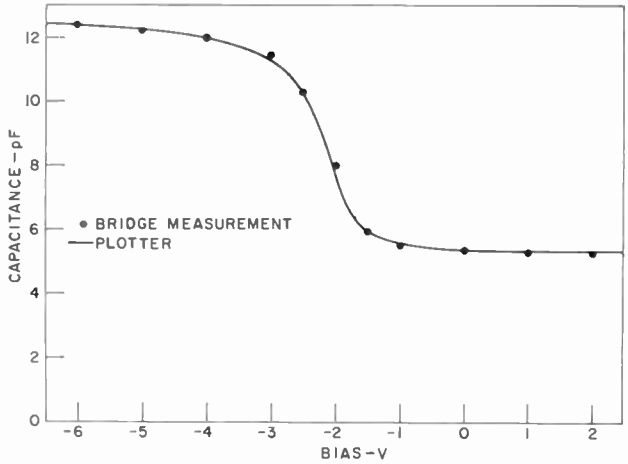

Fig. 5—MIS capacitance versus bias as obtained by measurement with the plotter and with a Boonton Electronics 75A Capacitance bridge.

The Bias Circuit

The bias for the capacitor is supplied from the horizontal output of the oscilloscope in series with a variable-voltage source. A linear voltage–time sweep with adjustable upper and lower limits is therefore obtained. The lower limit is set by blocking the scope output (switch S-4). The upper limit is then set by varying the magnitude of the scope sweep by means of a potentiometer.

The arrangement shown gives a maximum bias range of about 90 volts within the range of —90.0 to +90.0 volts.

Amplifier Circuit

The amplifier circuit consists of four stages. The first stage, a common-base configuration, serves as combination of measuring resistor and amplifier. The second stage is the tuned amplifier shown in Figure 6a. The third stage is an oscilloscope (the same as that used for the

sawtooth voltage) and associated plug-in unit (a type L in our case). The signal from the tuned amplifier is fed into the plug-in unit, and the amplified signal is taken out at the "VERT.SIG.OUT" and connected to the fourth stage of amplification, the emitter follower, shown in Figure 6b. This last stage serves as a driver for the detector, thus avoiding any loading of the previous stages.

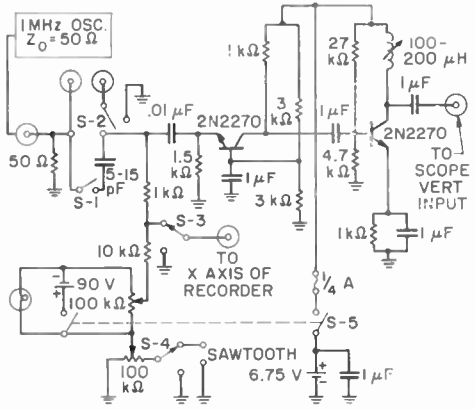

(a)

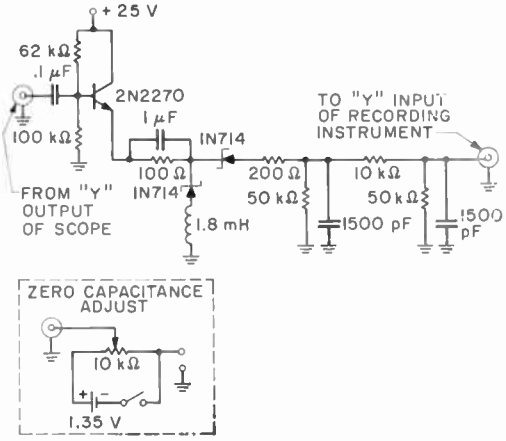

(b)

Fig. 6—Detailed schematic of measuring apparatus. (a) Measuring circuit with bias supply and first two stages of amplification. S-1 to S-4 are push-button switches, S-5 is the on-off switch. Push S-1 to calibrate, S-2 to temporarily ground gate, S-3 to check X-axis zero, and S-4 to measure the lower bias limit. (b) Last stage of amplification, detector, and zero-capacitance adjust circuit.

Detector

Since the ratio of minimum to maximum capacitance becomes quite small for MIS capacitors made from high-resistivity semiconductors and having a thin insulator film, the percent modulation of the signal can become quite high. For this reason, the special detector shown in Figure 6b was built in which the voltage drop across the rectifying diode is so small that it does not introduce any distortion. This is achieved by two low-capacitance Zener diodes, matched to within 1%, one of which is used to bias the detector diode to the verge of breakdown.

Zero-Capacitance Adjust Circuit

It is desirable to cancel out the masking effects of stray capacitances, including that of the sample holder. This could be done by means of an inductor across the test terminals that resonates with the undesired capacitance. Since at the output of the detector the effect of the stray capacitance is to introduce a d-c voltage, it is much simpler to inject a d-c voltage that exactly cancels that due to the undesired capacitance. This can be achieved with the circuit shown in the insert in Figure 6b. The advantage of this arrangement is that under a variety of different test conditions the zero capacitance can be easily, rapidly, and accurately adjusted.

Display

Any recorder with a high input impedance can be utilized in this application. For fast bias-sweep rates an X-Y oscilloscope can be used for displaying the C-V curves, and permanent copies can be obtained by means of a camera. For slower sweep speeds an X-Y recorder can be used that furnishes a copy immediately. The X channel is essentially used as a voltmeter. The variable d-c gain of the Y channel is used to calibrate the apparatus so that actual or normalized capacitance is read directly.

Sensitivity and Accuracy

The range of this apparatus is determined by the setting of the gain in both the oscilloscope amplifier and the recording instrument. It can be adjusted from about 500 pF/inch to 0.1 pF/inch. Care must be taken that the oscilloscope amplifier is not overloaded. This is achieved by making sure that in the accumulation regime, when the insulator capacitance is measured, the oscilloscope trace is not outside the graduated area.

The limit in sensitivity is determined by the quality of the detector, and is typically 0.1 pF/inch. The accuracy is limited by the stability of the oscillator and amplifiers, by the linearity of the amplifiers, by the distortion introduced by the detector, and by the calibrating capacitor. Typically, an accuracy of 2% is possible, as can be seen from Figure 7.

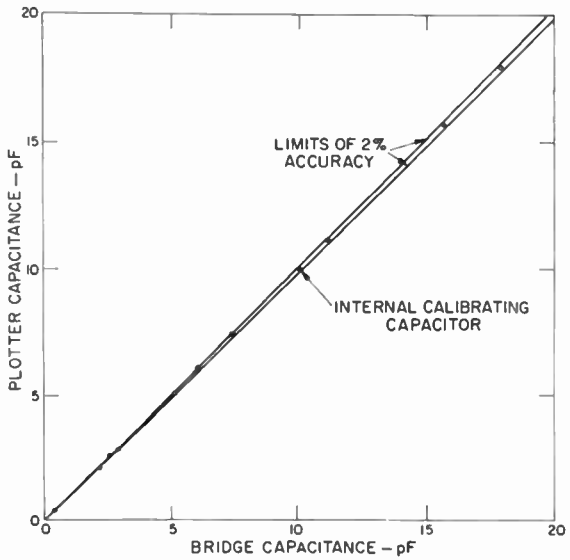

Fig. 7—Plot of capacitance as measured by the plotter versus that obtained, for the same device, by bridge measurements, to demonstrate the obtainable accuracy.

Device Mounting

In addition to the conventional way of connecting samples directly to the measurement circuit, there are several kinds of other sample holders that make this equipment more versatile and useful.

Wafer Holder

For a large number of applications it is desirable to measure MIS capacitors immediately after their fabrication in the unbroken semiconductor wafer at room temperature and in air. For this purpose a special sample holder, shown schematically in Figure 8, is employed. Connection to the ohmic contact on the back of the wafer is made by simple contact to the gold-plated supporting brass plate. A micromanipulator with a tungsten wire is used to make contact to the gates. This arrangement makes possible the rapid measurement of a whole array of MIS capacitors in the original wafer.

Modes of Operation

The apparatus described in the previous sections is quite versatile and may be used in several ways. Two more common modes of operation are continuous sweep and single sweep.

Continuous-Sweep Operation

In this mode the oscilloscope is set for continuous sweep. The sweep speed, and thereby change of bias, can be varied from 2 min/bias-sweep to 10 msec/bias-sweep. For rates of change faster than about 2 sec/bias-sweep, an oscilloscope must be used as display instrument.

Single-Sweep Operation

With the use of the Tektronix 545 oscilloscope, operation in a single-sweep mode is possible by properly adjusting the triggering level. In this mode the bias on the capacitor stays at the level set by the lower bias limit. Upon pushing the "Main Sweep Reset" button, bias will sweep through the predetermined range and then stay again at the lower bias limit. Triggering of the sweep can also be accomplished by means of an external triggering signal and the same range of sweep speeds is available.

Conclusions

MIS capacitors, because of the simplicity of their construction and the sensitivity of their *C-V* characteristics to physical properties, can advantageously be used as a test vehicle for the study of the influence of process parameters on properties of insulating films on semiconducting substrates and metal–insulator–semiconductor interfaces. The experimental arrangement described above allows the automatic and rapid measurement of the MIS capacitance versus bias characteristics at 1 MHz over a wide range of biases and sweep speeds and under a variety of experimental conditions. It is assembled from essentially standard laboratory equipment, provides a graphical output, and makes possible the rapid study of problems in MIS physics that otherwise would have, at best, been extremely cumbersome and time-consuming.

Acknowledgments

The author should like to thank A. K. Rapp, who designed the detector, and D. C. Mackwell for valuable assistance in the design and construction of this equipment.

APPENDIX A—DETERMINATION OF IMPURITY CONCENTRATION FROM MIS CAPACITANCE MEASUREMENTS

The high-frequency MIS capacitance versus bias characteristics represent a convenient tool for determining the impurity concentration

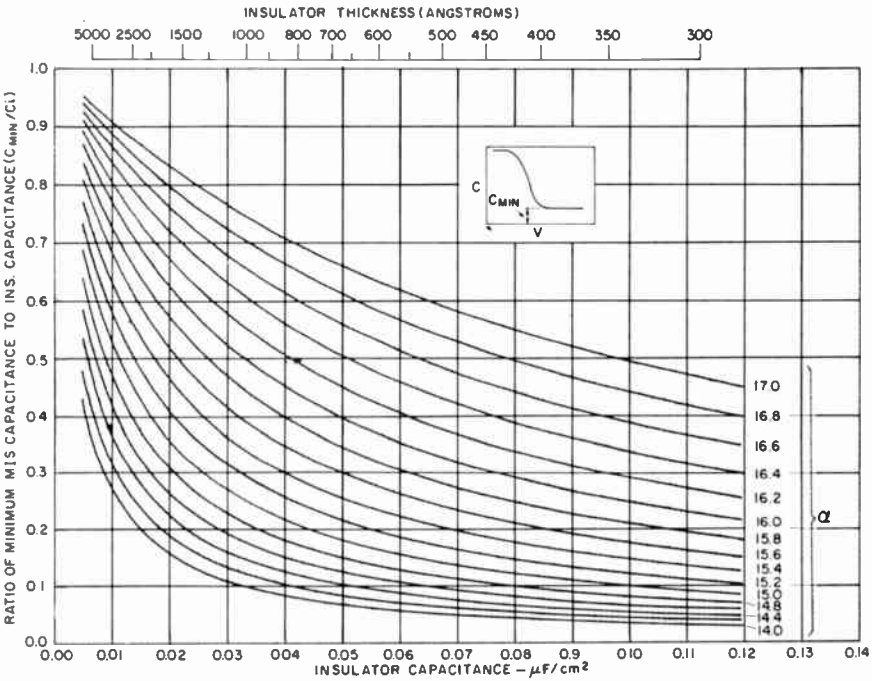

Fig. 10(a)—Dependence of normalized MIS capacitance at room temperature on the insulator capacitance per unit area with $\alpha = \log_{10} N$ as parameter. For the case of SiO_2 films ($\epsilon = 3.82$), the second abscissa with oxide thickness can be used. These curves are applicable when minority carriers follow both a-c and d-c signals (curve 1 in Figure 1).

in the semiconductor surface space-charge region.[9, 10] The conductivity type of this layer can be found from the shape of the *C-V* curve.[11] The value of the minimum capacitance is used to obtain the doping concentration because the minimum normalized MIS capacitance, C_{nmin}, is a function of both the insulator capacitance per unit area and the

---

[9] K. H. Zaininger, Ph.D. Thesis, Princeton University, 1964.

[10] B. E. Deal, A. S. Grove, E. H. Snow, and C. T. Sah, "Observation of Impurity Redistribution During Thermal Oxidation of Silicon Using the MOS Structure," *Jour. Electrochem. Soc.*, Vol. 112, p. 308, March 1965.

[11] F. P. Heiman, K. H. Zaininger, and G. Warfield, "Determination of Conductivity Type from MOS-Capacitance Measurements," *Proc. IEEE*, Vol. 52, p. 863, July 1964.

impurity concentration. Since the doping and insulator capacitance enter the expression for the MIS capacitance in completely different ways, it is not possible to give an exact analytical expression for the minimum MIS capacitance as a function of doping and insulator capacitance. However, it is possible to give C_{nmin} as a function of

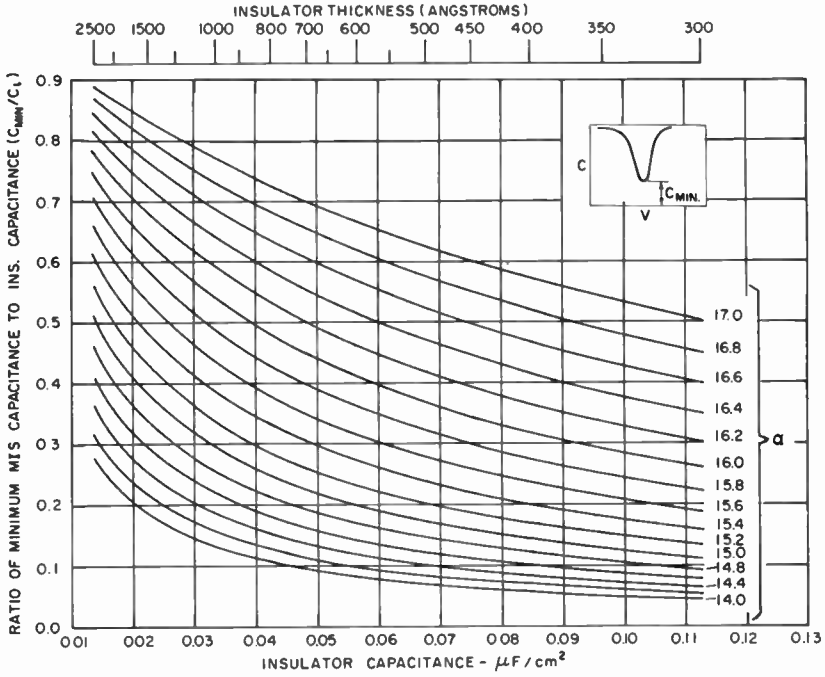

Fig. 10(b)—Same as Figure 10(a), except that the curves are applicable when minority carriers follow bias but not a-c signal (curve 3 of Figure 1).

insulator capacitance (and/or insulator thickness) with impurity concentration as a parameter. This dependence has been calculated by means of a digital computer for two different situations. For the case where minority carriers follow both a-c and d-c signals, Figure 10a is applicable, and for the case where minority carriers follow d-c but not a-c signals, Figure 10b applies. The resistivity of the material can then be obtained by use of the data represented in Figure 11.

Appendix B—Determination of Effective Density of Surface States

The effective density of surface states is determined by a com-

parison of actual and ideal *C-V* curves. FORTRAN programs have been developed to perform these otherwise laborious time-consuming calculations. The proper doping density required for calculation of the ideal curve can be determined from the ratio of minimum to maximum capacitance. This is especially important because of impurity

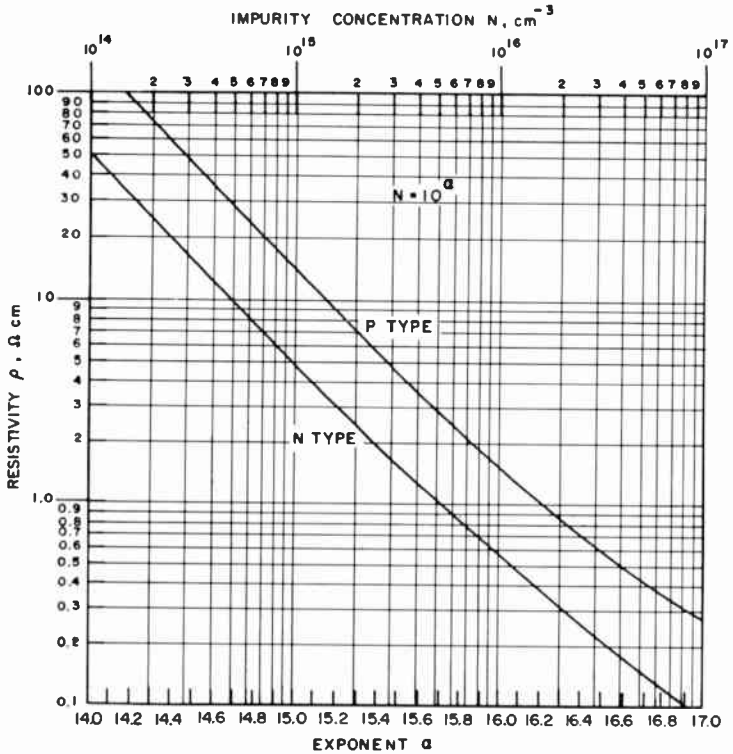

Fig. 11—Dependence of resistivity on the impurity concentration $N = 10^a$ for both n- and p-type silicon at room temperature.

redistribution in semiconductors during thermal oxidation. The insulator thickness is then determined by ellipsometry[12] (or other means) or, if the gate area is known, insulator capacitance per unit area is measured. This information together with the desired number of points of the experimentally determined *C-V* curve are fed into the computer; the computer then calculates the density of surface

[12] K. H. Zaininger and A. G. Revesz, "Ellipsometry—A Valuable Tool in Surface Research," *RCA Review*, Vol. 25, p. 85, March 1964.

states as a function of surface potential (or energy above the valence band).*

Appendix C—MIS Flat-Band Capacitance

In many cases, a general characterization of the system is desired, rather than a description of the dependence of surface states on surface potential. The density of surface states at zero surface potential,

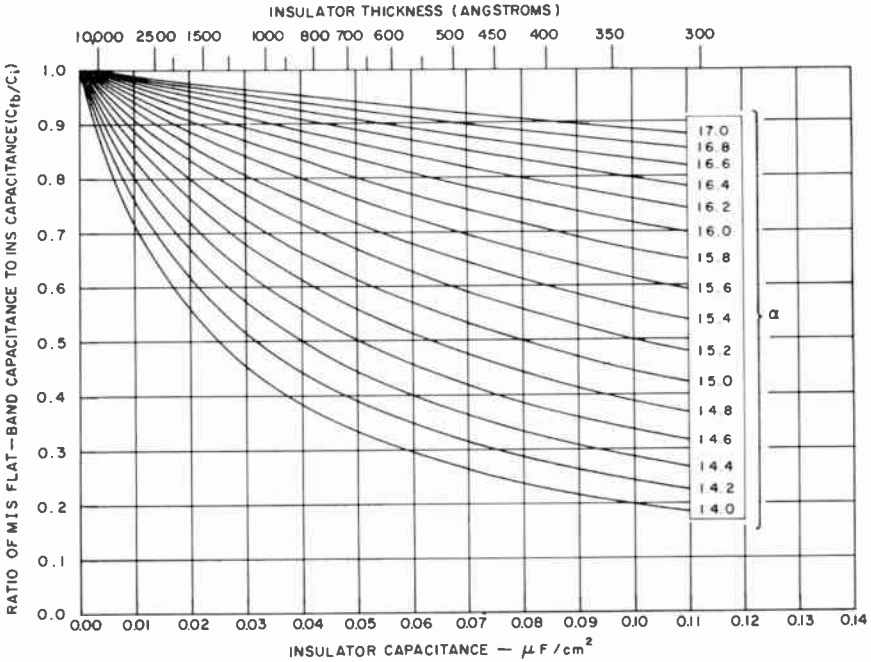

Fig. 12—Dependence of normalized MIS flat-band capacitance at room temperature on the insulator capacitance per unit area with $\alpha = \log_{10} N$ as parameter. For the case of SiO_2 films ($\epsilon = 3.82$) the second abscissa with oxide thickness can be used.

i.e., at the flat-band condition, is a parameter that is representative of the state of the insulator–semiconductor interface and can be used as a quality factor.

The normalized MIS flat-band capacitance, C_{nfb}, can easily be calculated from the space-charge flat-band capacitance, which is given by[6]

* Programs for both n- and p-type substrates are available on request from the author.

$$C_{\text{sefb}} = \frac{1}{\sqrt{2}}\left(\frac{\epsilon_s}{\lambda}\right) = \left(\frac{\epsilon_s e N}{kT/e}\right)^{1/2} \tag{9}$$

and C_i;

$$C_{\text{nfb}} = \frac{1}{1 + C_i/C_{\text{sefb}}} = \frac{1}{1 + C_i\left(\dfrac{kT/e}{\epsilon_s e N}\right)^{1/2}}$$

Here k is Boltzmann's constant, T is temperature, e the magnitude of the electronic charge, ϵ_s the semiconductor dielectric constant and $N = 10^{\alpha}$ is the impurity concentration. The flat-band capacitance versus C_i, with exponent of doping density, α, as parameter, is shown in Figure 12.

VIDICON PERFORMANCE IN EXTREME THERMAL ENVIRONMENTS*

By

R. E. Johnson

RCA Electronic Components and Devices
Lancaster, Pa.

Summary—A number of vidicons representative of the average commercial types were operated in a thermal chamber at practical extremes of temperature, and the resulting changes in performance characteristics were recorded. Signal output levels have been found to limit the useful operating range to approximately 100°C when other parameters are held constant. Absolute values of high and low temperature will vary with the "normal" temperature operating conditions selected. When target voltage and illumination are adjusted to compensate for changes in basic material characteristics, the useful operating range can be extended to as much as 200°C. Resolution and gamma were not affected by temperature to the extent that they would materially alter vidicon performance in the practical sense. However, lag was found to improve substantially at high temperatures and become progressively worse as the temperature goes down.

Introduction

THE use of vidicon camera tubes in space missions and in a variety of military systems has generated a high degree of interest in their performance over extreme temperature ranges. Users are normally concerned with vidicon operation at temperatures between −100°C and 100°C, and with pure survival (nonoperational, but with no permanent damage to the tube) over temperature ranges of −160°C to 125°C. Previous tests demonstrated that conventional vidicons have a very good chance of survival without permanent damage as the temperature is varied between −175°C and 100°C. This paper describes an investigation of changes in performance characteristics that occur over this temperature range.

The photoconductor used in vidicon camera tubes is basically a semiconducting material having a resistance that changes substantially with exposure to light. When a given voltage is applied across this very thin target layer, the current flow in discrete areas exposed to light builds up a charge pattern on the target that is retained for a finite length of time. The removal of this charge pattern by electron-beam scanning generates a video signal that can be used in a variety of applications.

The target material used in most conventional vidicons possesses

physical characteristics that provide optimum performance at temperatures somewhat above ordinary ambients (i.e., 25 to 35°C). At high temperatures, the resistance of the photolayer decreases and increasingly higher darker currents are produced for a given applied potential. Although the signal current also increases, the dark current increases at a significantly higher rate, and a practical operational limit is eventually reached. At low temperatures, there is a corresponding decrease in both dark current and signal current. However, the rate of decrease of the signal current is less than that of the dark current. Consequently, performance levels tend to be maintained longer as temperature decreases. In fact, operation at moderately low temperatures may be beneficial in some respects because of the reduction or elimination of the many harmful side effects that accrue from high-dark-current operation (e.g., bad shading characteristics that tend to develop with high dark currents).

Test Procedure

Performance data over a wide temperature range were measured on a developmental electrostatic-focus vidicon designed for military use. Test data was obtained for the following conditions as the temperature was varied.

1) The tube was adjusted for nearly optimum operating conditions at a recommended operating temperature (approximately 30°C), and operating-performance changes were measured. The limits of practical usefulness of the tube as a video-signal generating device without additional adjustment were also determined.

2) Constant illumination levels were maintained, but the target voltage was continuously adjusted to maintain constant dark current; performance changes and practical limits on temperature that determine the usefulness of the device were again measured.

3) All operating parameters were kept constant, and the illumination-level changes required to maintain constant signal-current levels were measured, together with practical limits to this adjustment.

4) A constant level of signal current was maintained to avoid incidental effects of noise and other detrimental effects, and resolution or picture-sharpness characteristics of the vidicon were determined.

5) A constant signal output was maintained by adjustment of the illumination level, and the effect of temperature changes on lag characteristics was measured. (The evaluation must be made in this manner, because light level, signal current, target voltage, and dark current have a measurable effect on the absolute value of residual signal,

or lag, even when the temperature of the photoconductor remains constant.)

6) Changes in the gamma characteristic of the vidicon were measured.

It is important to note that all data presented were recorded on a single tube. While it is reasonable to assume that this particular tube had "typical" characteristics and was representative of the average product, the inevitable variations from tube to tube must not be overlooked. The information presented here is intended to serve only as a guide; it should not be regarded as giving absolute performance limitations.

Unattended Operation Over Extreme Temperature Ranges

When the vidicon was adjusted for optimum operation (i.e., best over-all picture at some operating temperature), the major parameter that changed directly with temperature was the dark current. Changes in dark current may be accompanied by secondary changes in other parameters, or may induce changes in other parameters. At any rate, it is usually advisable, if not actually necessary, to adjust other parameters so as to control dark current and thus maintain a relatively constant level of performance in terms of other operating characteristics (such as signal, signal uniformity, lag, and resolution).

The first test in extreme thermal environments, however, was designed to determine how vidicon characteristics would change if virtually no adjustments were made on any of the operating controls. The tube was set up in a specially constructed camera head operated from a TK15 camera unit (all tests were made at conventional television scan rates). The photoconductor was flooded with uniform incandescent light to produce normally recommended signal-current levels for a particular dark current at near room temperature. A strip of opaque black tape was placed on the test source to provide a black reference for peak-to-peak signal measurement. The target voltage was adjusted to obtain the desired dark current. All other operating voltages and the light intensity were maintained constant as the thermal environment changed from approximately —70°C to 100°C. Temperature of the vidicon was determined by means of a thermocouple junction attached to the faceplate area of the tube. For all measurements, the environmental chamber temperature was maintained at a given setting or test point until the vidicon characteristics stabilized completely. This condition was attained by continuous monitoring of vidicon parameters with meters inserted in the television system. Figures 1-5 show the results of this series of tests.

Figure 1 shows that the dark current is an exponential function of temperature. It is also higher for higher target voltages (i.e., for higher reference-temperature dark currents). If a dark-current level of 0.2 microampere is established as the maximum limit for useful operation,* the curves show that this limit is reached at 40° to 45°C for a target voltage of 40 volts, at 55° to 60°C for 30 volts, and at approximately 70°C for 20 volts.

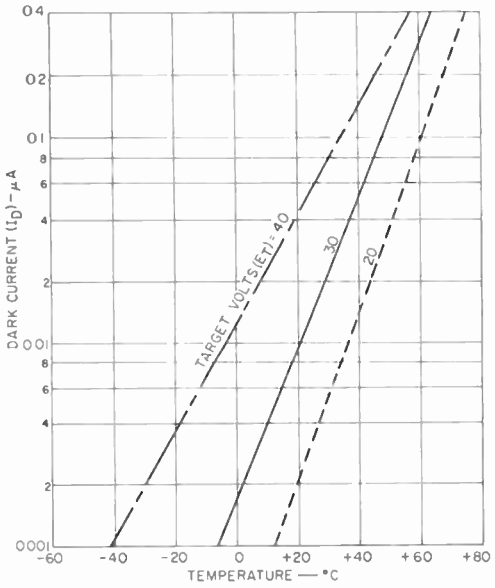

Fig. 1—Variation of vidicon dark current with temperature for three values of fixed target voltage.

The first conclusion, then, is that lower target voltages permit significantly higher-temperature operation before dark current becomes prohibitive. In addition, when an appropriate target voltage is used, operation at temperatures as high as 75° to 100°C is feasible, provided other characteristics are not more seriously affected.

In normal circumstances, the signal-current level I_s imposes a primary limitation only at very low temperatures. Figure 1 shows that the dark current decreases to near zero at low temperatures

* In many applications, a dark current of 0.1 microampere has been found to be the limit for acceptable system performance. If a lower dark current limit is adopted, the useful operational range of temperature must be modified accordingly.

within the normal range of exploration. Although a number of factors affecting camera-tube operation may make this low dark-current level a basically desirable characteristic, the signal level also decreases and a point is reached at which the vidicon is no longer useful. If this limiting signal level is arbitrarily set at 0.01 microampere (with negligible dark current some very useful pictures may be generated with this magnitude of signal), the curves of Figure 2 show that the tube is useful to —30°C with 20 volts on the target, to —50°C with

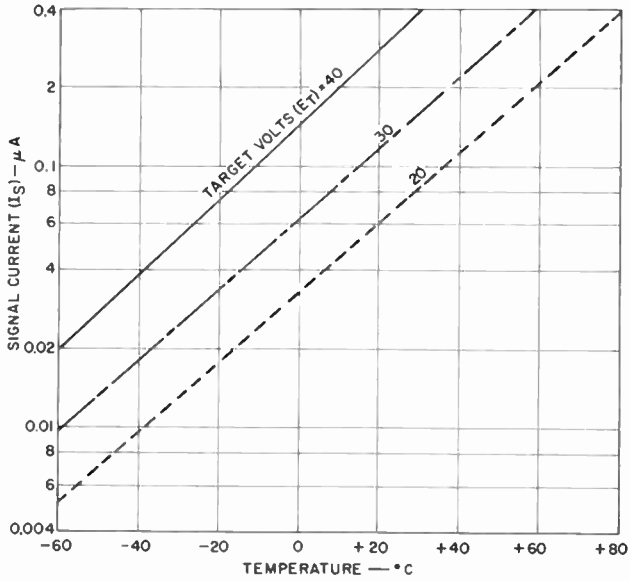

Fig. 2—Variation of vidicon signal current with temperature for three values of fixed target voltage.

30 volts on the target, and to temperatures below —60°C with 40 volts on the target.

Figures 3, 4, and 5 show the practical operating range for typical vidicons for target voltages of 20, 30, and 40 volts, respectively. At 20 volts (Figure 3), the vidicon operates satisfactorily without adjustment (with the possible exception of beam current) over a temperature range —30° to 70°C. Performance is typically limited by low signal (0.01-microampere point) at —30°C, and by high dark current (0.2-microampere point in Figure 1) at 70°C. The total current of 0.4 microampere encountered in the 70°C region should be handled successfully by conventional vidicon designs. It is interesting to note that signal current is approximately equal to dark current at 20 volts

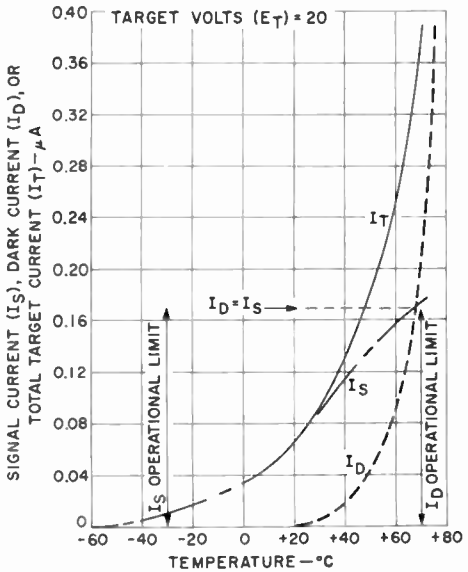

Fig. 3—Variation of vidicon currents with temperature at a target voltage of 20 volts.

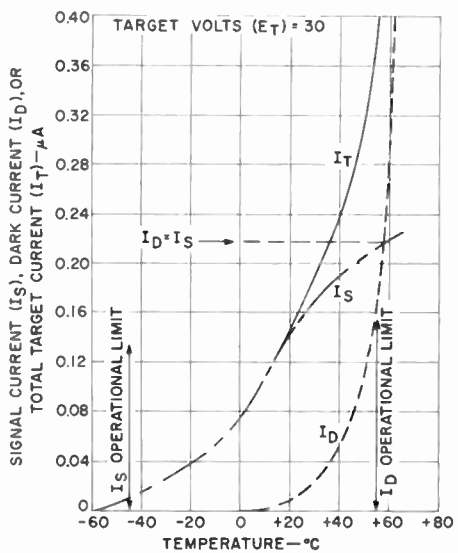

Fig. 4—Variation of vidicon currents with temperature at a target voltage of 30 volts.

at this temperature. In most applications, this ratio would be regarded as acceptable at the extreme environmental operating point.

At a target voltage of 30 volts (Figure 4), a typical vidicon will operate over the range —45° to 55°C without adjustment (it is again assumed that the tube was set up for optimum performance in the temperature range of 25°C to 30°C). At the lower limit of —45°C, signal level is still the limiting parameter. At temperatures of 50° to 60°C, however, performance is limited by a combination of high dark

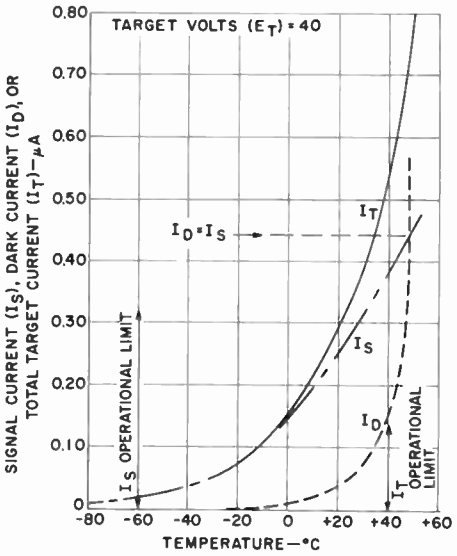

Fig. 5—Variation of vidicon currents with temperature at a target voltage of 40 volts.

current I_D, and high total target current I_T (discharge limitations). At this target voltage, the dark current equals the signal current at a temperature of approximately 60°C.

At a target voltage of 40 volts, signal output limits useful operation at approximately —60°C. At the high-temperature extreme, dark current combines with total target current to limit normal operation at approximately 40°C. Although a typical 100°C useful operating range without vidicon adjustment appears feasible, the practical signal-current-to-dark-current ratio is far above the 1:1 ratio at the maximum temperatures achieved in the other two modes. Under these conditions, total target current is more apt to limit practical operation than dark current alone.

Figures 3, 4, and 5 show that dark current becomes virtually zero

at 20°C at 20 volts, at 0°C at 30 volts, and at approximately —20°C at 40 volts. Zero or negligible dark current is, generally speaking, a most desirable operating mode, other things being equal. Subsequent thermal tests (described later) were made to determine what illumination and/or target-voltage compensations would be required to achieve optimum performance over a similar range of temperatures.

Performance over Extreme Temperature Ranges with Constant Dark Current

In the next series of tests, the vidicon was set up as in the previous tests, except that the absolute value of dark current was maintained

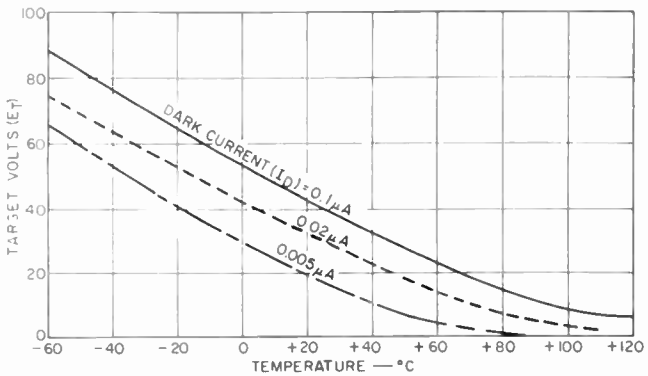

Fig. 6—Variation of vidicon target voltage required to maintain dark current constant at three levels as a function of temperature.

constant by adjusting the target voltage. Figure 6 shows the target-voltage compensation necessary to maintain certain fixed values of dark current over the temperature range considered. Figure 7 shows the change in signal current that results when dark current is maintained constant and illumination levels are unchanged from the optimum set-up condition in the reference operating range of 25° to 30°C.

The established fact that vidicons can be operated quite satisfactorily in the target range of 10 to 100 volts, other conditions being adaptable, provides an objective point of reference to establish operational boundary limits. As pointed out previously, however, variations in the dark-current/target-voltage characteristic of individual tubes may alter the useful range in practice. In this context, Figure 6 shows that, with suitable target-voltage adjustment, a dark current of 0.005 microampere can be maintained from —100° to 50°C, of 0.02 microampere from —80° to 70°C, and of 0.1 microampere from —60° to 90°C.

These values represent an absolute range of at least 150°C for constant-dark-current operation in each instance, with the specific range variable for the particular dark current selected. It is apparent that, in practice, moderately high dark currents provide a greater range because the lower target-voltage limit of 10 volts is reached earlier in the case of low-dark-current operation.

Even though constant dark current is maintained without change over extreme ranges of temperature by proper target-voltage compensation, vidicon signal currents decrease substantially, particularly at high temperatures, as shown in Figure 7. Standard test procedure

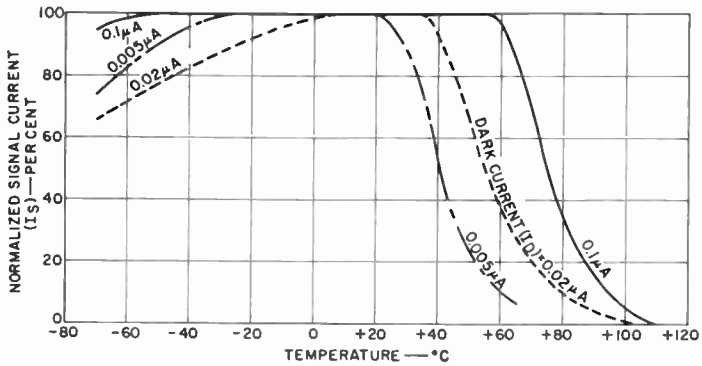

Fig. 7—Variation in normalized vidicon signal current as a function of temperature for three values of constant dark current.

provided for a normalized 100% signal output (usually 0.2 microampere) at normal ambient temperature (about 20°C). This output was obtained by adjustment of illumination levels to match a specific dark-current value achieved with target-voltage setting. Figure 7 shows that for all dark-current levels, the signal current decreases rapidly as the target temperature increases. However, for the lower-dark-current mode, the decrease begins at substantially lower temperatures and, correspondingly, practical vidicon operation is limited to a much lower temperature because of low signal output.

For a constant dark current of 0.005 microampere, the signal current starts to decrease as soon as the temperature is raised above the normal ambient room temperature of 20°C and continues to deteriorate as the temperature increases, until it reaches the 10% point at 60°C. For an intermediate dark current of 0.02 microampere, the signal is constant up to 35°C and then deteriorates progressively until the 10% signal level is reached at a high temperature extreme of 80°C.

For the highest dark current shown in Figure 7, 0.1 microampere, the signal does not begin to deteriorate appreciably until 55°C, and the 10% signal level is reached at 95°C.

At temperatures below 20°C (and, in fact, at extremely low temperatures), the signal holds up remarkably well for all dark-current operating modes. Although very high dark currents (high target voltages) may provide improved operation, the difference is not as clear cut and sharp at low temperatures as at high temperatures. In general, at the minimum chamber temperature of —70°C, signal levels for all three values of dark current decreased less than 30% from their normalized 100% room-temperature levels. At the very highest dark current (0.1 microampere), the measured decrease was only about 5% of normal signal at the minimum temperature point. At low temperatures, however, the lag characteristic (described later) may be a factor in determining the minimum useful value of target temperature.

Performance Over Extended Temperature Ranges With Variable Illumination

Figure 8 shows the performance obtained when the target voltage is retained at some constant typical value and the illumination is adjusted to maintain normal signal levels. At an intermediate target-voltage level, 30 volts, a normal optimum signal level of 0.2 microampere can easily be maintained over a temperature range of —40° to 60°C. The illumination level required for this type of operation need not exceed about 4 foot-candles on the faceplate of the vidicon. By varying both the target voltage and the light level, the full-signal performance range can be extended still further. With a target voltage of 40 volts, the vidicon can be expected to operate at temperatures as low as —50°C without loss in signal output. If the target voltage is reduced to 20 volts, full-signal-level performance can be extended to a high temperature of about 80°C.

There are ultimate limits of practical operation apparent at both ends of the temperature range. For a particular target voltage, for example, it is evident that the light level required to maintain the signal level at low temperatures rises at an exponential rate. In practice, therefore, it would not be feasible to maintain the signal output level indefinitely by means of extra illumination. Similarly, at very high temperatures, the dark current rises exponentially with temperature to a point where the vidicon can no longer supply enough beam current for complete neutralization of the charge accumulated

on the target. Although this effect can be compensated by reduction of the target voltage, a minimum target voltage is eventually reached, below which the vidicon cannot function. This effect presents a presumably insurmountable barrier to extreme temperature range for conventional vidicons.

The following conclusions may be drawn from the data shown in Figure 8:

(1) Suitable adjustment of illumination levels permits operation at optimum target voltages over a 100°C range (—40° to 60°C) with no loss in signal amplitude.

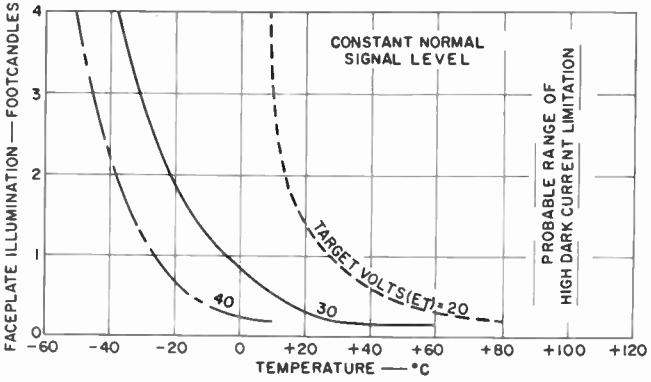

Fig. 8—Variation of vidicon faceplate illumination required for constant normal signal level at three values of constant target voltage as a function of temperature.

(2) Auxiliary adjustment of target voltage to the extent indicated extends this range to 120°C (—50° to 70°C). Full permissible adjustment of target voltage in combination with illumination could conceivably extend the full-signal operating range to 200°C (—100° to 100°C).

(3) Operation beyond these limits (or even up to the maximum limits indicated) will undoubtedly depend on photoconductor characteristics other than signal output. At high temperatures, the limitation might be prohibitive dark currents; at low temperatures, it might be excessive lag or image retention. In both instances, physical factors associated with tube fabrication and assembly may also need to be considered.

Resolution Over Extreme Temperature Range

For tests of vidicon resolution, amplitude response at a given

television line number is used as the criterion.* This method is more objective and more accurate than the technique of limiting resolution in a converging wedge. Standard picture size imaged on the faceplate of the tube is 0.44 by 0.44 inch for the vidicon used.

Resolution was measured at a constant typical signal-current level of approximately 0.1 microampere. Dark current was maintained at a level of approximately 0.02 microampere. These conditions were imposed because the measured resolution and response can be affected significantly by higher or lower signal-current values. In the first case, the beam-spot current density changes and the size increases. At low signal-current levels, on the other hand, amplifier noise characteristics become an appreciable factor in accurate measurement of the true response. Therefore, the signal level was maintained essentially constant to avoid secondary effects and to permit evaluation of the resolution change as a function of temperature only.

Constant signal current (and dark current) was maintained by adjustment of both target voltage and illumination level. Although these parameters individually were expected to have little effect on resolution, they were controlled simultaneously to provide minimum deviation of each from normal levels, as well as adequate compensation for the full range of temperatures to be investigated.

Light level was adjusted by regulation of lamp current. Besides being a convenient and practical arrangement, this adjustment has less effect on resolution than an equivalent lens-iris adjustment. The lens was set at f:5.6 throughout the test.

The results of the resolution test are shown in Table I and in Figure 9. There is some indication that the resolution or response tends to improve as the temperature decreases from the typical value of 30°C, and that it deteriorates to some extent at high temperatures. The tabulated data show that the per cent response decreased by 5 to 10 as the temperature changes from —70° to 85°C for each line number except the last (600 lines), which generally represents limiting detail detectable. It is generally conceded, however, that the amplitude response is a rather critical method for evaluating resolution. Subjectively, there is no extreme change in picture sharpness evident over the full range of target temperatures investigated.

* Amplitude response is the signal amplitude from a given television line number (fine picture detail) expressed as a per cent of the signal amplitude from a very-low-frequency (large-area) picture element. In practice, the large-detail reference is usually 15 television lines with signal amplitude set equal to 100%. The line number is the number of equal-width black and white lines that will fit into the physical height of the image focused on the camera-tube faceplate.

Table I—Relative Response (Resolution) as a Function of Faceplate Temperature

Temperature (°C)	Amplitude Response (Per Cent) For Various Television Line Numbers							
	100	150	200	300	400	500	600	700
−70	60	45	40	25	17	8	2	0
−60	60	48	40	28	17	8	2	0
−50	60	48	40	28	18	9	3	0
−40	60	48	40	27	17	9	3	0
−30	60	48	40	27	17	8	3	0
−15	60	45	40	27	17	9	4	0
− 5	60	45	40	25	15	8	3	0
+12	60	45	40	25	10	6	1–2	0
+25	60	45	40	24	16	7	1–2	0
+34	60	45	40	25	16	8	2	0
+43	60	45	40	20	15	7	1	0
+53	57	42	39	20	11	7	2	0
+62	55	42	40	20	12	6	2	0
+70	52	40	35	18	10	5	2	0
+85	50	40	35	18	10	4	1	0

Lag Characteristics over Extreme Temperature Range

The lag, or residual-signal characteristic, of vidicons is more critically dependent on signal levels (light) and dark-current values (target voltages) than is the resolution. Consequently, it is important to maintain other conditions constant, as far as practical, to isolate the thermal effect on lag.

For these tests, the signal current and dark current were maintained essentially constant at 0.2 and 0.02 microampere, respectively.

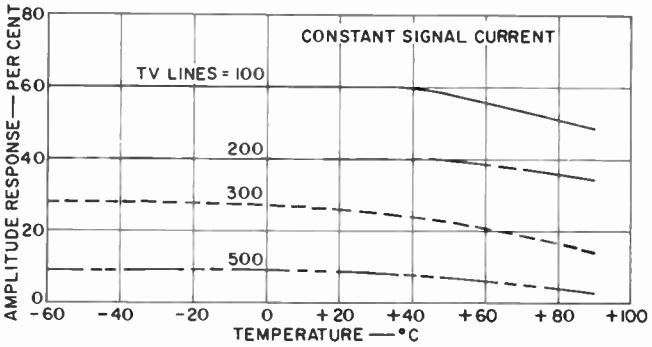

Fig. 9—Amplitude response as a function of temperature for four television line numbers.

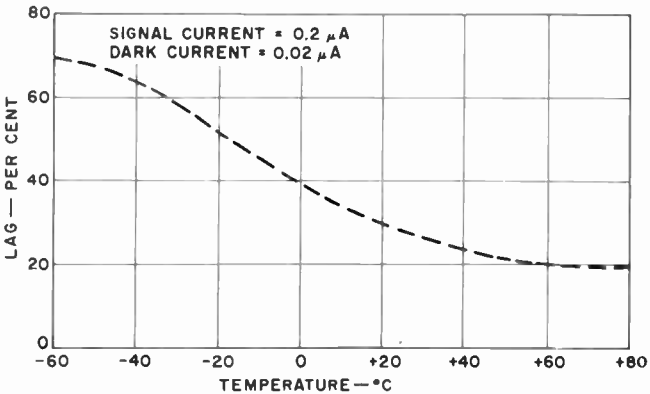

Fig. 10—Fourth-field residual signal (lag) as a function of temperature with constant signal current and dark current.

Secondary parameters such as illumination and target voltage were adjusted at each temperature value to achieve this condition. Experience with this type of photoconductor has shown that signal and/or dark current have a major effect on lag. The change in lag that occurs when signal, dark current, and resolution are maintained at a useful or optimum level over the full temperature range is of considerable interest.

Figure 10 shows how the lag at the normal fourth-field reference point changes over the full range of practical operating temperature under the established conditions. At approximately 25°C, the lag of the vidicon tested was 25%. As temperature decreased, the lag increased at a uniform rate until it reached a maximum fourth-field value of 65%. As the temperature was increased, lag improved to 18% at 60°C. Figure 11 shows lag characteristic over many fields at

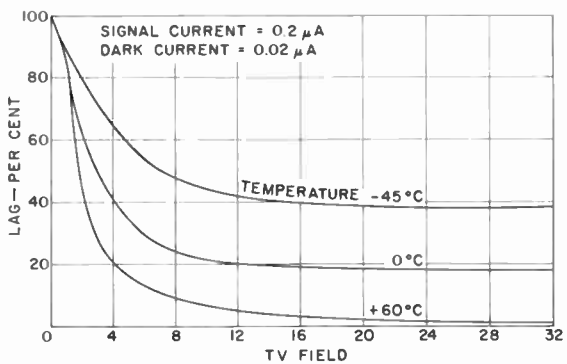

Fig. 11—Residual signal (lag) as a function of television field with constant signal current and dark current at three temperature levels.

a few selected temperature values representing the normal range investigated. The curves in both Figures 10 and 11 indicate that the lag characteristic is very dependent on temperature, especially at operating temperatures below normal ambients.

Gamma Characteristics and Temperature

Figure 12 shows light-transfer curves recorded for a typical vidicon at three temperature points (—60°, 20°, and 65°C). At the high tem-

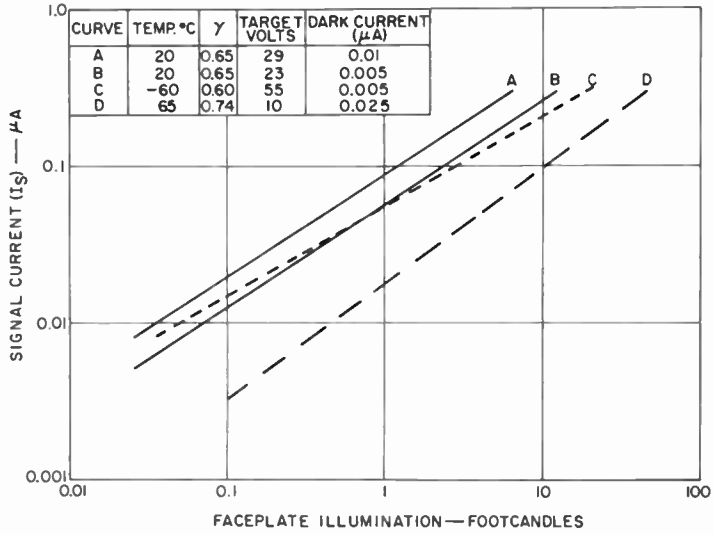

Fig. 12—Light-transfer characteristics at different temperatures and dark-current levels.

perature, the minimum practical dark current is of the order of 0.02 microampere. At the low temperature, dark current is very low. Therefore, the test at the reference temperature was made at two dark-current levels to facilitate comparison of gamma change with temperature.

At 20°C, gamma is exactly 0.65, and is not noticeably affected by dark-current level over a range of signal currents from 0.02 to 0.2 microampere. For comparison of performance at extreme temperatures, transfer curves were recorded for dark currents of 0.005 microampere at —60°C and 0.02 microampere at 65°C. The gamma decreases to 0.60 at —60°C, but increases to 0.74 at 65°C. These results indicate a direct relationship between gamma and faceplate temperature. As the temperature varies, the gamma of the transfer charac-

teristic may be expected to change directly with temperature, as shown in Figure 13.

Although the gamma changes caused by temperature variations appear large, they are actually moderate in relation to gamma variations among individual tubes often encountered at normal temperatures. The gamma for a given tube type normally varies between 0.63 and 0.67 when all possible precautions in manufacturing and processing are exercised. When the full range of operating variables normally

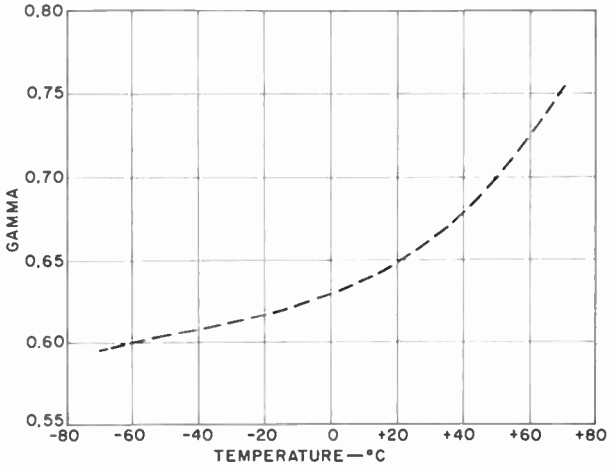

Fig. 13—Vidicon gamma as a function of temperature.

encountered in specific applications is considered, a gamma range of 0.65 ± 0.05 is often quoted for typical vidicon operation. In this context, a variation in gamma over this same general range as the temperature is varied by 120°C is not severe.

Conclusions From Thermal-Environment Tests

When adjusted for optimum operation at normal temperature, the vidicon tested was capable of useful operation over a temperature range of 100°C without further adjustment. The center position of this absolute range could be varied to some extent by the selection of appropriate target voltage in the initial setup.

When the target voltage was adjusted to maintain constant dark current, the useful temperature range increased to approximately 150°C (—70°C to 80°C), with improved performance within this

range. Limits of performance are generally determined by the maximum target voltages that can be applied to the vidicon.

When illumination was controlled and adjusted within reasonable limits, the vidicon operates over a 100°C temperature range (—40°C to 60°C) with no loss in signal output. Auxiliary adjustment of target voltage as well as illumination could conceivably extend the constant-signal operating range to 150°C (—60°C to 90°C) or possibly to 200°C (—110°C to 90°C).

Resolution was virtually unaffected over the 200°C temperature range of —100°C to 100°C. However, to realize system resolution in the practical sense it would be necessary to maintain normal vidicon signal-current and dark-current levels.

The lag characteristic was found to be very temperature dependent. At high temperatures, lag tended to decrease and presented no problem. As the temperature dropped, however, lag increased to a point that would require serious consideration by a system designer. Signal level should be maintained to avoid effects other than temperature which may adversely affect the lag characteristic.

The gamma characteristic of vidicon tubes is also significantly altered by temperature.

MEASUREMENTS ON THE PROPERTIES OF MICROSTRIP TRANSMISSION LINES FOR MICROWAVE INTEGRATED CIRCUITS

By

M. Caulton, J. J. Hughes, and H. Sobol

RCA Laboratories
Princeton, N. J.

Summary—The conformal mapping theories of Wheeler have been used to derive a set of design curves for microstrip transmission lines applicable over a wide range of geometries, frequencies, and substrate materials. Design data are presented for characteristic impedance, wave-length, attenuation, and circuit Q. A broadband in-line coaxial-to-microstrip transition has been developed. This transition is adaptable over a wide variety of substrate sizes and materials and is suitable for connection to microwave integrated circuits. The properties of microstrip lines at S-band were measured on alpha-alumina, sapphire, and polyolefin substrates. The agreement between the measured values and the design curves is good.

Introduction

Advances in microwave solid-state devices and materials technology have led to integrated microwave circuits. The transmission line, a basic element of microwave circuits, is required for matched interconnections, resonators, and filters, and as integral parts of phase shifters, isolators, and circulators. In general, fairly high unloaded Q (low-loss) lines are required for resonant circuits, while relatively high loss per unit length can be tolerated in interconnecting lines because of the very short distances between active elements in an integrated circuit.

In this paper we consider the microstrip transmission line shown in Figure 1. The insulating layer serves as the substrate for either monolithic or hybrid devices and can be a high-resistivity semiconductor or a low-loss ceramic dielectric. Microstrip lines on semiconducting substrates have been previously discussed[1] and the present paper is devoted primarily to a study of the line with a ceramic substrate.

The first extensive study of microstrip lines for propagation of

[1] T. M. Hyltin, "Microstrip Transmission on Semiconductor Dielectrics," *IEEE Trans. Microwave Theory and Techniques*, Vol. MTT-13, p. 777, Nov. 1965.

microwave energy was published nearly fifteen years ago.[2] Much of the earlier disagreement between theory and measurements appears to have been overcome by the recent work of Wheeler.[3,4] Since a significant part of the microwave energy is propagated in the fringe field, circuitry using the microstrip line suffers from cross-coupling difficulties and is also susceptible to detuning due to nearby metallic disturbances. The Triplate or Strip-line structure using two ground planes confines the fringe field, and has been used more extensively than the microstrip line for conventional microwave circuits. However, in integrated circuits, use of the microstrip line, which is nearly a planar structure, is

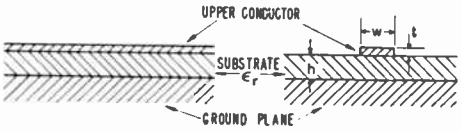

Fig. 1—Microstrip line.

more suitable. Most applications will require a metallic enclosure or packaging for hermetic sealing and strength, and this will confine the fringe field. If the distance from the conductor to the metallic enclosure is several (3 to 5) times the height of the insulating layer, the propagation characteristics are only slightly perturbed. The design data and experimental results presented below are for unshielded lines, and it may be necessary to make some slight corrections for the effects of the enclosure in an actual circuit.

Conventional microstrip lines are usually fabricated on standard Teflon impregnated fiberglass or polystyrene printed circuit boards 1/32 to 1/16 inch thick, and use copper lines of the order of 1/16 to 1/8 inch wide. For integrated circuits alumina, sapphire, beryllia, or high-resistivity semiconductors 10 to 30 mils thick are used as substrates for the lines. The conductors may be copper, aluminum, gold, or silver, and are of the order of 8 to 30 mils wide.

This paper presents a study of the properties of microstrip lines. Theoretical design data based on the work of Wheeler[3,4] are discussed first. A miniature coaxial-to-microstrip transition useful for a wide

[2] F. Assadourian and E. Rimai, "Simplified Theory of Microstrip Transmission Systems," Proc. IRE, Vol. 40, p. 1651, Dec. 1952.

[3] H. A. Wheeler, "Transmission-Line Properties of Parallel Wide Strips by a Conformal-Mapping Approximation," *IEEE Trans. Microwave Theory and Techniques*, Vol. MTT-12, p. 280, May 1964.

[4] H. A. Wheeler, "Transmission-Line Properties of Parallel Strips Separated by a Dielectric Sheet," IEEE Trans. *Microwave Theory and Techniques*, Vol. MTT-13, p. 172, March 1965.

range of substrate dimensions is then described, and, finally, measurements of lines for use in integrated circuits are presented and compared with the theory.

Theoretical Background

The microstrip line has not been amenable to an exact analysis, and until recently, reasonable predictions of characteristics over a wide range of impedances and dielectric characteristics were not available. Approximate analyses by Assadourian[2] and others[5] have provided useful design equations for impedances of less than 50 ohms

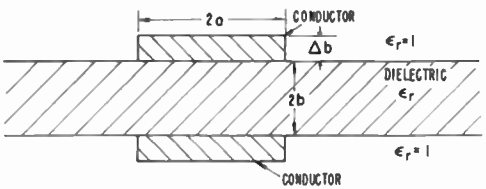

Fig. 2—Parallel plane geometry of Wheeler[3, 4] (equivalent to Figure 1 when $h = b$, $2a = w$, $\Delta b = t$).

or for ratios of the width of the line w to height above the ground plane h (Figure 1) much greater than unity. Somewhat less accurate formulas have been found for impedance levels in excess of 50 ohms or $w/h \leq 1$. The main difficulty in obtaining a complete solution is that it is necessary to take into account the dielectric discontinuity at the insulator boundary, fringe fields, finite conductor sizes, and radiation losses. The approximate theories, which are based on TEM propagation, account for the fringing electrostatic fields, but neglect the dielectric discontinuity. In his more elaborate theory, Wu[6] purports to account for some of the above effects, but the theory has not been reduced to practical terms. The electrolytic tank studies of Dukes[5] are useful in obtaining some information on the phase velocity through a consideration of the "effective dielectric constant" of the line when both the fringe field propagating in air and the field propagating in the dielectric are accounted for. Recently Wheeler[3,4] has published a conformal mapping analysis of TEM propagation that does account for the dielectric discontinuity. Wheeler's calculations are for the parallel-plane waveguide shown in Figure 2, but, with a simple transformation,

[5] J. M. C. Dukes, "An Investigation Into Some Fundamental Properties of Strip Transmission Lines With the Aid of an Electrolytic Tank," *Proc. IEE* (London), Vol. 103B, p. 319, 1956.

[6] T. T. Wu, "Theory of the Microstrip," *Jour. Appl. Phys.*, Vol. 28, p. 299, 1957.

the results are applicable to the microstrip line. The dimensions of Wheeler's parallel-plane guide in Figure 2 apply to the microstrip line of Figure 1 with $2a = w$, $b = h$. The wavelength of the parallel-plane guide is equal to that of the microstrip, and the impedance of the microstrip is one-half the impedance of the parallel-plane guide. It will be shown that Wheeler's results show fairly good correlation with

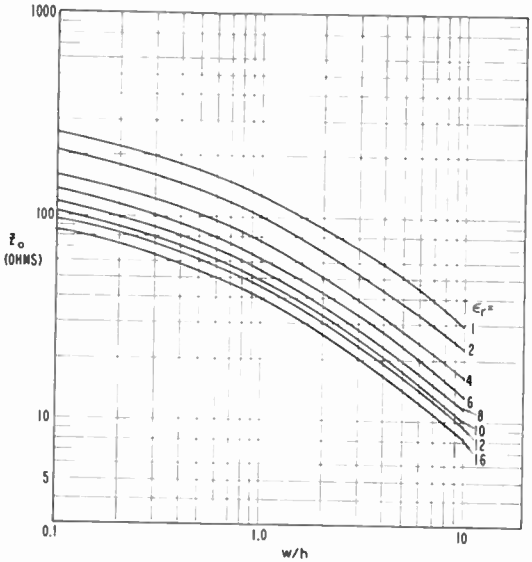

Fig. 3—Calculated characteristic impedance Z_0 of microstrip lines as a function of w/h and ϵ_r.

experiment for all lines, including those with w/h ratios less than unity and impedances in excess of 50 ohms. The above transformations were applied to Wheeler's results, and the characteristic impedance Z_0 and wavelength λ were calculated for a zero-thickness conductor and an infinitely wide ground plane. The characteristic impedance as a function of w/h is plotted in Figure 3. The wavelength λ normalized to that of a microstrip line completely imbedded in a dielectric (λ_{TEM}) is shown in Figure 4.

Since the first-order effect of a line of finite thickness t is to increase the capacitance, an approximate correction can be made by using an effective width,

$$w_{eff} = w + \Delta w \tag{1}$$

where

$$\Delta w = \frac{t}{\pi}\left(\ln\frac{2h}{t} + 1\right) \tag{2}$$

for $w/2 > h/(4\pi) > t$. The correction factor Δw can be derived from the low-impedance closed-form approximations or from the theory of

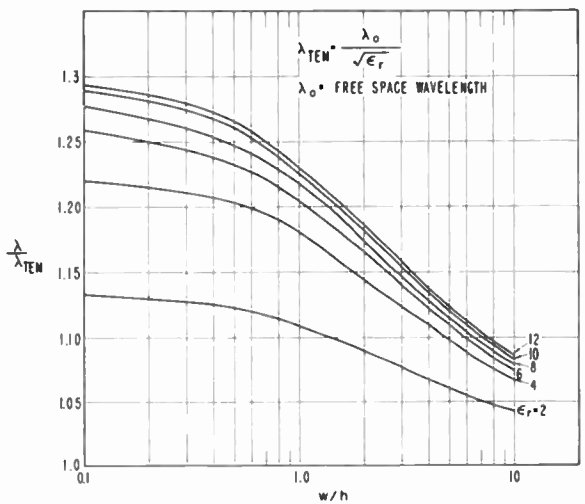

Fig. 4—Calculated normalized wavelength as a function of w/h and ϵ_r.

Wheeler. The value of the correction $\Delta w/t$ is plotted for various h/t ratios in Figure 5. The effective width should be used when applying the design curves. Wheeler cautions regarding the effectiveness of this edge correction for high-dielectric-constant media, since $\Delta w \rightarrow 0$ for $\epsilon >> \epsilon_0$. However, Equation (2) should be regarded as a limit correction for lines where the fringe fields make up an appreciable part of the total fields, a condition that applies for the lines studied in this paper.

The loss per unit length of a line may be expressed as

$$\alpha = \alpha_{c1} + \alpha_{c2} + \alpha_d = \frac{r_1 + r_2}{2Z_0} + \frac{gZ_0}{2}. \tag{3}$$

where

α_{c1} is the loss in the conductor in nepers/meter,

α_{c2} is the loss in the ground plane in nepers/meter,

α_d is the dielectric losses in nepers/meter.

r_1 and r_2 are the effective series resistance per meter of the conductor and ground plane, respectively, and

g is an effective conductance representing the total dielectric losses in mhos per meter.

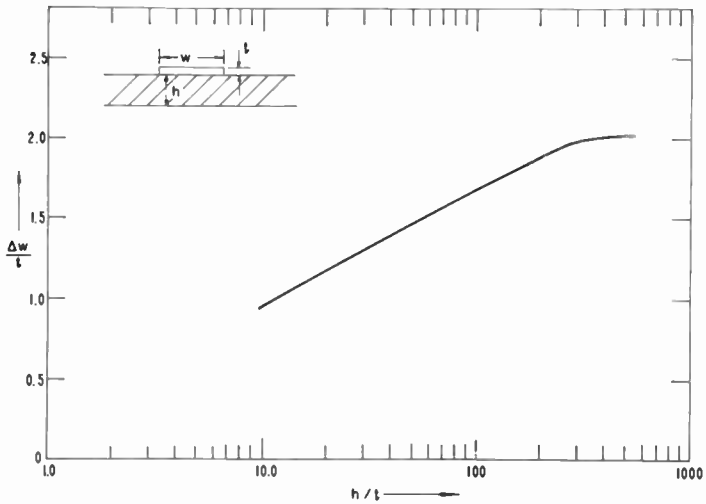

Fig. 5—Line-width correction for finite-thickness substrates.

The conductor losses $\alpha_c = \alpha_{c1} + \alpha_{c2}$ can be calculated approximately assuming a uniform current across the width of the conductor and also assuming that the ground-plane current is distributed uniformly under the conductor. Subject to these approximations, the conductor loss is

$$\alpha_c = \alpha_{c1} + \alpha_{c2} = \frac{\sqrt{\pi f \mu}}{2Z_0 w}\left(\frac{1}{\sqrt{\sigma_{c1}}} + \frac{1}{\sqrt{\sigma_{c2}}}\right), \tag{4}$$

or

$$\alpha_c = \frac{R_{s1} + R_{s2}}{2Z_0 w}, \tag{5}$$

where σ_c is the conductivity in mhos per meter and R_s is the surface resistivity in ohms per square. A normalized conductor attenuation may be calculated using the impedance data presented in Figure 3.

Figure 6 shows curves of the conductor attenuation α_c in db per meter normalized as shown on the figure for a wide range of parameters. The dielectric loss α_d is independent of geometery and is given as

$$\alpha_d = \frac{gZ_0}{2} = \frac{\omega}{2}\left(\frac{\mu}{\epsilon'}\right)^{\frac{1}{2}} \frac{\epsilon''}{\epsilon'}\epsilon', \tag{6}$$

where ϵ' is the real part of the permittivity of the dielectric and ϵ'' is the imaginary part of the permittivity.

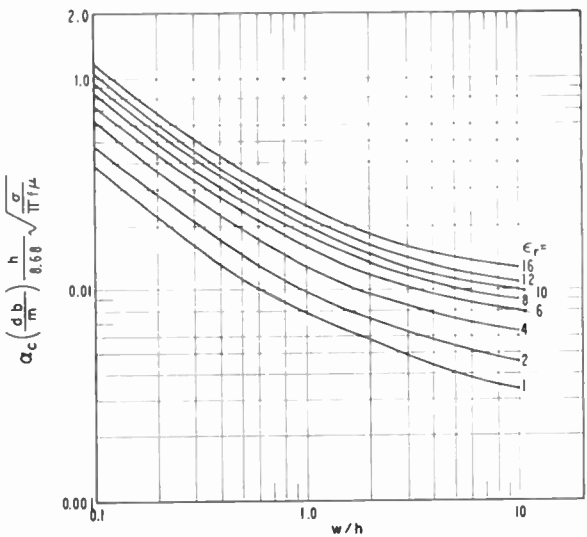

Fig. 6—Calculated normalized conductor loss as function of geometry w/h and ϵ_r (MKS units).

As an estimate of the performance of the microstrip line in circuit applications, consider a $\lambda/4$ shorted resonator. The unloaded Q of the resonator can be expressed as

$$\frac{1}{Q} = \frac{1}{Q_c} + \frac{1}{Q_d}, \tag{7}$$

where Q_c is the quality factor of the conductors and Q_d is the quality factor of the dielectric.

Q_c for the case of the conductor and ground plane fabricated from the same material is

$$Q_c = \frac{\omega_0 Z_0^2 C}{r_s}, \tag{8}$$

where ω_0 is the resonant frequency, C is the capacitance per unit length, and r_s is the total series conductor loss per unit length. Q_c can be expressed in normalized form as

$$\frac{Q_c}{h\sqrt{f_{GHz}}} \frac{6}{\sqrt{\sigma_r}} = \frac{\lambda_{TEM}}{\lambda} \frac{w}{h} Z_0 \sqrt{\epsilon_r}. \tag{9}$$

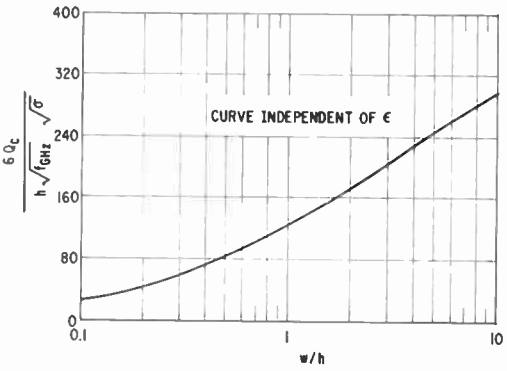

Fig. 7—Calculated normalized Q_c as function of w/h (MKS units).

The results of Figures 3 and 4 may be used to calculate the normalized conductor Q_c presented in Equation (9). This is plotted in Figure 7. The dielectric quality factor is the ordinary Q value of the material used.

The design data given above apply to microstrip lines in general. Application of the results applied to microstrip lines of the sizes used for typical integrated-circuit applications is discussed later.

Coaxial-to-Microstrip Transition

The standard input and output connector of most microwave equipment (X-band and lower) is coaxial. It is necessary, therefore, to use a transition from the substrate circuitry to the external coaxial equipment. For testing and application of integrated microwave circuits, it is desirable to have a small inexpensive broad-band transition that is easy to connect and can accommodate a wide range of substrates, line sizes, and materials.

The transition from a coaxial line to a microstrip line can be either the "in-line" type, where the coaxial axis is parallel to the plane of the microstrip line, or the "right-angle" type, where the axes are perpendicular. The right-angle type has been used in standard-size commercial equipment but requires the insertion of a pin through the ground

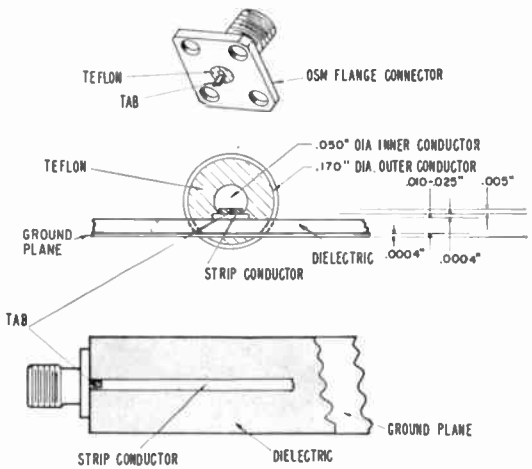

Fig. 8—In-line coaxial-to-microstrip transition.

plane and insulator and, in general, does not satisfy the requirements for a versatile and inexpensive transition. The in-line transition, on the other hand, can satisfy these requirements and was used in the work reported below. It is illustrated in Figure 8. The coaxial connector used is in the miniature 50-ohm OSM* series and is suitable for use with integrated circuits over a wide frequency band. This transition is simple to design when the coaxial center-pin diameter is of the order of the line width, as is the case for substrates with thicker dielectrics and lower ϵ_r. On the other hand, for thin substrates where the thickness is much less than the distance between the inner and outer coaxial conductor, a capacitive discontinuity can exist. If this discontinuity is large enough to warrant tuning, a limited bandwidth will result.

The thicker dielectric and lower ϵ_r is typified by a copper-clad circuit board of Polyguide† ($\epsilon_r = 2.32$). Here a line width of the order of the diameter of the OSM center conductor (0.050 inch) is required for a 50-ohm line ($w/h \cong 2.8$). A reasonable match with a minimum

* Trademark of Omni-Spectra.
† Tradename.

capacitive discontinuity is obtained simply by extending the center pin over the microstrip line on the substrate.

Microwave integrated circuits usually have thin high-dielectric-constant substrates. In the tests reported here alumina ($\epsilon_r = 9.0$), alpha-alumina (polycrystalline sapphire, $\epsilon_r = 9.9$), and sapphire with $\epsilon_r = 9.35$, 11.7 were used. For thicknesses of 0.010 to 0.015 inch the line width is of the order of the thickness; the 0.050-inch-diameter center pin of the OSM connector will form a capacitive discontinuity.

Hyltin[1] tapers the coaxial line until the center pin is of the order of the line width. It is possible to avoid this tapered section by shearing

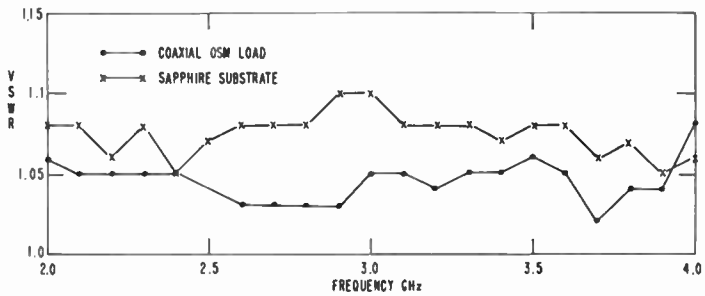

Fig. 9—VSWR as a function of frequency (GHz) for in-line transition.

the pin flush with the end of the coaxial connector and fastening on the end of the pin a thin metal strip that overlaps the microstrip line, as shown in Figure 8. The width of the strip or tab is equal to or less than the width of the strip conductor. This junction results in a capacitance discontinuity, but calculations show that this is less than 0.01 pf. Measured values of the VSWR over S-band are less than 1.1 for a w/h of 0.8 to 1.0 on a 10-mil substrate of alpha-alumina for this transition (Figure 9). Low VSWR's were measured from L-band to X-band. At 10 GHz the VSWR was as high as 1.2. However, the line did not extend to the end of the substrate, with the result that a tab smaller than the line presented a series inductive discontinuity. This could have been removed by more carefully adjusting the size of tab on the line or by extending the line to the edge of the substrate. A photograph of a transition jig that quickly attaches to various size substrates is shown in Figure 10.

The same transition was used successfully on the larger size lines ($\cong$ 0.050 inch) constructed on Polyguide of 0.022-inch thickness; the VSWR, while not quite as good, is under 1.15). The 0.050-inch center conductor extending over the microstrip line gave comparable matches

to the tab. This would be expected, since the diameter of the center conductor and the Stripline width are now close in size.

It is concluded that this simple in-line coaxial-to-microstrip transition is suitable over a wide range of frequencies and for a wide variety of substrates.

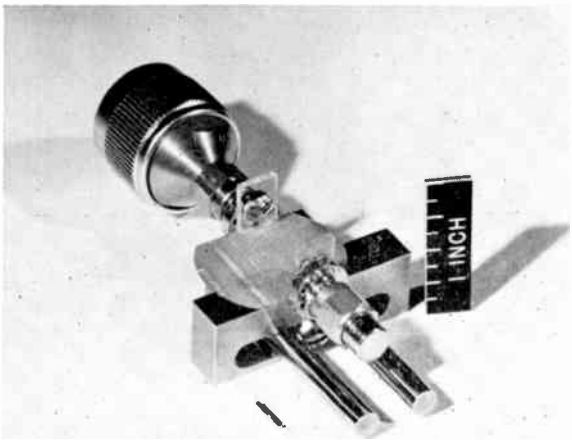

Fig. 10—Photograph of coaxial-to-microstrip transition (microstrip transmission line on ceramic substrate attached).

Properties of Microstrip Lines on Substrates

With the establishment of a satisfactory transition, three properties of microstrip lines were measured: (1) characteristic impedance Z_0, (2) wavelength λ, and (3) the attenuation α.

Determination of Z_0

Three different substrate materials were used for measurements of Z_0. These were Polyguide ($\epsilon_r = 2.32$, $h = .022$ inch), alpha-alumina (GE Lucalox†, $\epsilon_r = 9.9$, $h = 0.10$ inch), and sapphire with two orientations of the C axis. The sapphire substrate with the C-axis at an angle of 33° from the plane of the substrate has an effective ϵ_r calculated to be 9.9 for TEM propagation, while for a C-axis in the plane of the substrate the ϵ_r is stated in the literature to be 9.35.

The measurements of Z_0 were made by determining the VSWR using a GR900 slotted line. This method gives only approximate re-

† Tradename.

Table I—Z_0 as a Function of Line Width w and Substrate Thickness h

Material	h (inches)	t (inches)	w (inches)	w/h	$\sqrt{VSWR_{MAX}}$	Z_0 (ohms)
Polyguide	.022	.0010	.0495	2.23	1.13	56.4
$\epsilon_r = 2.32$			.0540	2.44	1.09	54.6
			.0585	2.68	1.06	53.1
			.0640	2.90	1.11	45.4
			.0695	3.13	1.15	44.0
			.0735	3.36	1.19	42.4
Alpha-alumina	.010	.0002	.0067	.67	1.11	55.6
$\epsilon_r = 9.9$			.0077	.77	*	50.0
			.0087	.87	*	50.0
			.0097	.97	1.09	46.5
			.045	4.5	2.61	19.1
Sapphire	.0158	.0002	.0104	.66	1.16	58.1
$\epsilon_r = 9.9$			.0125	.74	*	50.0
			.0136	.86	*	50.0
			.0158	1.0	1.10	46.2
Sapphire	.0095	.0004	.0066	.695	1.17	58.6
$\epsilon_r = 9.35$			.0085	.895	1.06	53.0
			.0087	.915	†	50.0
			.0095	1.0	†	50.0
			.0110	1.155	1.11	45.0
			.0140	1.47	1.23	40.5
			.0155	1.63	1.30	38.0
			.0404	4.25	2.47	20.6

* VSWR < 1.09

† VSWR < 1.10

sults. Our accuracy in S-band for 50 ohms is of the order of ±2.5 ohms. The VSWR as a function of frequency showed long-line characteristics giving VSWR maxima and low minima at appropriate frequencies across the band. The Z_0 was then calculated as 50 ohms divided or multiplied by the geometric mean of these values, which was close to the square root of the maximum VSWR. The results for various substrates and line widths are shown in Table I.

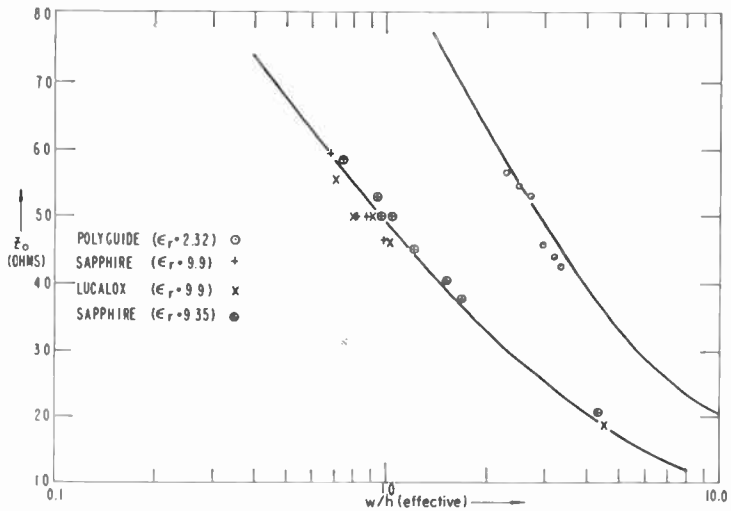

Fig. 11—Characteristic impedance Z_0 as a function of w/h of microstrip line.

Figure 11 shows curves (Z_0 versus w/h) extracted from Figure 3 for the values of ϵ_r used in our measurements. The appropriate w/h correction, as discussed earlier is made. Thus $w_{eff} = w_{measured} + \Delta w$, where Δw is computed from Figure 5. This correction may be a limit, but the fringe fields still make up an appreciable part of the total field, and it is expected that Figure 5 should give a valid correction.

The w/h of Table I are modified to w_{eff}/h and are plotted in Figure 11. It is apparent that the adjusted values agree reasonably well with the theory of Wheeler.

Determination of λ

The values of λ for typical values of w/h have been measured on samples of both the sapphire and Polyguide substrates. The wavelength was determined by measuring the change in position of minima

as the distance to either an open or a short circuit was varied. In Figure 12 the values for some sample measurements of λ are compared with curves extracted from the data of Figure 4. The errors in these measurements overlay the solid curves, and it is again concluded that the theory predicts the measured wavelength reasonably well.

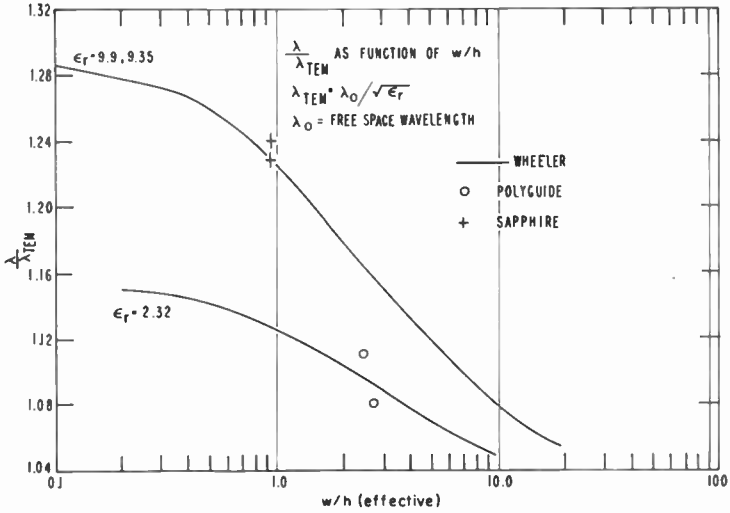

Fig. 12—Normalized wavelength as function of w/h of microstrip line.

Determination of α

The attenuation was determined by measuring the VSWR when the line was terminated by an open or short circuit. A good transition was assured by checking the VSWR for a well-matched line. Two methods of measuring the attenuation of the line were used. In one case the attenuation was measured for open- or short-circuited lines of varying lengths. The change in attenuation removes the effect of residual losses in the measuring system. A second method involved measuring the losses in the residual connectors and subtracting this from the total attentuation measured. The two methods gave reasonable agreement.

Table II gives the results of the loss measurements for sapphire and Polyguide substrates. The values of attenuation calculated from Figure 6 are also shown. The agreement between theory and measurement is considered well within the experimental error. The Q of quarter-wavelength resonators using these lines is calculated to be 58 and 87, respectively. The main loss mechanism here is the conduc-

tor loss; the dielectric loss is negligible. To obtain a higher Q, it is necessary to use thicker substrates. For example, an X-band resonator on a 25-mil-thick sapphire substrate has a theoretical Q of 285.

The dielectric loss plays a more important role in circuit Q when using high-resistivity silicon as a substrate. The substrate or "dielectric" Q is given as

$$Q_d = \omega\epsilon\rho \tag{10}$$

At low frequencies the primary loss for the lines is in the silicon substrate. As an example, a 2000 ohm-cm substrate results in a Q_d

Table II—Calculated and Measured Attenuation ($f = 2.25$ GHz)

Material	$\frac{w_{eff}}{h}$	Measured Loss (db/cm)	Calculated Loss (db/cm)
Polyguide			
$\epsilon_r = 2.32$	2.44	$.015 \pm .005$	.013
Sapphire			
$\epsilon_r = 9.35$	.93	$.08 \pm .02$	.074

of about 25 at 2 GHz. At higher frequencies the loss terms for the conductor and substrates are more nearly equal. With gallium arsenide of extremely high resistivity, on the other hand, a circuit Q comparable to that of ceramic substrates can be obtained.

Conclusions

A simple wide-band in-line microwave coaxial-to-microstrip transition proved very effective in studying microstrip transmission lines for integrated circuits.

Calculations based on Wheeler's theory were consistent with measurements of characteristic impedance, wavelength, and attenuation on sapphire, high-purity alumina, and Polyguide substrates. A set of design curves for use with microstrip transmission lines has been extracted from Wheeler's theory. It is expected that these can be used for the design of microstrip lines with reasonable accuracy.

Acknowledgment

The assistance of R. E. Chamberlain in the preparation of substrates is gratefully acknowledged.

EFFICIENT SEQUENTIAL DETECTION IN THE PRESENCE OF STRONG LOCALIZED SIGNAL INTERFERENCE

By

H. M. Finn and R. S. Johnson

RCA Missile and Surface Radar Division
Moorestown, N. J.

Summary—A class of sequential interference-rejection modes has been designed and subjected to a performance analysis. These tests, using a maximum of two steps, introduce a parameter-consistency test at each of the sequential steps employed in order to accomplish the desired interference-signal rejection. The newly developed sequential modes are shown quantitatively to significantly reduce the system cost over the use of a fixed-sample test incorporating the same discrimination criterion.

A COMMON ENVIRONMENT encountered in a radar complex includes, in addition to additive thermal noise and spatially distributed clutter, strong localized interfering signals that have the same waveform as the transmitted signal but are unsynchronized and randomly received. This paper describes an efficient multiple-stage decision processor for performing the radar-surveillance mission of detecting a point target in such an environment.

The stochastic model of the strong localized, random interfering signal that is employed in this paper involves the selection of a Bernoulli trial probability $\overline{P}$ representing the probability that any range-doppler cell in the parameter space of admissible targets will be interfered with. The 'success' event of the Bernoulli trial (the occurrence of a strong localized interfering signal in a resolution cell) is assumed, in this model, to be statistically independent from one resolution cell to another and also between transmissions. The interfering signals are assumed to be so intense that the occurrence of one in a parameter-resolution cell *assures* that the sampled matched-filter output of the cell will be larger than any established single transmission threshold. That is to say, a value of unity is assumed for the conditional probability of a threshold crossing of a resolution-cell output when an interfering signal is present in the cell.

It is also assumed that the transmitted beam may "step through" the surveillance volume, and that the dwell time at a beam position may vary from one beam position to the next. (Electronically steer-

able array radar systems permit such beam-steering flexibility.) At each beam position, the detection mode may be viewed as a statistical test of the hypotheses as to the presence or absence of target backscattering within the noise and interference-signal environment. The decision-processor framework of the two-alternative test developed here has a maximum of two sequential steps. Discrimination against the randomly distributed strong localized-signal interference is accomplished by employing a number of transmissions at each sequential step and requiring some specified consistency in the parameters of the received signals for these transmissions within a sequential step and from one sequential step to another.

More specifically, N_1 transmissions are employed on the first sequential step; at each resolution cell and for each transmission of this first step, the linearly detected and sampled-matched filter output is initially compared with a single pulse threshold β_1. The second or confirmation sequential step is only employed when crossings of the β_1 threshold have occurred in a common parameter resolution cell on at least M_1 of the N_1 first-step transmissions. If this parameter-consistency test requirement is not met on the first step, the no-target hypothesis is accepted, and the beam is moved to a new beam position for a new hypothesis test. N_2 transmissions are used whenever the second sequential step is employed and here again both a single-pulse threshold β_2 and a sum threshold M_T are employed. In all cases, the time interval between single transmissions is assumed to be longer than the correlation time of the clutter so that statistical independence of the noise samples becomes a valid assumption. Thus, the target-present hypothesis is accepted only when the sum of the single-transmission threshold crossings on the first and second sequential steps in a common resolution cell exceed M_T and where at least M_1 of these single-transmission threshold crossings occurred on the first step. The ratio of the average received-signal energy to the thermal-plus-clutter noise-power density ($\overline{X}$) is assumed to be the same for each transmission on both sequential steps. This sequential interference rejection mode is in effect a multiple-stage implementation of a fixed-sample-size test (single-stage test) discussed by Linder and Swerling.[1]

The multiple-stage decision processor is a member of a relatively new class of radar detection modes that permit a change of the radar

[1] I. W. Linder and P. Swerling, "Performance of the 'Double-Threshold' Radar Receiver in the Presence of Interference," (U) RM-1719 ASTIA Doc. AD 115366.

'policy' from one transmission to another (see Finn[2-4], Brennan and Hill[5], and Baum[6]). This class of test is free of the fundamental constraint imposed in the sequential probability ratio test (Wald[7, 8]), namely, that the same 'experiment' be employed at each sequential step.

The expressions for the detection and false-alarm probabilities (P_D and P_{FA}) are developed for the specified stochastic properties of the environment and the hypothesized target characteristics, and these expressions are then set equal to the required values P_{D_0} and P_{FA_0}. These two probability equations are functions of the design parameters N_1, β_1, M_1, M_T, N_2, β_2, $\overline{X}$ and become the constraint relationships of the optimization procedure.

The cost function $\overline{C}$ to be minimized is defined as $\overline{C} = \overline{N}X$, where $\overline{N}$ is the average number of transmissions employed. Since this analysis is concerned with situations where the a priori probability of the occurrence of a target at a beam position is small, it is justifiable to design a mode aimed at minimizing the cost for the no-target environment. The design strategy involves the selection of a design vector $[N_1, \beta_1, M_1, M_T, N_2, \beta_2, \overline{X}]$ meeting the P_{D_0} and P_{FA_0} requirement and minimizing the no-target-environment cost function C. This strategy typically involves relaxing the first-step thresholds (β_1 and M_1) so that the first-step cost ($N_1\overline{X}$), which must be performed at every position, is kept low. The second or confirmation step, which is only infrequently employed in the no-target environment (say typically 6% of the time), involves a larger set of transmissions to determine the final detection and false-alarm probability requirement. In this way, a minimum cost can be achieved. The analytical procedure for accomplishing this optimization is detailed later.

---

[2] H. M. Finn, "A New Approach to Sequential Detection in Phased-Array Radar Systems," *Proc. Nat. Winter Convention on Military Electronics*, Vol. II, p. 4-3, 1963.

[3] H. M. Finn, "Energy Variant Sequential Detectors for Fluctuating Targets," *Proc. Symposium on Electronically Scanned Array Techniques and Applications*, RADC TDR-64-225, Vol. I, July 1964.

[4] H. M. Finn, *Efficient Multiple Stage Decision Processors for Radar Surveillance*, Doctoral Dissertation, Univ. Pennsylvania, 1965.

[5] L. E. Brennan and F. S. Hill, "A Two-Step Sequential Procedure for Improving the Cumulative Probability of Detection in Radars," *Trans. IEEE PTGME*, July/Oct. 1965.

[6] R. F. Baum "Simple Sequential Detection Tests," *Proc. IEEE* (Cor.) Oct. 1964.

[7] A. Wald, *Sequential Analysis*, John Wiley, New York, 1943.

[8] A. Wald, *Statistical Decision Functions*, John Wiley, New York, 1950.

Design and Performance Data

Typical sets of design and performance curves for the developed modes are presented in Figures 1 through 7. The optimum design parameters are shown in Figures 4 and 5 as a function of the effective number of radar resolution cells, where the fixed parameters are the detection and false-alarm probabilities and the Bernoulli-trial strong-signal interference probability $\bar{P}$. The target type hypothesized for

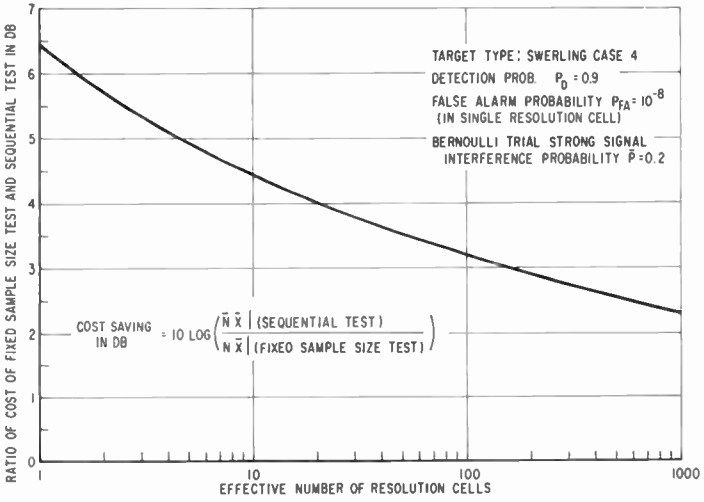

Fig. 1—Cost reduction of sequential test over the use of fixed-sample-size test designed to achieve the same specified performance when operating in strong localized signal interference environment.

these sample computations is the Swerling Case #4. For this model, statistical independence of the target cross section from one transmission to the next is assumed. Since the computer search procedure for the minimum cost function yields a number of sets of surveillance design parameters (see Table II) having the same P_D and P_{FA}, all with $\bar{C}$ close to the minimum, other parameters can be considered in making the final selection of the seven-dimensional design vector. The optimum sets of design parameters appear in Table I.

Optimum design parameters for fixed-sample-size tests have also been developed based on the same type of parameter consistency test and designed to achieve the same sets of error probabilities as the newly designed sequential modes when operating in identical environments. These fixed-sample-size, or uniform-search, modes provide the major basis of comparison of the costs of the developed multiple-

Table I—Optimum Design Parameters of Two-Step Maximum Sequential Test Designed for Operation in Strong-Localized-Signal-Interference Environment (Target Type—Swerling Case #4, Detection Probability $P_D = 0.9$, and Single-Cell False-Alarm Probability $P_{FA} = 10^{-8}$.)

N_F	M_1	N_1	M_T	N_2	$\overline{X}$	β_1	β_2	$\overline{C}$
Bernoulli Trial Strong Signal Interference Probability $\overline{P} = 0.05$								
1	2	3	15	22	8.8	2.209	2.417	25.03
10	3	5	13	17	6.487	2.497	2.435	39.90
100	4	6	12	13	7.857	2.526	2.425	55.46
1000	7	12	15	15	4.96	2.375	2.337	65.19
Bernoulli Trial Strong Signal Interference Probability $\overline{P} = 0.10$								
1	3	5	23	33	4.475	2.136	2.168	30.04
10	5	8	22	27	4.886	2.212	2.124	47.26
100	8	13	23	25	4.320	2.187	2.136	63.22
1000	11	18	24	22	3.998	2.173	2.089	78.60
Bernoulli Trial Strong Signal Interference Probability $\overline{P} = 0.20$								
1	5	7	37	46	4.345	1.868	1.976	40.22
10	8	11	34	37	4.807	1.972	2.00	63.41
100	11	15	32	30	5.016	2.032	2.034	85.84
1000	16	22	35	28	4.385	1.980	1.986	105.99
Bernoulli Trial Strong Signal Interference Probability $\overline{P} = 0$ (No Interference Case)								
1	1	2	6	13	6.923	2.82	3.01	17.23
10	1	2	4	8	10.776	3.52	3.37	25.10
100	1	2	3	5	14.772	4.097	3.613	32.89
1000	2	4	4	6	9.952	3.409	3.394	43.02

stage decision processors. For the fixed-sample-size test, N transmissions are employed and the target is declared present only when the single-pulse receiver threshold β has been exceeded by at least M of the N transmissions in a common resolution cell. An optimization program has also been developed for finding the fixed-sample-size test

Table II—Typical Set of Sequential Test Design Parameters Yielding the Same Surveillance Specifications and Comparable Costs (Near-Minimum-Cost Designs)

Bernoulli Trial Strong Signal Interference Probability $\overline{P} = 0.10$								
N_F	M_1	N_1	M_T	N_2	$\overline{X}$	β_1	β_2	$\overline{C}$
100	7	11	21	22	5.062	2.257	2.118	63.79
100	7	11	21	21	5.110	2.259	2.055	63.91
100	7	11	20	22	5.085	2.261	2.283	63.86
100	7	10	20	22	5.667	2.139	2.271	64.81
100	7	10	19	22	5.732	2.149	2.486	65.04
100	7	11	20	21	5.114	2.261	2.223	63.85
100	8	12	21	21	4.845	2.100	2.207	63.90
100	8	13	23	25	4.320	2.187	2.136	63.20 ←Min. Cost Design
100	9	14	24	26	4.103	2.051	2.178	63.41
100	8	12	23	26	4.687	2.089	2.175	63.71
100	6	9	24	25	6.205	2.363	1.774	67.74
100	6	9	22	24	6.157	2.354	1.949	67.20
100	6	9	22	22	6.187	2.352	1.841	66.66
100	6	10	18	19	5.662	2.487	2.313	67.19
100	9	12	21	22	5.244	1.872	2.462	68.39
100	7	13	23	23	4.453	2.464	1.929	67.70

$[M, N, \beta, \overline{X}]$ satisfying the specified detection and false-alarm probability, and minimizing the cost for a given single-cell interference probability $\overline{P}$ and effective number of resolution cells N_F. The optimization procedure is similar to that employed for the sequential test, but is much simpler because only four design parameters are involved. Optimum sets of design parameters for the fixed-sample-size test are given in Figure 7.

The ratio of the cost of the fixed-sample-size test to the cost of the sequential test for the same set of surveillance conditions provides a

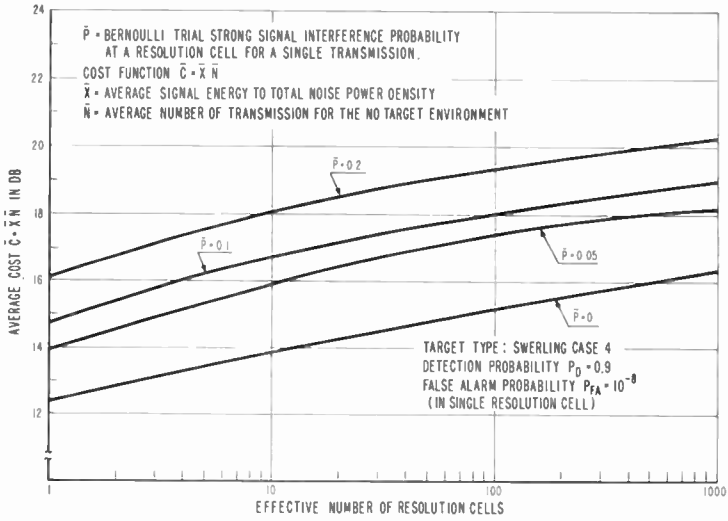

Fig. 2—Average cost of two-step-maximum sequential detection mode with parameter-consistency test of each sequential step when operating in strong localized signal interference environment.

useful measure of the efficiency of the sequential test. For example, Figure 1 shows that the efficiency is a monotonically decreasing function of the number of resolution cells involved on the test. The reduction in cost of the sequential test over the use of the fixed-sample-size

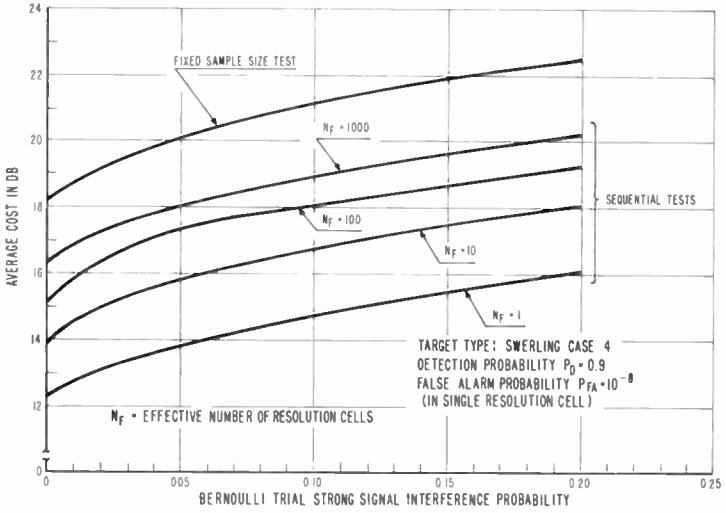

Fig. 3—Average cost of sequential-detection modes and fixed-sample-size test as a function of the strong signal interference probability.

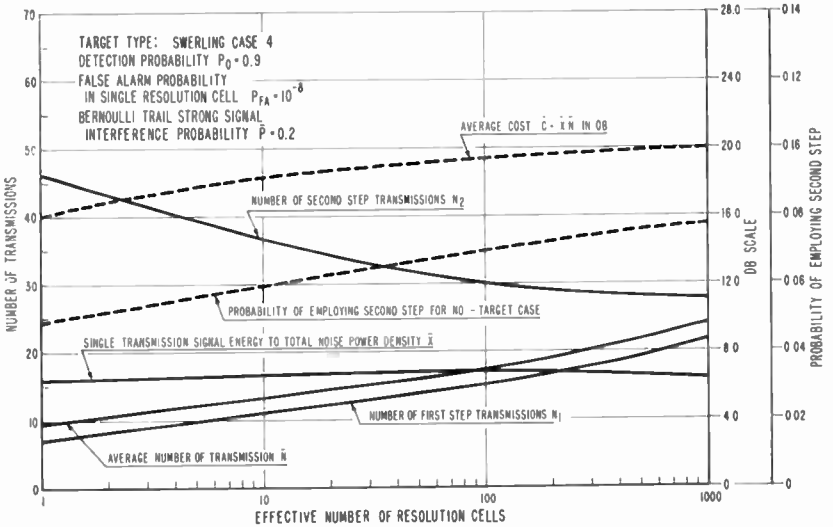

Fig. 4—Number of transmissions employed in two-step-maximum sequential-detection mode designed for operation in strong localized signal interference environment.

test ranges from about 6.5 db for a single-resolution-cell radar to 2.3 db for the 1000-resolution-cell case. The price paid for discriminating against strong localized signal interference can be obtained from the cost data presented in Figures 2 and 3. For example,

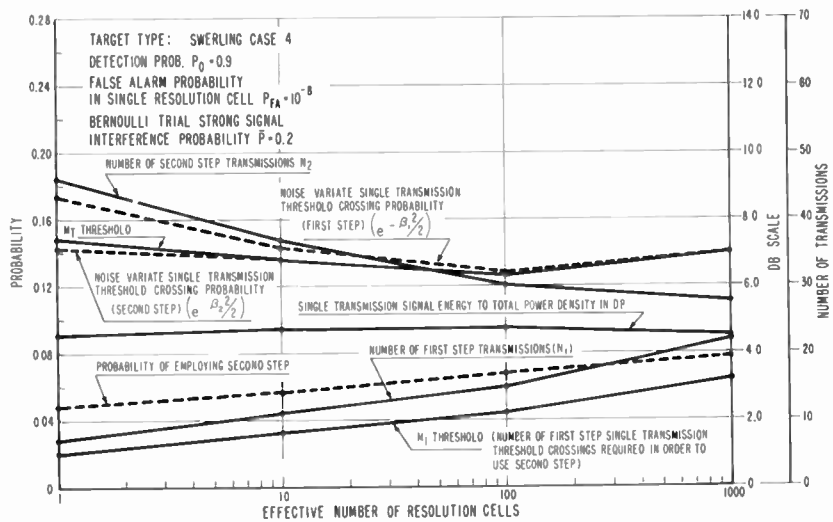

Fig. 5—Design parameters for two-step-maximum sequential-detection mode designed for operation in a strong localized signal interference environment.

the detection-process cost for discriminating against a strong interfering signal with a single-cell-occurrence probability of 0.1 is only approximately 3 db greater than the cost for achieving the same detection and false alarm probability ($P_D = 0.9$ and $P_{FA} = 10^{-8}$ for this case) when the interferring signal is absent. When these optimized modes are employed, the prices paid for handling strong signal interference with relatively high frequencies of occurrence is surprisingly small.

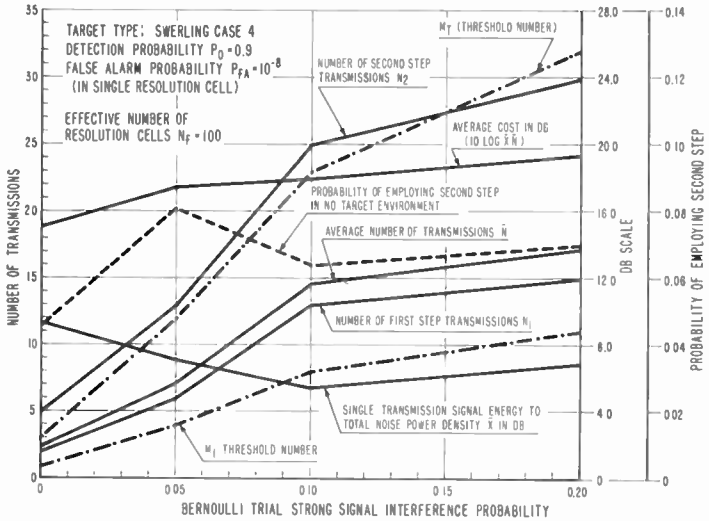

Fig. 6—Number of transmissions as a function of the strong signal interference probability for a two-step-maximum sequential detector.

Analytical Formulation of the Optimization Procedure

The seven-dimensional design vector $[M_1, N_1, M_T, N_2, \beta_1, \beta_2, \bar{X}]$ minimizing the cost $\bar{C}$ and satisfying the specified detection and false-alarm probabilities involves three continuous variables β_1, β_2, $\bar{X}$ and four integral-valued variables M_1, N_1, M_T, N_2. For each selection of these four integral-valued variables, the optimization procedure involves the use of Lagrange multipliers to find the vector $[\beta_1, \beta_2, \bar{X}]$ that minimizes the cost and satisfies the specified P_D and P_{FA}. A computer search procedure is then initiated at the lattice points of the integral-valued coordinates M_1, N_1, M_T, N_2 in order to find the smallest of these minimum costs. The search continues until a lattice point is found where all surrounding lattice points yield a larger cost. This section discusses the formulation of the constraint relationships P_D

and P_{FA}, the cost function $\bar{C}$, and the optimization procedure for the sequential test.

The constraint relationships of the optimization procedure are the detection and false-alarm probability equations. These probabilities express for the target present and no-target present cases, respectively, the joint probabilities of meeting the criterion for accepting the target-present hypothesis on the first and second sequential steps.

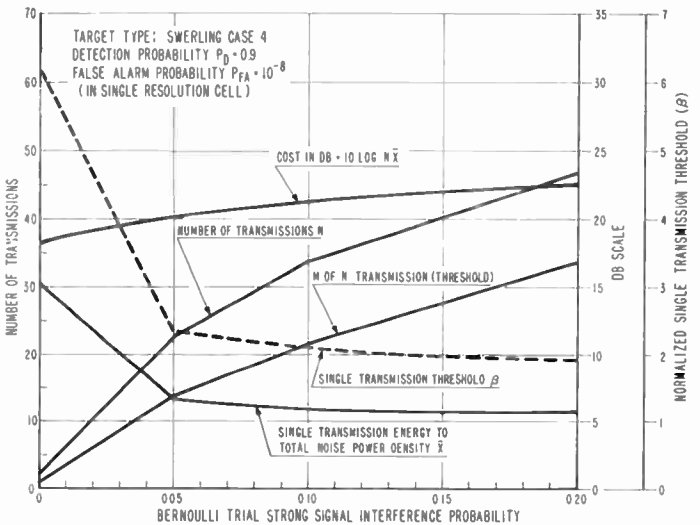

Fig. 7—Optimum design parameters of fixed-sample-size test operating in strong signal interference environment.

These probabilities reflect the imposed decision rule and the specified stochastic properties of the target and interfering signals.

The detection probability (P_D) is

$$P_D = \sum_{K=M_1}^{N_1} b(K; P_1^{(1)}, N_1) \sum_{J=M_T-K}^{N_2} b(J; P_2^{(1)}, N_2) \tag{1}$$

where

$$b(K; P_i^{(1)}, N_i) = \binom{N_i}{K} P_i^{(1)K} (1 - P_i^{(1)})^{Ni-K}$$

is the binomial probability of K of N_i threshold crossings when the probability of a single transmission threshold crossing for the target-present hypothesis (H_1) is $P_i^{(1)}$ for the ith step, and $i = 1, 2$.

This single-transmission threshold-crossing probability $P_i^{(1)}$ in-

cludes all possible combinations of events leading to threshold crossings. The threshold crossing event after a transmission in a resolution cell may be due to the presence of a signal-plus-noise variate, a strong localized interfering signal, or a combination of these events:

$$P_i^{(1)} = P_{Di}\,(1-\bar{P}) + P_{Di}\,(\bar{P}) + \bar{P}(1-P_{Di}), \tag{2}$$

or

$$P_i^{(1)} = \bar{P} + P_{Di}(1-\bar{P}), \tag{3}$$

where P_{Di} is the probability that the threshold crossing event is due to the presence of the signal-plus-noise variate. P_{Di} for this analysis may be expressed as

$$P_{Di} = \int_{x=\beta_i}^{\infty} \int_{\alpha_i=0}^{\infty} x \exp\left\{-\frac{x^2+\alpha^2}{2}\right\} I_0(\alpha x)\, f(\alpha; \bar{X})\, d\alpha dx, \tag{4}$$

where β_i is the normalized single-transmission threshold, and the integrand

$$f(x/\alpha)\, dx = x \exp\{-(x^2+\alpha^2)/2\}\, I_0(\alpha x)\, dx \tag{5}$$

is the well-known Rice distribution and, in this case, represents the conditional-probability density function of the linearly detected matched-filter output on the hypothesis that the input signal energy to total noise power density ratio is $(\alpha^2/2) f(\alpha, \bar{X}) d\alpha$ in Equation (4) is the probability density function of the variate α. For the computations given here, the Swerling Case #4 target has been selected, where

$$f(\alpha, \bar{X})\, d\alpha = \frac{2\alpha^3}{\bar{X}^2} \exp\left\{-\frac{\alpha^2}{\bar{X}}\right\} d\alpha \tag{6}$$

and where the α are assumed to be statistically independent between transmissions and sequential steps.

Substituting Equation (6) into Equation (4) and performing the indicated integration,

$$P_{Di} = \left[1 + \frac{\beta_i^2 \bar{X}}{(\bar{X}+2)^2}\right] \exp\left\{-\frac{\beta_i^2}{\bar{X}+2}\right\}. \tag{7}$$

In a similar manner, the false-alarm probability in a single resolution cell, P_{FA}, may be expressed

$$P_{FA} = \sum_{K=M_1}^{N_1} b\ (K, P_1^{(0)}, N_1) \sum_{J=M_T-K}^{N_2} b\ (J, P_2^{(0)}, N_2), \tag{8}$$

where $P_i^{(0)}$ is the single-transmission threshold-crossing probability in a resolution cell on the condition that the no-target hypothesis H_0 is true and is given by

$$P_i^{(0)} = \overline{P} + \exp\left\{ -\frac{\beta_i^2}{2} \right\} (1 - \overline{P}). \tag{9}$$

In Equation (9), the single-transmission threshold crossing probability due to the noise variate alone is $\exp\{-\beta_i^2/2\}$.

For the no-target environment, the cost is

$$\overline{C} = \overline{X}\ [N_1 + N_2 N_F \sum_{K=M_1}^{N} b\ (K, P_1^{(0)}, N_1)\ ], \tag{10}$$

where N_F is equal to the number of resolution cells of the first step. The quantity

$$F_1^{(0)} = \sum_{K=M_1}^{N_1} b\ (K, P_1^{(0)}, N_1) \tag{11}$$

represents the probability that crossings of the β_1 threshold have occurred in at least M_1 of the N_1 transmissions in a common resolution cell for the no-target environment. The probability of using the second or confirmation step for the no-target case is then the probability that the above single-cell set of threshold crossing events is met in at least one of the N_F resolution cells. This probability is

$$P_{F1} = 1 - (1 - F_1^{(0)})^{N_F} \tag{12}$$

and for the usual case where $F_1^{(0)} \ll 1$, the approximation

$$P_{F1} = N_F F_1^{(0)} \tag{13}$$

can be employed. This approximation has been used in the formulation of $\overline{C}$ in Equation (10).

The optimization procedure for a given selection of the four vectors (M_1, N_1, M_T, N_2) involves finding the vector (β_1, β_2, $\overline{X}$) satisfying P_D and P_{FA} (Equations (1) and (8), respectively) and minimizing the cost $\overline{C}$. The method of Lagrange multipliers is employed for this portion of the optimization. The Lagrangian

$$L = \overline{C} - \tau P_D - \mu P_{FA} \tag{14}$$

is formed, where τ and μ are the undetermined coefficients. The partial derivatives of L with respect to the design variables (β_1, β_2, $\overline{X}$) are first formed, and are each set equal to zero;

$$\frac{\partial L}{\partial X} = \frac{\overline{C}}{\overline{X}} - \tau \frac{\partial P_D}{\partial \overline{X}} = 0, \tag{15}$$

$$\frac{\partial L}{\partial \beta_1^2} = \frac{\partial C}{\partial \beta_1^2} - \tau \frac{\partial P_D}{\partial \beta_1^2} - \mu \frac{\partial P_{FA}}{\partial \beta_1^2} = 0, \tag{16}$$

$$\frac{\partial L}{\partial \beta_2^2} = \frac{\tau \partial P_D}{\partial \beta_2^2} - \mu \frac{\partial P_{FA}}{\partial \beta_2^2} = 0, \tag{17}$$

$$P_D = P_{D_0}, P_{FA} = P_{FA_0}. \tag{18}$$

After solving for the undermined multipliers, the three equations of interest are

$$f_1 = \overline{X} \frac{\partial \overline{C}}{\partial \beta_1^2} \frac{\partial P_D}{\partial \overline{X}} \frac{\partial P_{FA}}{\partial \beta_2^2} - \overline{C} \left(\frac{\partial P_D}{\partial \beta_1^2} \frac{\partial P_{FA}}{\partial \beta_2^2} - \frac{\partial P_D}{\partial \beta_2^2} \frac{\partial P_{FA}}{\partial \beta_1^2} \right) = 0, \tag{19}$$

$$f_2 = P_D - P_{D_0} = 0, \tag{20}$$

$$f_3 = P_{FA} - P_{FA_0} = 0. \tag{21}$$

A Newton's interation procedure is then employed to find (β_1, β_2, $\overline{X}$) solving Equation (18), (19) and (20). The iteration is

$$\frac{\partial f_1^J}{\partial \overline{X}} \Delta \overline{X}^J + \frac{\partial f_1^J}{\partial \beta_1^2} \Delta \beta_1^{2J} + \frac{\partial f_1^J}{\partial \beta_2^2} \Delta \beta_2^{2J} = - f_1^J \tag{22}$$

$$\frac{\partial f_2^J}{\partial \overline{X}} \Delta \overline{X}^J + \frac{\partial f_2^J}{\partial \beta_1^2} \Delta \beta_1^{2J} + \frac{\partial f_2^J}{\partial \beta_2^2} \Delta \beta_2^{2J} = - f_2^J \tag{23}$$

$$\frac{\partial f_3^J}{\partial \beta_1^2}\Delta\beta_1^{2J} + \frac{\partial f_3^J}{\partial \beta_2^2}\Delta\beta_2^{2J} = -f_3^J \tag{24}$$

where

$$(\bar{X}^{J+1}, \beta_1^{J+1}, \beta_2^{J+1}) = (\bar{X}^J, \beta_1^J, \beta_2^J) + (\Delta\bar{X}^J, \Delta\beta_1^J, \Delta\beta_2^J). \tag{25}$$

Involved in this iteration are the first and second derivatives of

$$P = \sum_{K=M_1}^{N_1} \binom{M_1}{K} P_1^K (1-P_1)^{N_1-K} \sum_{J=M_2-K}^{N_2} \binom{N_2}{J} P_2^J (1-P_2)^{N_2-J}. \tag{26}$$

These derivatives are determined to be:

$$\frac{\partial P}{\partial P_1} = \sum_{K=M_1}^{N_1} \binom{N_1}{K} P_1^K (1-P_1)^{N_1-K} \left(\frac{K}{P_1} - \frac{N_1-K}{1-P_1}\right) \sum_{J=M_2-K}^{N_2} \binom{N_2}{J} P_2^J (1-P_2)^{N_2-J}, \tag{27}$$

$$\frac{\partial P}{\partial P_2} = \sum_{K=M_1}^{N_1} \binom{N_1}{K} P_1^K (1-P_1)^{N_1-K} \left(\frac{M_T-K}{P_2}\right) \binom{N_2}{M_T-K} P_2^{M_T-K} (1-P_2)^{N_2-M_T+K}, \tag{28}$$

$$\frac{\partial^2 P}{\partial P_1^2} = \sum_{K=M_1}^{N_1} \binom{N_1}{K} P_1^K (1-P_1)^{N_1-K} \left(\frac{K(K-1)}{P_1^2} - \frac{2K(N_1-K)}{P_1(1-P_1)} + \frac{(N_1-K)(N_1-K-1)}{(1-P_1)^2}\right) \sum_{J=M_T-K}^{N_2} \binom{N_2}{J} P_2^J (1-P_2)^{N_2-J}, \tag{29}$$

$$\frac{\partial^2 P}{\partial P_1 \partial P_2} = \sum_{K=M_1}^{N_1} \binom{N_1}{K} P_1^K (1-P_1)^{N_1-K} \left(\frac{K}{P_1} - \frac{N_1-K}{1-P_1}\right) \left(\frac{M_T-K}{P_2}\right) \binom{N_2}{M_T-K} P_2^{M_T-K} (1-P_2)^{N_2-M_T+K}, \tag{30}$$

$$\frac{\partial^2 P}{\partial P_2^2} = \sum_{K=M_1}^{N_1} \binom{N_1}{K} P_1^K (1-P_1)^{N_1-K} \left(\frac{M_T - K}{P_2} \right) \left(\frac{M_2 - K - 1}{P_2} - \frac{N_2 - M_2 + K}{1-P_2} \right) \binom{N_2}{M_T - K} P_2^{M_T-K} (1-P_2)^{N_2-M_T+K}. \tag{31}$$

The first and second partial derivatives of

$$Q = \left[1 + \frac{\beta^2 \overline{X}}{(\overline{X}+2)^2} \right] \exp \left\{ -\frac{\beta^2}{(\overline{X}+2)} \right\}$$

with respect to β^2 and $\overline{X}$ are also involved in this iteration and the equations are:

$$\frac{\partial Q}{\partial \overline{X}} = \beta^2 \exp \left\{ \frac{-\beta^2}{\overline{X}+2} \right\} \left[\frac{4}{(\overline{X}+2)^3} + \frac{\beta^2 \overline{X}}{(\overline{X}+2)^4} \right], \tag{32}$$

$$\frac{\partial Q}{\partial \beta^2} = \exp \left\{ \frac{-\beta^2}{\overline{X}+2} \right\} \left[\frac{2}{(\overline{X}+2)^2} + \frac{\beta^2 \overline{X}}{(\overline{X}+2)^3} \right], \tag{33}$$

$$\frac{\partial^2 Q}{\partial \overline{X}^2} = \exp \left\{ \frac{-\beta^2}{\overline{X}+2} \right\} \left[\frac{3\beta^4 (2-\overline{X})}{(\overline{X}+2)^5} - \frac{12\beta^2}{(\overline{X}+2)^4} + \frac{\beta^2 \overline{X}}{(\overline{X}+2)^6} \right], \tag{34}$$

$$\frac{\partial^2 Q}{\partial \overline{X} \partial \beta^2} = \exp \left\{ \frac{-\beta^2}{\overline{X}+2} \right\} \left[\frac{4}{(\overline{X}+2)^3} - \frac{2\beta^2 (2-\overline{X})}{(\overline{X}+2)^4} - \frac{\beta^4 \overline{X}}{(\overline{X}+2)^5} \right], \tag{35}$$

$$\frac{\partial^2 Q}{\partial (\beta^2)^2} = \exp \left\{ \frac{-\beta^2}{\overline{X}+2} \right\} \left[\frac{(2-\overline{X})}{(\overline{X}+2)^2} + \frac{\beta^2 \overline{X}}{(\overline{X}+2)^4} \right]. \tag{36}$$

Conclusions

A practical and efficient class of sequential-detection modes has been developed for the detection of a point target in an environment of strong localized interfering signals that have the same waveform as the transmitted signal but appear at random in the target parameter space. The sequential test, conducted at a beam position for

the presence of a target return, has a maximum of two steps and introduces a target-parameter-consistency test at each of the sequential steps employed in order to accomplish the desired rejection of the randomly occurring intense interfering signal. The newly developed modes are free of the constraint imposed by classical sequential analysis, namely, that the same 'experiment' be used at each of the sequential steps. The number of transmissions and the decision rule employed are changed at each of the sequential steps for these sequential interference-rejection modes. System cost is significantly reduced over that for a fixed-sample-size test incorporating the same discrimination criteria. The solution of the optimization problem is shown to involve the use of a relatively low-cost first sequential step that must be employed at all beam positions. The decision rule for employing the second, or confirmation, step is also shown to involve a relaxed set of criteria. The second sequential step is noted to be a relatively high-cost step. However, it is employed only approximately 6% of the time in the no-target environment. This confirmation step also involves the use of a more stringent set of criteria for accepting the target-present hypothesis, so that the specified final set of error probabilities are achieved in spite of the presence of the strong localized interfering signal environment.

RESPONSE OF LOW-POWER NUVISTORS TO PULSED NUCLEAR RADIATION*

By

I. F. Stacy and F. J. Feyder

RCA Electronic Components and Devices Division
Somerville, N. J.

Summary—This paper discusses the results of the exposure of operating nuvistors to the gamma-neutron fields of the pulsed TRIGA Mark F reactor at the Diamond Ordnance Radiation Facility. Three nuvistor types and a conventional miniature tube type were operated statically and dynamically (at 1,000 cycles per second). Grid and plate currents were recorded before, during, and after the reactor transients. The tests showed that there were no permanent effects on the tubes. During the pulses, an electron current flowing through the grid resistor to the grid caused a decrease in bias and a corresponding increase in plate current. During dynamic operation and with the signal-input coupling capacitor in the circuit, the plate-current recovery time could be made as small as desired. During static operation the plate-current shift followed the reactor transient. As distance from the reactor shroud was increased, the current induced in the grid circuit by the transient corresponded more closely to the fall-off in the peak gamma exposure rate than to the peak neutron flux rate. The results of the tests were consistent with the theory of Compton ejection of electrons from the tube grid.

The data indicate that the magnitude of the effect on a tube cannot be correlated with the grid weight or surface area alone, but must include the over-all tube structure and potential distribution.

Introduction

FOR CERTAIN instrumentation problems that arise in a very high-intensity radiation environment, low-power nuvistors provide an acceptable compromise between semiconductors, which are susceptible to neutron flux, and conventional-size vacuum tubes, which have higher power requirements.[1] Specifically, this paper discusses the radiation response of the low-power nuvistors. These tubes are effective because, frequently, only an impedance match to lower impedance lines is required without much power-handling capability.

In previous tests, nuvistor audio amplifiers showed no frequency change during transient radiation bursts, and no permanent damage

* The work reported here was sponsored by the Harry Diamond Laboratories, U. S. Army Materiel Command under contract number DA-49-186-AMC-89(D).

[1] P. A. Trimmer, "Transient Radiation Effects on Basic Triode Amplifiers," Harry Diamond Laboratories Report TR-1197, 24 April 1964.

from either steady-state exposure or from repeated transient bursts.[2-4] The purpose of this study was threefold:

(a) To confirm the hypothesis that the Compton ejection of electrons from the grid structure is the cause of grid current in low-power nuvistors, as was previously shown for conventional tubes.

(b) To determine the relationship between grid structure (mass and type of material) and the induced current.

(c) To select a tube suitable for future applications in high-intensity radiation environments.

The following experiments involved various types of nuvistors and a conventional vacuum tube that were exposed to nuclear radiation at the Diamond Ordinance Radiation Facility (DORF). These investigations were made to ascertain the radiation effects on the static and dynamic characteristics of the tube types and to compare the radiation effects on each type.

Description of the Tubes

Nuvistor tubes utilize a lightweight cantilever-supported cylindrical electrode structure, including a heater–cathode assembly, housed in a ceramic–metal envelope. All connections are brazed at very high temperatures to eliminate structural strain and element distortion; the brazing is done in a hydrogen atmosphere to reduce oxide formation. The tubes are exhausted and sealed without a getter at high temperatures to reduce the gas and impurity contents.

The basic nuvistor tested was type 7586, a single-ended, medium-mu, general-purpose triode that requires 0.85 watt of heater power. The structure of type 7586 and the grid geometry are shown in Figure 1.

Type A15274 is a developmental half-size, double-ended, sharp-cutoff, rf-amplifier nuvistor triode that requires 0.43 watt of input heater power. Its structure and grid geometry are shown in Figure 2.

Type A15475 is a developmental half-size, double-ended, oscillator-amplifier nuvistor triode that requires 0.16 watt of input heater power. Its structure and grid geometry are shown in Figure 3.

---

[2] R. G. Saelens, "Transient Nuclear Radiation Effects on Electron Tubes and Transistors," U. S. Army Research Office (Durham), Report No. ARODR62-2, p. 225.

[3] H. A. Stern et al, "Radiation-Induced Gas Effects on Electron Tube Materials," RCA, Lancaster, Pennsylvania, Final Progress Report, Contract No. DA36-039-SC-89121, 1 July 1961 to 30 June 1962, p. 81.

[4] F. J. Feyder, "Nuvistor Nuclear Radiation Testing," RCA, Harrison, N. J., Publication ST-2296, August 1962.

Type 6J4WA, a conventional glass, seven-pin minature, high-mu triode with separate heater and cathode assembly has approximately the same transconductance as type 7586. The 6J4WA is made with either a wound grid or a frame grid. Its structure is shown in Figure 4; the two grid structures are shown in Figure 5.

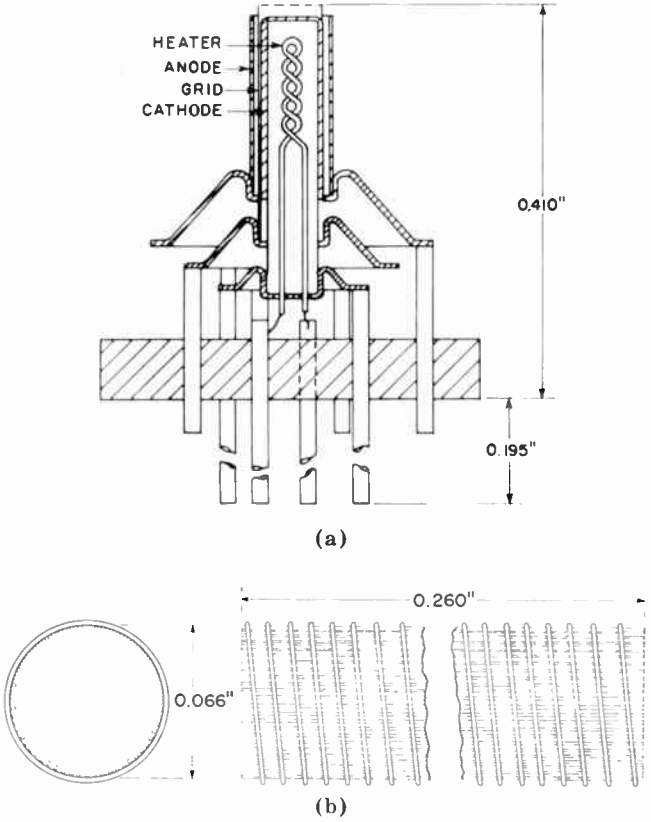

Fig. 1—Structure of the 7586 nuvistor triode, and detail of grid structure.

The physical sizes of the tube types exposed in the reactor are compared in Figure 6.

Test Procedure

The nuvistors were mounted in 6061-6T aluminum cans, and were potted with sockets and associated components in Sylgard 184 resin to prevent air ionization. The potting container was evacuated to elim-

inate air bubbles from the resin that might "bridge" some of the conductors.

Instrumentation consisted of a control panel located at the side of the reactor pool and containing bias controls, grid resistors, plate-load resistors, plate-and-grid-circuit sampling resistors, coupling capacitors,

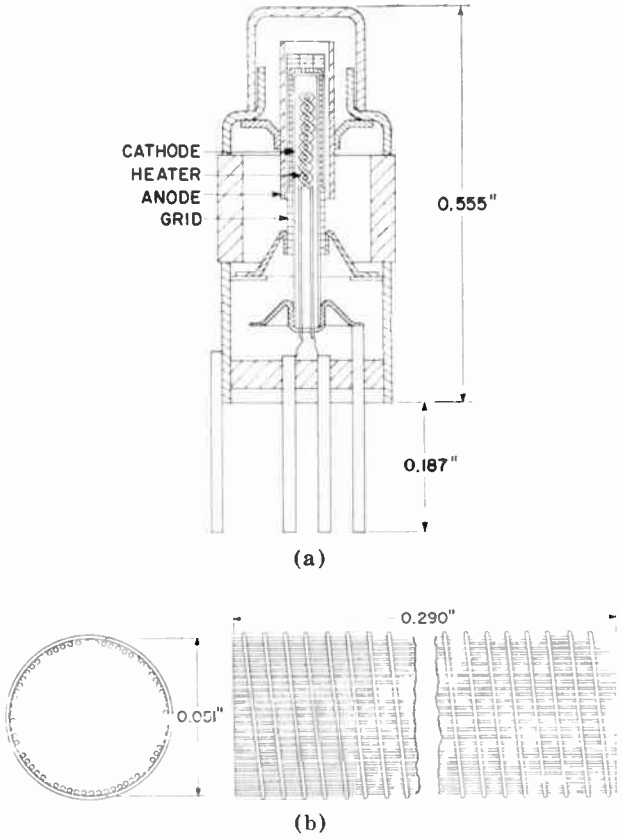

Fig. 2—Structure of type A15274 nuvistor triode and detail of grid structure.

and connectors from the aluminum test container to the power supplies and the measuring circuits. All connections to the tubes under test in the aluminum containers were made through RG59U coaxial cables.

The TRIGA Mark F nuclear reactor, which was used for the tests, is of the swimming-pool type. Materials can be irradiated in any one of three areas—in an exposure room adjacent to the reactor, in the

reactor core, or in the pool. For these experiments, the nuvistors were exposed in the pool. The reactor uses uranium–zirconium-hydride fuel-moderator material; it is water-cooled, and produces transient emissions that have a duration of approximately 13 milliseconds at half-maximum pulse height and an integrated energy of up to 23 megawatt-

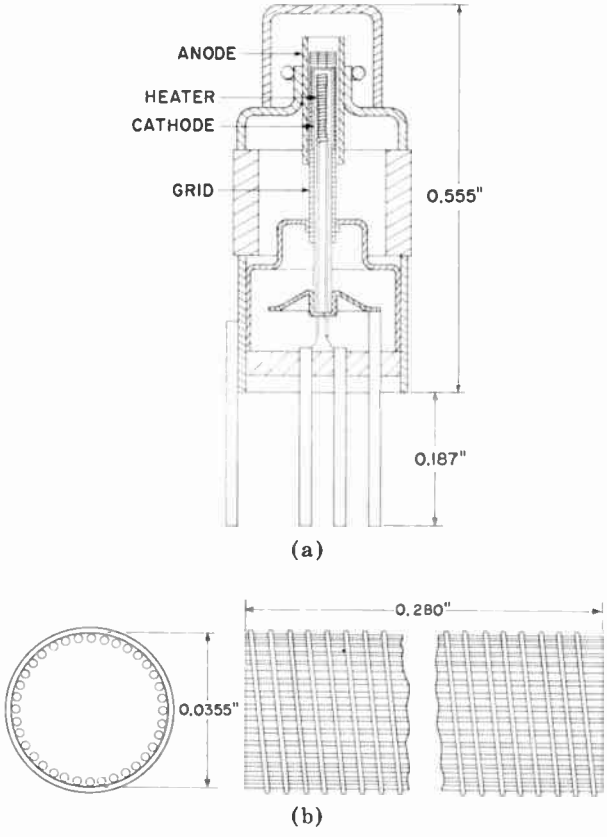

Fig. 3—Structure of type A15475 1/4-watt nuvistor triode and detail of grid structure.

seconds. All reactor pulses in this experiment involved peak powers between 1100 and 1180 megawatts. The total integrated energies ranged from 19.5 to 20.4 megawatt-seconds. Because of these small ranges, the different radiation-pulse measurements are comparable.

Dosimetry was supplied by the Diamond Ordinance Radiation Facility. Sulfur pellets were used to measure the fast neutron fluence, and

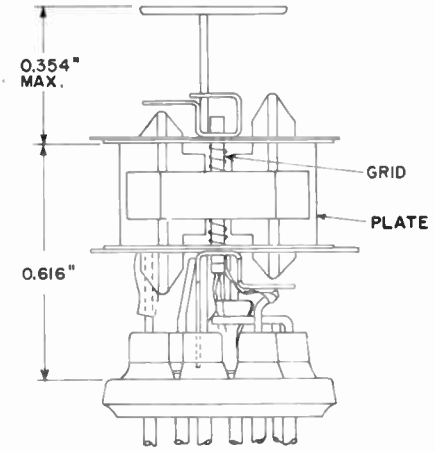

Fig. 4—Structure of type 6J4WA miniature triode.

cobalt-glass rods were used for gamma and slow neutron exposures. A sulfur pellet and a cobalt-glass rod assembly were placed in a depression in a Sylgard 184 disc at the thin end of a container to duplicate the positions of the tubes under test. The gamma-exposure rate varied from 1×10^7 gamma/sec at zero inches from the reactor shroud to 1×10^5 gamma/sec at 24 inches, a change of one order of magnitude in 12 inches. The fast-neutron exposure rate varied from 5×10^{15} neutrons/cm^2-sec at zero inches to 5×10^{13} neutrons/cm^2-sec at 10 inches, a change of one order of magnitude in 5 inches.

In these experiments, the electron tubes to be tested were selected from identified production to ensure uniformity of characteristics, and were stabilized. After the tubes were mounted on the container covers, their static and dynamic characteristics were checked before and after potting. Spurious oscillation, which was detected, was stopped by the addition of a 0.001-microfarad mica capacitor mounted on the expo-

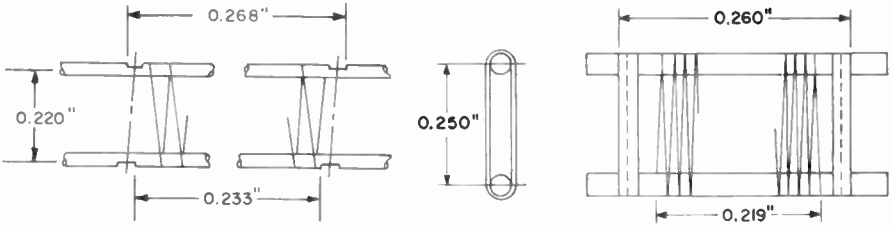

Fig. 5—(a) Wound-grid and (b) frame-grid structures used with type 6J4WA miniature triode.

sure head between plate and ground. The effect of radiation on the mica capacitor was insignificant.[5]

Type 7586 was operated at a plate current of 10 milliamperes; static plate current was read before and after each transient radiation burst to determine if the circuits were functioning and whether any permanent damage had resulted. No permanent damage was apparent after as many as 16 reactor pulses. After the last transient burst, the

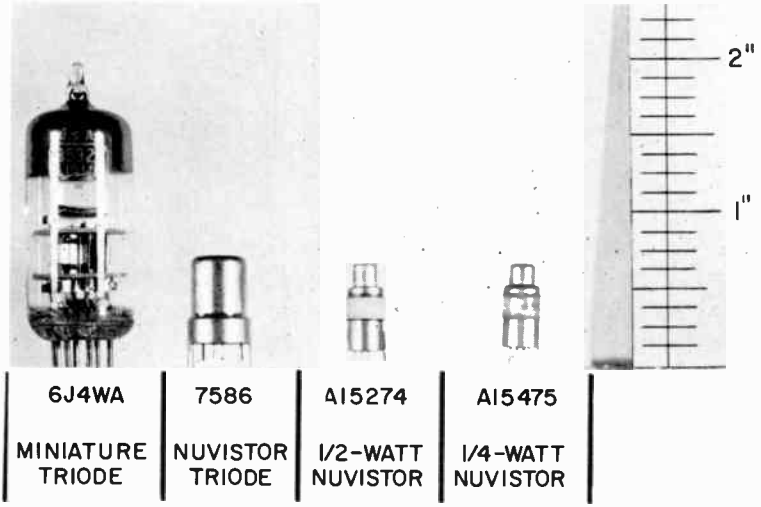

Fig. 6—Comparison of sizes of tubes used in radiation experiments.

static plate currents were within an average of 1.6% of the initial values. All dynamic tests were run at a grid-signal frequency of 1000 cycles per second, allowing the recording of individual cycles.

Test Results — Standard Tube Types

Socket-Leakage Measurements

One of the exposure heads contained three nuvistors and two empty sockets, one of which was composed of mica-filled phenolic resin and the other of diallyl phthalate. Cable conductors were soldered to the cathode and grid pins on both empty sockets. The current flowing across the sockets during the reactor pulses was determined by meas-

[5] D. C. Jones, editor, "Transient Radiation Effects on Electronics (TREE) Handbook," Battelle Memorial Institute, DASA 1420, February 20, 1964, pp. G1-G13.

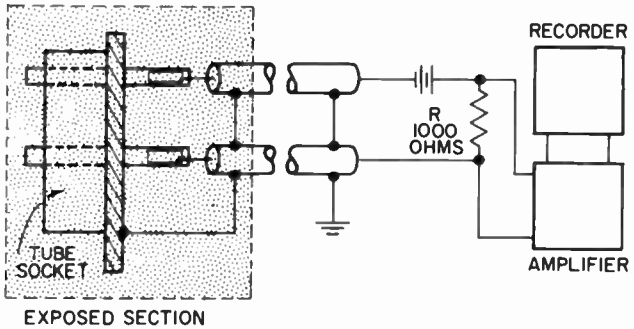

Fig. 7—Circuit for measuring socket leakage.

urement of the voltage generated across a 1000-ohm resistor in series with the two socket pins. The circuit is shown in Figure 7; the results obtained with an applied voltage of —100, 0, and 100 volts are given in Figure 8.

Because the slopes of the leakage curves for the two socket materials are approximately the same, either the ohmic resistance of both socket materials was approximately the same or the leakage in the potting material was being measured. However, the diallyl phthalate

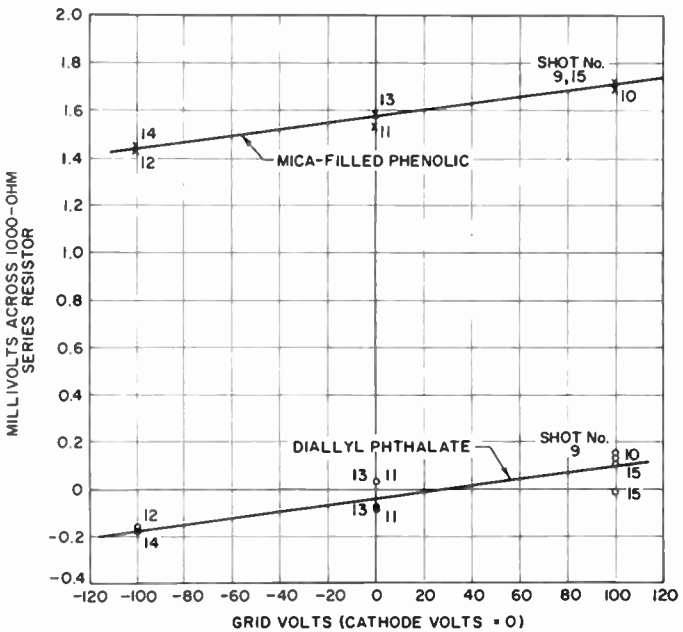

Fig. 8—Results of socket-leakage tests.

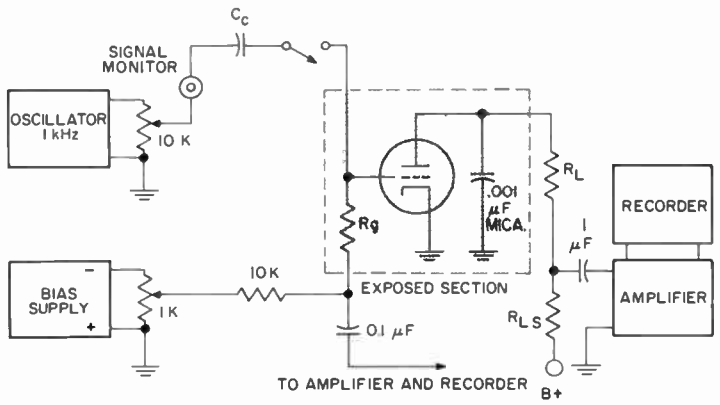

Fig. 9—Circuit for measuring fixed-bias dynamic operation.

line passes near the origin, and the mica-filled phenolic line shows a 1.6-microampere current superimposed on the leakage. This current is probably the result of electron emission from the mica-filled phenolic socket material.

Bias Mode

Fixed-bias operation (Figure 9) consistently showed a smaller transient increase in plate current than did the cathode-bias operation (Figure 10). This result was unexpected because of the self-regulating feature of cathode-bias operation.

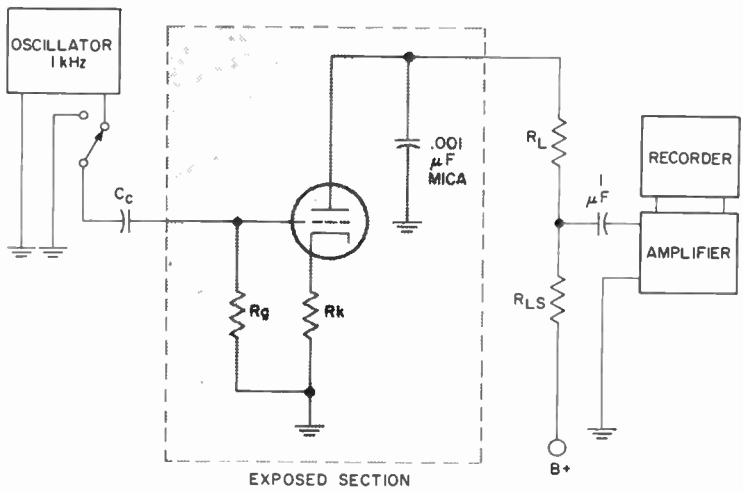

Fig. 10—Circuit for measuring cathode bias.

Plate-Load Resistor

Although the plate-current change varied by a factor of more than 7 in response to a change in the plate-load resistor, the corresponding bias changes were relatively small. These relationships show that the change in circuit gain was caused only by the change of plate-load resistor. It was not caused by any change in the nuvistor.

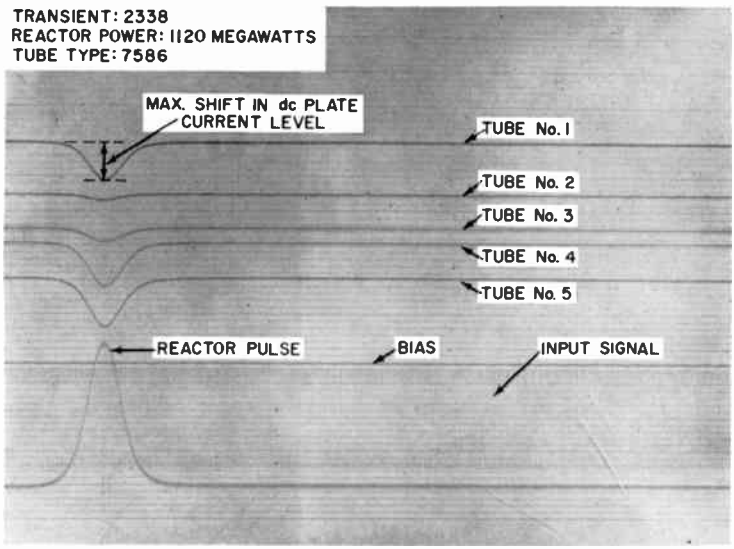

Fig. 11—Effects of nuclear transient on static operation.

Static Versus Dynamic Operation

For a given set of conditions, the data showed a much larger shift in d-c plate-current level under static operation than in the dynamic state (see Figures 11 and 12). In static operation, the input-signal switch was open, so that the grid current generated by the reactor pulse had to pass through only the grid resistor. With the switch closed for dynamic operation, the signal generator provided a lower-impedance parallel path for the grid current. Therefore, under dynamic operation, there was a smaller change in bias during the pulse and a resultant smaller change in plate current.

Gain Increase

In dynamic operation, the amplitude of the 1000-hertz output signal temporarily increased during the reactor pulse. This increment is consistent with an increase in the amplification factor of the tube caused by a decrease in bias with a subsequent rise in circuit gain.

grid by *gamma* radiation, and thereby cause a current flow through the grid resistor with a resultant change in bias.

Recovery Time

The d-c outputs, with the input circuit open, followed the radiation pulse closely, as shown in Figure 11. Figure 12 shows the extended recovery time, under dynamic operation, caused by a long *RC* time con-

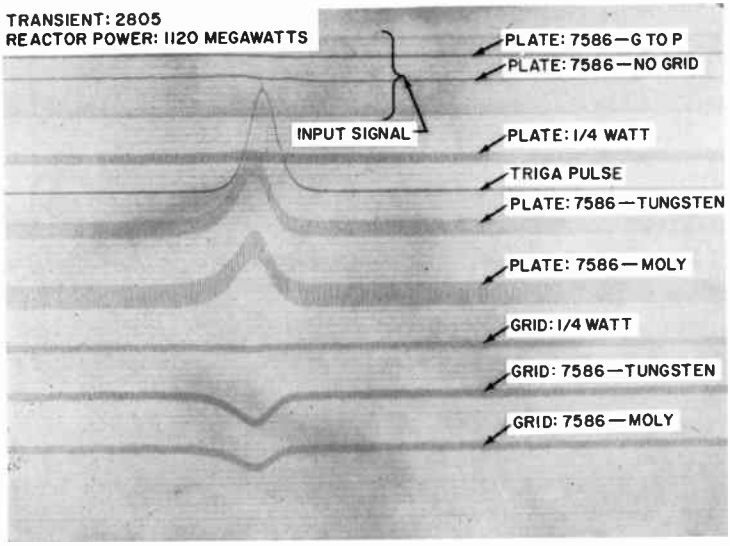

Fig. 14—Effects of nuclear transient on dynamic operation (short *RC*).

stant in the input circuit. A comparison of Figures 12 and 14 shows the difference in recovery time for input-circuit time constants of 100 and 4.7 milliseconds.

Effect of Variations In Materials and Construction

Modified type 7586 was tested under diode conditions (a) without a grid, and (b) with the grid tied to the plate. In both instances, the effects of the transients were the same as those on tubes without active grids, or the same as those on the cables alone (see Figure 14). This information is consistent with the conclusion that the measured plate-current changes are cause by the grid effects.

Table II shows the grid currents induced in the tubes by the gamma exposure rates. Also tabulated are relative induced currents (6J4WA = 1.0) that compare the different materials and constructions under

equal gamma-exposure rates and operating conditions. The relative induced currents are grouped in brackets, but the numbers within each bracket are not significantly different. Therefore, the tube variations within each group could show similar responses to the radiation.

Type 7586 with a tungsten grid showed a significantly greater grid current than did the nuvistor with the standard molybdenum grid. Although type 7586 with three grid flanges has almost three times the grid-structure weight of the standard 7586 with one flange, the grid

Table II—Grid Currents Induced by the Reactor Transients

Tube Type	Generated Grid Current (10^{-13} amp-sec-r^{-1})	Relative Grid Current (6J4WA = 1.0)	Total Control-Grid-Structure Weight (mg)	Control Grid Active Weight (mg)
6J4WA-Wound	17.0	1.0	98	98
6J4WA-Frame	16.9	1.0	216	216
7586-Grid to Shell	4.7	0.28	1138	2.90
7586-Tungsten	3.3	0.19	30	4.49
1/2-Watt	3.0	0.17	263	2.30
7586-Molybdenum	2.2	0.13	29	2.90
7586-Three Flanges	1.9	0.11	81	2.90
1/4-Watt	1.1	0.07	287	1.20

current was approximately the same. This result indicates that the mass of the complete grid structure is not the sole determinant of the induced grid current during irradiation, but that other factors are involved, e.g., the mass of the active grid or the projected area of the grid structure.

Type 7586 was tested with the grid tied to the shell and showed a larger grid current than did the standard 7586, although the result was not in proportion to the grid structure weights. Electrons from the outside of the shell probably return to the shell and do not contribute to the net grid current.

In still another test involving the standard 7586, the plate voltage was turned off. The induced grid current was less than with the plate voltage applied. This result further substantiates the theory that if the freed electrons are not collected by a positive electrode, some of them will return to the grid.

The two 6J4WA grid constructions differ in grid weights by more than a factor of two. However, the radiation effects on the two tubes were approximately the same. This result, therefore, reconfirms that

the weight of the grid alone is not the determining factor. The grid surface area, the projected area intercepted by the gamma radiation, or a combination of these and the grid mass, probably contribute to the radiation effect.

The ½-watt nuvistor (A15274), which has a tungsten grid, displayed approximately the same effect as type 7586 with a tungsten grid. The ½-watt nuvistor grid is electrically connected to the metal shell, with a corresponding increase in weight and surface area, but the radiation effect is more closely related to the active grid weight than to the total grid-structure weight.

The ¼-watt nuvistor (A15475) with a tungsten grid, which requires less than one quarter the heater power of type 7586, showed 50% of the radiation effect on type 7586 with the molybdenum grid; it showed less than 10% of the radiation effect on type 6J4WA. These relationships are true despite the fact that the ¼-watt nuvistor grid is electrically connected to the metal skirt on the envelope. This design makes its total grid-structure weight equal to that of the 6J4WA frame grid.

The Compton coefficient can be used to calculate an approximate induced grid current for the 7586. The formula for Compton electrons set in motion by incident photons is[6]

$$\frac{\text{photons}}{\text{cm}^2} \times \frac{\text{electrons}}{\text{gram}} \times \frac{\text{cm}^2}{\text{photons-electrons-MeV}} \times$$

$$\text{electron energy range (MeV)} = \frac{\text{electrons set in motion}}{\text{gram}}.$$

A gamma-ray energy of 1.0 MeV (the average gamma energy from the DORF) corresponds to 1.8×10^9 photons/cm²-roentgen, calculated from the true absorption coefficients for air.* The figures for electrons/gram for molybdenum and tungsten are 2.6×10^{23} and 2.4×10^{23}, respectively. We shall use a mean value. The total Compton coefficient for electrons with energies up to 0.796 MeV is 2.2×10^{-25} cm²/electron-MeV. Substituting these values in the above formula:

$$(1.8 \times 10^9)\ (2.5 \times 10^{23})\ (2.2 \times 10^{-25})\ 0.796 = 7.9 \times 10^7$$
electrons/gram-roentgen.

[6] G. J. Hine and G. L. Brownell, *Radiation Dosimetry*, Academic Press Inc., 1956, p. 67.

* See Reference (6), p. 87.

For a 30-milligram grid structure, this is equivalent to 3.8×10^{-13} ampere-second/roentgen, an order-of-magnitude check of the results for the 7586 in Table II. This result is also close to the results of calculations for a similar nuvistor type given in Reference (7).

Conclusions

The grid currents measured directly were valid. They correlated with the grid-current changes calculated from the plate-current changes. The measured grid currents were independent of the grid resistance. In the calculation of the grid-current changes, it was necessary to use the actual circuit gain during the transient radiation. With increased grid resistance, the change in the tube amplification factor was appreciable.

Much greater radiation effects were indicated for the miniature 6J4WA than for any of the nuvistors. The induced grid current in the standard molybdenum-grid 7586 was 33% less than that in the tungsten-grid version, and approximately 13% of that in 6J4WA miniature tube. The ½-watt nuvistor showed approximately the same radiation effects as did the tungsten-grid 7586. The ¼-watt nuvistor showed a lesser radiation effect than did any of the standard nuvistors. The effect was less than 10% of that for the 6J4WA.

The recovery time for the radiation effects measured was a function of the input-circuit time constant. The recovery time could be decreased, as desired, by proper choice of the grid resistance and coupling capacitor.

The variation of induced grid current with the distance from the reactor shroud agrees with the variation of the gamma-exposure rate with distance. The grid current was caused by the Compton ejection of electrons from the grid structure by gamma radiation.

The radiation effects did not correlate with grid weight, with grid surface area, or with potential distribution alone. All of these factors were probably involved.

The following conclusions were reached in regard to the design of radiation-hardened circuits:

1. The tube structure determines the induced grid current at a particular radiation level. To minimize the effect of this grid current, the grid resistance should be as small as possible and consistent with good circuit-design techniques.

[7] W. D. Parker, A. G. Berger, and J. P. Gleason, "Transient Radiation Instrumentation Equipment Study," U.S. Air Force Contract No. AF04 (695)-677, Report No. NVR-3880, June 1965, Appendix A.

2. The *RC* time-constant of the grid input circuit should be kept as small as possible to minimize the recovery time.

3. Molybdenum-grid tubes are preferable to tungsten-grid tubes.

4. Low plate voltage results in a smaller induced grid current.

5. The ¼-watt nuvistor was the best of the standard nuvistors tested, and was an order of magnitude better than the 6J4WA miniature tube.

ACKNOWLEDGEMENT

The authors wish to thank P. A. Trimmer of the Harry Diamond Laboratories for several helpful discussions, and B. MacPherson of RCA Electronic Components and Devices, for the construction of the electronic circuits.

ANALYSIS OF MULTIPLE-SIGNAL FM DETECTION SYSTEM

By

T. Murakami

RCA Missile and Surface Radar Division
Moorestown, N. J.

Summary—In a command and control system it is sometimes necessary to process a multiplicity of signals with a single receiver. This paper treats one method of implementing such a system and establishes the signal-to-noise performance and dynamic range capability. Analysis is made of square-law detection of multiple FM signals in the presence of noise for a system using a non-limiting i-f amplifier. The system model consists of two linear-slope filters of opposite sign each followed by square-law devices whose outputs are subtracted to obtain the discriminator output. The important theoretical performance characteristics of the multiple-signal FM detection system have been determined as an aid in the design of a practical system. Equations for the output signal-to-noise ratio have been derived as functions of the various system parameters, such as i-f bandwidth, frequency deviation, signal frequency, and audio filter bandwidth. The single-signal and multiple-signal signal-to-noise ratios are shown as functions of the input carrier-to-noise ratio. These illustrate the signal suppression effect of the detection system and indicate the usable dynamic range of the given system. Effects of non-ideal filters and carrier offset on the system performance are also shown.

Introduction

A THEORETICAL analysis is made of an FM detection system that uses a square-law device instead of a linear demodulator and a non-limiting i-f amplifier. This type of system is chosen so as to obtain minimum signal suppression in the simultaneous reception of multiple signals. The carriers in this system are frequency modulated by cw tones, these audio tones being chosen such that minimum interaction is produced in the detection process. Small offsets from the system center frequency are used for the different carriers for the same reason. The main reason for the choice of such a system is its suitability for telemetry with a number of simultaneously airborne vehicles.

The output signal-to-noise ratio is found for the case of a single signal and noise, and then the results are extended to the case of multiple signals. In this analysis, the effects of carrier detuning and relative carrier amplitudes are considered. The system model used

is shown in Figure 1. Linear-slope filters and sharp-cutoff band pass in the i-f and audio filters are assumed. It is also assumed that the pass-band amplitude ripple does not significantly affect the noise autocorrelation function, so that a rectangular pass band can be assumed for noise. The band-passed signal and noise components are passed through the slope circuits, which superimpose AM on the original FM signal and add a derivative component to the noise. This composite waveform is applied to the respective square-law devices, and the outputs are subtracted as shown and then filtered at the audio

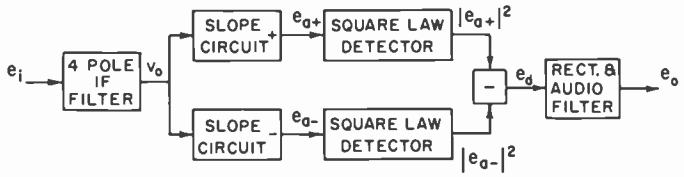

Fig. 1—Model of detection system.

signal frequency. The output power spectrum prior to filtering is found from the Fourier transform of the autocorrelation function of the voltage out of the subtraction circuit. After audio filtering, the output signal-to-noise is determined from the pertinent components in the power spectrum.

Passage of FM Wave through Filter

Consider an FM wave passing through a filter with a voltage transfer function $T(\omega)e^{j\theta(\omega)}$, as shown in Figure 2. Let the input voltage be

$$v_i = E_s \cos(\omega_c t + \beta \sin \omega_s t),$$

where

E_s = signal carrier amplitude,

ω_c = carrier angular frequency,

β = modulation index = $\Delta\omega/\omega_s$,

$\Delta\omega$ = angular deviation,

ω_s = angular frequency of modulation.

v_i can be written in terms of a Bessel function expansion as

$$v_i = E_s \sum_{n=-\infty}^{\infty} J_n(\beta) \cos(\omega_c + n\omega_s)t. \qquad (2)$$

After passing through the filter, the FM wave is

$$v_o = \mathrm{Re}\,\{E_s \sum_{n=-\infty}^{\infty} J_n(\beta)\, T(\omega_c + n\omega_s)\} \exp\{j[(\omega_c + n\omega_s)t + \theta(\omega_c + n\omega_s)]\}$$

$$= \mathrm{Re}\,\{E_s \exp\{j[\omega_c t + \theta(\omega_c)]\}\} \sum_{n=-\infty}^{\infty} J_n(\beta)\, T(\omega_c + n\omega_s) \exp\{j(n\omega_s t + \theta_n)\}, \tag{3}$$

where

$$\theta_n = \theta(\omega_c + n\omega_s) - \theta(\omega_c).$$

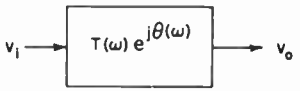

Fig. 2—Filter transfer function.

The complex envelope E is then

$$E = E_s \sum_{n=-\infty}^{\infty} J_n(\beta)\, T(\omega_c + n\omega_s) \exp\{j(n\omega_s t + \theta_n)\}$$

$$= E_s \sum_{n=-\infty}^{\infty} J_n(\beta)\; T\;(\omega_c + n\omega_s)\; [\cos\;(n\omega_s t + \theta_n) + j \sin\;(n\omega_s t + \theta_n)] \tag{4}$$

If we define the quantities

$$u = E_s \sum_{n=-\infty}^{\infty} J_n(\beta)\, T(\omega_c + n\omega_s) \cos\;(n\omega_s t + \theta_n),$$

$$v = E_s \sum_{n=-\infty}^{\infty} J_n(\beta)\, T(\omega_c + n\omega_s) \sin\;(n\omega_s t + \theta_n),$$

the complex envelope of a zero frequency carrier[1] can be written

$$E = u + jv. \tag{5}$$

[1] H. A. Wheeler, "The Solution of Unsymmetrical-Sideband Problems with the Aid of the Zero Frequency Carrier," *Proc. IRE*, Vol. 29, p. 446; Aug. 1941.

Slope-Circuit Output for Signal

To simplify the analysis, a linear slope is assumed in the discriminator circuit shown in Figure 1. With this assumption, the transfer function can be represented by the equation[2]

$$T_{\pm}(\omega) = \frac{1}{2}(1 \pm k\omega), \tag{6}$$

where k is the slope factor. For convenience, Equation (6) can also be expressed in the form of a time operator

$$T_{\pm}(p) = \frac{1}{2}(1 \mp jkp), \tag{7}$$

where p is the differential operator d/dt, so that for an input time function $e_i(t)$, the output can be written in the form

$$e_{a\pm} = T_{\pm}(d/dt)\ e_i(t). \tag{8}$$

Equation (8) gives the output of the appropriate slope circuit of Figure 1 when the proper sign is used.

The response of the signal given by Equation (5) to the slope circuit is

$$(e_{a\pm})_s = \frac{1}{2}[u(t) \pm k\dot{v}(t) + jv(t) \mp jk\dot{u}(t)]. \tag{9}$$

Slope-Circuit Output for Noise

For a zero-frequency carrier, the noise can be expressed

$$n(t) = x(t) + jy(t), \tag{10}$$

where $x(t)$ = in-phase component of the noise envelope,

$y(t)$ = quadrature component of the noise envelope.

The slope-circuit response to noise is then

$$(e_{a\pm})_n = \frac{1}{2}[x(t) \pm k\dot{y}(t) + jy(t) \pm jk\dot{x}(t)]. \tag{11}$$

---

[2] H. A. Wheeler, "Common-Channel Interference Between Two Frequency-Modulated Signals", *Proc. IRE*, Vol. 30, p. 34, Jan. 1942.

Output of Square-Law Detector

The square-law detector performs the operation

$$|e_{a\pm}|^2 = |(e_{a\pm})_s + (e_{a\pm})_n|^2, \tag{12}$$

where $(e_{a\pm})_s$ and $(e_{a\pm})_n$ are the slope circuit outputs given by Equations (9) and (11). Substitution of these values into Equation (12) results in

$$|e_{a\pm}|^2 = \frac{1}{4}|u \pm k\dot{v} + x \pm k\dot{y} + j|v \mp k\dot{u} + y \pm k\dot{x}]|^2$$

$$= \frac{1}{4}[(u \pm k\dot{v})^2 + 2(u \pm k\dot{v})(x \pm k\dot{y}) + (x \pm k\dot{y})^2$$

$$+ (v \mp k\dot{u})^2 + 2(v \mp k\dot{u})(y \mp k\dot{x}) + (y \mp k\dot{x})^2]. \tag{13}$$

Considering only the $\pm$ terms, since the others will cancel on subtraction,

$$\{|e_{a\pm}|^2\} = \frac{1}{4}\Big[\pm 2ku\dot{v} \pm 2k\dot{v}x \pm 2ku\dot{y} \pm kx\dot{y}$$

$$\mp 2kv\dot{u} \mp 2k\dot{u}y \mp 2kv\dot{x} \mp 2k\dot{x}y\Big]. \tag{14}$$

Discriminator Output

Using the plus and minus signs for the detector outputs corresponding to the two slope circuits, the discriminator output e_d can be expressed

$$e_d = |e_{a+}|^2 - |e_{a-}|^2. \tag{15}$$

For the case of one signal and noise this becomes

$$e_d = ku\dot{v} + k\dot{v}x + ku\dot{y} + kx\dot{y} - kv\dot{u} - k\dot{u}y - kv\dot{x} - k\dot{x}y. \tag{16}$$

Dividing both sides of Equation (16) by the slope factor k gives the normalized output e.

$$e = \frac{e_d}{k} = u\dot{v} + \dot{v}x + u\dot{y} + x\dot{y} - v\dot{u} - \dot{u}y - v\dot{x} - \dot{x}y. \tag{17}$$

Autocorrelation Function

To determine the spectrum of the output voltage, the autocorrelation function is found and its Fourier transform taken. The normalized autocorrelation function of the discrimination output is given by

$$R(\tau) = < e(t)\ e(t+\tau) >, \tag{18}$$

where $< >$ designates the expected value. Using Equation (17) in Equation (18), the autocorrelation function is expressed as

$$\begin{aligned} R(\tau) = &<u\ u'\ \dot{v}\ \dot{v}'> + <\dot{v}\ \dot{v}'\ x\ x'> + <u\ u'\ \dot{y}\ \dot{y}'> \\ &+ <x\ x'\ \dot{y}\ \dot{y}'> + <v\ v'\ \dot{u}\ \dot{u}'> + <\dot{u}\ \dot{u}'\ y\ y'> \\ &+ <\dot{x}\ \dot{x}'\ v\ v'> + <\dot{x}\ \dot{x}'\ y\ y'> - <\dot{x}\ x'\ y\ \dot{y}'> \\ &- <x\ \dot{x}'\ \dot{y}\ y'>, \end{aligned} \tag{19}$$

where the primes denote the functions that are displaced in time by τ.

Noise-Cross-Noise Terms

The noise-cross-noise terms in Equation (19) are

$$\begin{aligned} R_{n\times n}(\tau) = &<x\ x'\ \dot{y}\ \dot{y}'> + <\dot{x}\ \dot{x}'\ y\ y'> \\ &- <x\ \dot{x}'\ \dot{y}\ y'> - <\dot{x}\ x'\ y\ \dot{y}'>. \end{aligned} \tag{20}$$

Since x and y are independent random variables, Equation (20) can be expressed

$$\begin{aligned} R_{n\times n}(\tau) = &<x\ x'> <\dot{y}\ \dot{y}'> + <\dot{x}\ \dot{x}'> <y\ y'> \\ &- <x\ \dot{x}'> <\dot{y}\ y'> - <\dot{x}\ x'> <y\ \dot{y}'>. \end{aligned} \tag{21}$$

We define the averages[3]

$$<x\ x'> = <y\ y'> = \rho(\tau)\ \sigma^2 B, \tag{22}$$

$$<\dot{x}\ \dot{x}'> = <\dot{y}\ \dot{y}'> = -\sigma^2 B \frac{d^2\rho}{d\tau^2} = -\sigma^2 \ddot{\rho}(\tau)\ B, \tag{23}$$

$$<x\ \dot{x}'> = <y\ \dot{y}'> = -<\dot{x}\ x'> = -<\dot{y}\ y'> = \sigma^2 \dot{\rho}(\tau)\ B, \tag{24}$$

---

[3] S. O. Rice, "Mathematical Analysis of Random Noise", *Bell Syst. Tech. Jour.*, Vol. 24, p. 46, Jan. 1945.

where $\rho(\tau)$ is the normalized autocorrelation coefficient, σ^2 the noise power density, and B the i-f bandwidth of the system. Using these relations, the autocorrelation function for the noise-cross-noise component becomes

$$R_{n\times n}(\tau) = -2\,\sigma^4 B^2\,[\rho(\tau)\,\ddot{\rho}(\tau) - \dot{\rho}^2(\tau)]. \tag{25}$$

Signal-Cross-Signal and Signal-Cross-Noise Terms

The signal-cross-signal and noise-cross-signal terms can be evaluated by considering the series expansions

$$u = E_s \sum_{n=-\infty}^{\infty} J_n(\beta)\; T(\omega_c + n\omega_s) \cos\,(n\omega_s t + \theta_n), \tag{26}$$

$$\dot{u} = -E_s \sum_{n=-\infty}^{\infty} J_n(\beta)\; T(\omega_c + n\omega_s)\; (n\omega_s) \sin\,(n\omega_s t + \theta_n), \tag{27}$$

$$v = E_s \sum_{n=-\infty}^{\infty} J_n(\beta)\; T(\omega_c + n\omega_s) \sin\,(n\omega_s t + \theta_n), \tag{28}$$

$$\dot{v} = E_s \sum_{n=-\infty}^{\infty} J_n(\beta)\; T(\omega_c + n\omega_s)\; (n\omega_s) \cos\,(n\omega_s t + \theta_n). \tag{29}$$

The signal-cross-signal terms will result in the signal and its harmonic components. These components can be found by a harmonic analysis of the input signal to the detectors and then taking the fundamental component for the desired signal (ω_s). The noise-cross-signal terms are

$$\langle \dot{v}\,\dot{v}'\,x\,x'\rangle = \langle \dot{u}\,\dot{u}'\,y\,y'\rangle = \sigma^2 B\,\rho(\tau)\;\; \langle \dot{v}\,\dot{v}'\rangle$$

$$= \frac{1}{2}\,\sigma^2 B\,\rho(\tau)\; E^2_s \sum_{n=-\infty}^{\infty} J^2_n(\beta)\; T^2\,(\omega_c + n\omega_s)\; (n\omega_s)^2 \cos n\omega_s\tau, \tag{30}$$

$$\langle u\,u'\,\dot{y}\,\dot{y}'\rangle = \langle v\,v'\,\dot{x}\,\dot{x}'\rangle = -\sigma^2 B\,\rho(\tau)\,\langle u\,u'\rangle$$

$$= -\frac{1}{2}\,\sigma^2 B\,E^2_s\,\ddot{\rho}(\tau) \sum_{n=-\infty}^{\infty} J^2_n(\beta)\; T^2\,(\omega_c + n\omega_s) \cos n\omega_s\tau. \tag{31}$$

Considering only the signal-cross-noise terms, the autocorrelation function becomes

$$R_{s\times n}(\tau) = \sigma^2 BE^2 \rho(\tau) \sum_{n=-\infty}^{\infty} J^2_n(\beta)\ T^2\ (\omega_c + n\omega_s)\ (n\omega_s)^2 \cos n\omega_s\tau$$

$$- \sigma^2 B E^2_s \ddot{\rho}(\tau) \sum_{n=-\infty}^{\infty} J^2_n(\beta)\ T^2\ (\omega_c + n\omega_s) \cos n\omega_s\tau. \qquad (32)$$

In Equation (32) it is seen that the function depends only on the amplitude characteristic of the i-f pass band. For a Chebishev-type characteristic with low ripple, $T(\omega_c + n\omega_s) \cong 1$ in the pass band.

Power Spectrum of Output

For the rectangular i-f of bandwidth B, the autocorrelation function for noise is

$$\rho(\tau) = \text{sinc}\ B\tau = \frac{\sin \pi B \tau}{\pi B \tau}, \qquad (33)$$

and its Fourier transform is

$$\rho(\tau) \longleftrightarrow \frac{1}{B} \text{rect} \frac{f}{B}, \qquad (34)$$

where

$$\text{rect}\ \frac{f}{B} = 1 \qquad \text{for} \qquad |f| < -\frac{B}{2}$$

$$= 0 \text{ otherwise.}$$

The terms in Equation (32) will be of the type $\rho(\tau) \cos n\omega_s\tau$ and $\ddot{\rho}(\tau) \cos n\omega_s\tau$; these have the Fourier mates

$$\rho(\tau) \cos n\omega_s\tau \longleftrightarrow \frac{1}{2B}\left[\text{rect}\ \frac{f - nf_s}{B} + \text{rect}\ \frac{f + nf_s}{B}\right] \qquad (35)$$

$$-\ddot{\rho}(\tau) \cos n\omega_s\tau \longleftrightarrow \frac{2\pi^2}{B}\left[(f - nf_s)^2\ \text{rect}\ \frac{f - nf_s}{B} + (f + nf_s)^2\ \text{rect}\ \frac{f + nf_s}{B}\right] \qquad (36)$$

The spectrum for the signal-cross-noise terms becomes

$$S_{s\times n}(f) = \sigma^2 BE^2_s \sum_{n=-\infty}^{\infty} J^2_n(\beta)\ (n\omega_s)^2 \frac{1}{2B}\left[\text{rect}\frac{f-nf_s}{B} + \text{rect}\frac{f+nf_s}{B}\right]$$

$$+ \sigma^2 BE^2_s \sum_{n=-\infty}^{\infty} J^2_n(\beta) \frac{2\pi^2}{B}\left[(f-nf_s)^2 \text{rect}\frac{f-nf_s}{B}\right.$$

$$\left. + (f+nf_s)^2 \text{rect}\frac{f+nf_s}{B}\right]. \qquad (37)$$

Since the modulating frequency f_s is much smaller than the system bandwidth B, the shifted rectangular functions will overlap. In the case of no carrier shift, all terms will contribute in the audio frequency range of interest. Under these conditions

$$\text{rect}\frac{f-nf_s}{B} + \text{rect}\frac{f+nf_s}{B} = 2, \qquad (38)$$

and

$$S_{s\times n}(f) = 4\pi^2 \sigma^2 E^2_s \sum_{n=-\infty}^{\infty} J^2_n(\beta)\ [f^2 + 2n^2 f_s^2]. \qquad (39)$$

Using the relations[4]

$$\sum_{n=-\infty}^{\infty} J^2_n(\beta) = 1, \qquad (40)$$

$$\sum_{n=-\infty}^{\infty} n^2 J_n^2(\beta) = \frac{\beta^2}{2}, \qquad (41)$$

the signal-cross-noise spectrum reduces to

$$S_{s\times n}(f) = 4\pi^2 \sigma^2 E^2_s (f^2 + \beta^2 f_s^2). \qquad (42)$$

The spectrum corresponding to the noise-cross-noise correlation function given by Equation (25) can be expressed as the Fourier pair

[4] G. N. Watson, *A Treatise on the Theory of Bessel Functions*, Cambridge University Press, 1958, p. 37.

$$-2\sigma^4 B^2 [\rho(\tau)\ \ddot{\rho}(\tau) - \dot{\rho}^2(\tau)] \leftrightarrow 8\pi^2\sigma^2 \left[f^2 \operatorname{rect}\frac{f}{B} * \operatorname{rect}\frac{f}{B} - f \operatorname{rect}\frac{f}{B} * f \operatorname{rect}\frac{f}{B} \right] = \frac{4}{3}\pi^2\sigma^4 B^3 \left[1 - \frac{|f|}{B} \right]^3 \tag{43}$$

where * indicates convolution. The total output spectrum including the signal and noise-cross-noise terms is then

$$S(f) = \pi^2\beta^2 f_s^2 k_0^2 E_s^4 [\delta(f - f_s) + \delta(f + f_s)] + 4\pi^2\sigma^2 E_s^2 (f^2 + \beta^2 f_s^2) + \frac{4}{3}\pi^2\sigma^4\beta^3 \left(1 - \frac{|f|}{B} \right)^3 \tag{44}$$

where $k_0 E^2_1$ is the average signal envelope amplitude after passing through detector (see Appendix II).

Effect of Carrier Offset

When the carrier frequency is offset from the center of the passband, the complex envelope can be represented by

$$\begin{aligned} E &= (u + jv) \exp\{j\delta_s t\} \\ &= u \cos \delta_s t - v \sin \delta_s t + j(v \cos \delta_s t + u \sin \delta_s t) \\ &= u_1 + jv_1 , \end{aligned} \tag{45}$$

where u and v are as defined in Equation (4) and δ_s is the carrier offset. Using the quantities

$$u_1 = u \cos \delta_s t - v \sin \delta_s t, \tag{46}$$

$$\dot{u}_1 = (\dot{u} - v\delta_s) \cos \delta_s t - (\dot{v} + u\delta_s) \sin \delta_s t, \tag{47}$$

$$v_1 = v \cos \delta_s t + u \sin \delta_s t, \tag{48}$$

$$\dot{v}_1 = (\dot{v} + u\delta_s) \cos \delta_s t + (\dot{u} - v\delta_s) \sin \delta_s t, \tag{49}$$

the signal-cross-noise autocorrelation function corresponding to Equation (32) can be expressed as

$$R_{s\times n}(\tau) = \sigma^2 B E_s^2 \cos \delta_s \tau \, \rho(\tau) \sum_{n=-\infty}^{\infty} J_n^2(\beta) \, T^2 (\omega_c + n\omega_g) \, [(n\omega_s)^2 + \delta_s^2] \cos n\omega_g \tau$$

$$- \sigma^2 B E_s^2 \cos \delta_s \tau \, \dot{\rho}(\tau) \sum_{n=-\infty}^{\infty} J_n^2(\beta) \, T^2 (\omega_c + n\omega_s) \cos n\omega_g \tau. \quad (50)$$

Power Spectrum of Output for Shifted Carrier

Taking the Fourier transform of Equation (50), the spectrum of the signal-cross-noise term becomes

$$S_{s\times n}(f) = \frac{1}{4} \sigma^2 E_s^2 \sum_{n=-\infty}^{\infty} J_n^2(\beta) \left\{ [(n\omega_g)^2 + \delta_g^2] \left[\text{rect} \frac{f - \zeta_s + nf_g}{B} \right.\right.$$

$$\left.\left. + \text{rect} \frac{f + \zeta_s - nf_g}{B} + \text{rect} \frac{f - \zeta_g - nf_s}{B} + \text{rect} \frac{f + \zeta_s + nf_s}{B} \right] \right\}$$

$$+ \pi^2 \sigma^2 E_s^2 \sum_{n=-\infty}^{\infty} J_n^2(\beta) \left[(f - \zeta_s + nf_s)^2 \, \text{rect} \frac{f - \zeta_s + nf_s}{B} \right.$$

$$+ (f + \zeta_s - nf_s)^2 \, \text{rect} \frac{f + \zeta_s - nf_s}{B} + (f - \zeta_s - nf_s) \, \text{rect} \frac{f - \zeta_s - nf_s}{B}$$

$$\left. + (f + \zeta_g + nf_s)^2 \, \text{rect} \frac{f + \zeta_s + nf_s}{B} \right]. \quad (51)$$

where ζ_s is the frequency $\delta_s/(2\pi)$. In the derivation of Equation (51) it has been assumed that the band-pass characteristic for noise is rectangular.

If all overlapping channels are included, the signal-cross-noise spectrum can be written

$$S_{s\times n}(f) = 4\pi^2 \sigma^2 E_s^2 (f^2 + 2\zeta_s^2 + \beta^2 f_s^2). \quad (52)$$

Equation (52) represents a worst case if it is used to calculate the signal-cross-noise power for values of carrier offset large enough to cause truncation of the spectral sidebands.

When the carrier shift is such that some of the significant sidebands are truncated by the i-f characteristic, the form of the spectral function will depend on the particular value of the carrier shift, the i-f bandwidth, the modulation index, and the frequency. Assuming

the conditions

$$f_s = 3 \text{ kHz}$$
$$B = 77 \text{ kHz}$$
$$\zeta_s = 27 \text{ kHz}$$
$$\beta = 6,$$

the spectrum is

$$S_{s\times n}(f) = 4\pi^2 \sigma^2 E_x^2 \left\{ \sum_{n=-3}^{21} J_n^2(\beta) \left[2(n^2 f_x^2 + \zeta_x^2) + f^2 - 2nf_x\zeta_x \right] \right.$$
$$\left. + \sum_{n=4}^{5} J_n^2(\beta) \left[n^2 f_x^2 + \zeta_x^2 + \frac{1}{2} f^2 + nf_x\zeta_x \right] \right\} \tag{53}$$

The total output spectrum including all signal and noise terms for the case where all signal-cross-noise terms are included is given by

$$S(f) = \pi^2\beta^2 f_x^2 k_n^2 E_x^4 \left[\delta(f - f_x) + \delta(f + f_x) \right]$$
$$+ 4\pi^2\sigma^2 E_x^2 (f^2 + 2\zeta_x^2 + \beta^2 f_x^2) + \frac{4}{3}\pi^2\sigma^4 B^3 \left(1 - \frac{|f|}{B} \right)^3. \tag{54}$$

Output Signal-to-Noise Ratio

If we assume an audio-signal pass band that is rectangular and of bandwidth B_x centered at frequency f_x, the power in the pass band is given by

$$P = \int_{-\infty}^{\infty} \left[\text{rect} \frac{f - f_x}{B_s} + \text{rect} \frac{f - f_x}{B_x} \right] S(f)\, df. \tag{55}$$

Using Equation (54) for the spectral function, the signal power is given by

$$P_x = 2\pi^2 \Delta f_x^2 k_n^2 E_x^4, \tag{56}$$

where

$$\Delta f_x = \beta f_x.$$

The power in the audio filter contributed by the signal-cross-noise terms, using Equation (52), will be

$$P_{s\times n} = \int_{-\infty}^{\infty} S_{s\times n}(f)\,df$$

$$= 8\pi^2\sigma^2 E_s^2 B_s \left[f_s^2 + 2\zeta_s^2 + \Delta f_s^2 + \frac{B_s^2}{12} \right]. \tag{57}$$

Since B_s is usually much smaller than f_s or Δf_s, the term $B_s^2/12$ can be dropped in most cases. The remaining term contributing to the output noise is due to the noise-cross-noise components; this results in a noise power

$$P_{n\times n} = \frac{8\pi^2\sigma^4 B^3}{3} \int_{f_s-(B_s/2)}^{f_s+(B_s/2)} \left(1 - \frac{f}{B}\right)^3 df.$$

$$= \frac{8}{3}\pi^2\sigma^4 B^3 B_s \left[\left(1 - \frac{f_s}{B}\right)^3 + \frac{B_s^2}{8B^2} - \frac{B_s^2 f_s}{4B^3} \right]$$

$$\simeq \frac{8}{3}\pi^2\sigma^4 B^3 B_s \left(1 - \frac{f_s}{B}\right)^3. \tag{58}$$

By using Equation (56), (57), and (58), the output signal-to-noise ratio can be written in the form

$$\frac{S}{N} = \frac{k_v^2 \left(\frac{C}{N}\right)^2}{2\frac{C}{N}\frac{B_s}{B}\left[1 + \frac{1}{\beta^2} + 2\frac{\zeta_s^2}{\Delta f_s^2}\right] + \frac{B\,B_s}{3\Delta f_s^2}\left(1 - \frac{f_s}{B}\right)}$$

where $C/N = E_s^2/2N$, and $N = \sigma^2 B$. (59)

In the derivation of Equation (59) it has been assumed that amplitude ripples in the pass band are small and the pass band is essentially rectangular. A comparison of the gaussian and rectangular band-pass characteristics with respect to S/N performance for low S/N is given in Appendix III. The amplitude reduction due to pass-band distortion of the signal function is determined by k_v as evaluated by harmonic

analysis of the signal after passing through filter and detector. The particular filter constants and characteristic used in this analysis is given in Appendix I, and the definition of k_o is given in Appendix II. Since all noise terms are included in the evaluation of Equation (59), the S/N ratio obtained would be worse than that obtained using Equation (53) for the detuned carrier case where some of the noise side-bands are truncated by the i-f characteristic.

In the case of low input carrier-to-noise ratios, the results given by Equation (59) will be fairly accurate for the detuned carrier case, since the contribution of the noise due to signal-cross-noise terms will be small compared with that due to the noise-cross-noise products. Under this condition most of the degradation in the output signal-to-noise ratio will be due to the decrease in signal power caused by carrier mistuning in the i-f pass band.

Extension of Results to Multiple Signals

In the multiple-signal case several (up to five in a particular system) carrier frequencies each with a different FM tone are received simultaneously and detected in the same detector. If the audio tones are chosen so that they are not harmonically related (prime numbers), they will not build up products that will result in a signal tone. In the signal-to-noise ratio equation, there will be additional signal-cross-noise terms although the noise-cross-noise term will be unchanged in form. Under this condition, the signal-to-noise ratio for the m^{th} tone is given by

$$\left(\frac{S}{N}\right)_m = \frac{k_{om}^2 \left(\frac{C}{N}\right)_m^2}{2\left(\frac{C}{N}\right)_m \frac{B_s}{B} \sum_{r=1}^{n} a_{rm}^2 \left(b_{rm}^2 + \frac{1}{\beta_m^2} + \frac{2}{\Delta f_m^2}\zeta_r^2\right) + \frac{BB_s}{3\Delta f_m^2}\left(1 - \frac{f_m}{B}\right)^3} \tag{60}$$

where $(C/N)_m = E_m^2/(2N)$, $a_{rm} = E_r/E_m$, $b_{rm} = \Delta f_r/\Delta f_m$ and k_{om} is the signal loss factor of the signal tone f_m.

The effect of bandwidth on the signal-to-noise ratio at the output of the system can be found by substituting $(C/N)\ (B_0/B)$ for (C/N) in Equation (60). This results in

$$\left(\frac{S}{N}\right)_m = \frac{\left(\frac{C}{N}\right)_m^2 \left(\frac{B_v}{B}\right)^2}{2\left(\frac{C}{N}\right)_m \frac{B_s B_v}{B^2} \sum_{r=1}^{n} a_{rm}^2 \left[b_{rm}^2 + \frac{1}{\beta_m^2} + \frac{\zeta_r^2}{\Delta f_m^2} \right] + \frac{BB_s}{3\Delta f_m^2} \left(1 - \frac{f_m}{B}\right)^3} \tag{61}$$

Equation (61) references the noise power to a system with bandwith B_v.

When all signals except the m^{th} are identical and the deviations made equal, so that $b_{rm} = 1$, Equation (60), for the $\zeta_r = 0$ case, reduces to

$$\left(\frac{S}{N}\right)_m = \frac{k_{om}^2 \left(\frac{C}{N}\right)_m^2}{2\left(\frac{C}{N}\right)_m \frac{B_s}{B}\left(1 + \frac{1}{\beta_m^2}\right)\left[1 + (n-1)a^2\right] + \frac{B_s B}{3\Delta f^2}\left(1 - \frac{f_m}{B}\right)^3}, \tag{62}$$

where $a = E_r/E_m$. In the analysis given above, a square-law detector characteristic has been used to simplify the analysis. The performance of a detection system using a linear detector is analyzed in Appendix IV for the case of two signals and noise when one of the signals is much larger than noise.

The signal-to-noise performance of the FM detection system in the presence of interfering signals can be presented in an alternative way. Equation (62) can be expressed in the form

$$Z = \frac{y^2}{K_1 y(1 + x) + K_2}, \tag{63}$$

where

$$y = (C/N)_m$$

$$x = na^2 = \frac{\text{interfering signal}}{\text{desired signal}},$$

$$K_1 = 2\frac{B_s}{B}\left(1 + \frac{1}{\beta_m^2}\right),$$

$$K_2 = \frac{BB_s}{3\Delta f^2}\left(1 - \frac{f_m}{B}\right)^3.$$

Contours of constant output S/N as a function of x and y can be determined if Equation (63) is solved for y in terms of x and z. This gives

$$y = \frac{1}{2}\left[K_1 z(1+x) + \{|K_1 z(1+x)|^2 + 4K_2 z\}^{1/2}\right]. \tag{64}$$

Calculated Results

Using Equation (60), the output signal-to-noise ratio has been calculated for various input carrier-to-noise ratios and system parameters. These results have been tabulated in Tables I and II for a typical set of system parameters and signal conditions. In this set of calculations, the carrier offsets ζ_r were assumed to be zero and the signal loss due to i-f distortion assumed to be zero ($k_{nm} = 1$). Table I shows a listing of the output signal-to-noise ratios as a function of the input carrier-to-noise ratio and of the number of additional signals present. The added signals in this case are at a level 10 db above the noise level. Table II shows the signal-to-noise ratio of the stronger signal corresponding to the conditions given in Table I. Figure 3 is a plot of the results given in Table I.

Figure 4 is a parametric plot illustrating the effect on the output S/N of i-f bandwidth and frequency deviation when the noise power density in the i-f is kept constant. These curves are plots of Equation (61) with $B_n = 100$ kHz, $n = 1$, $\zeta_r = 0$ and $C/N = -15$ db. The corresponding curves for the case where there is an interfering signal 20 db higher than the desired signal is shown in Figure 5. A family of curves of output signal-to-noise ratio as functions of the input carrier-to-noise ratio as computed using Equation (64) is shown in Figure 6. Curves such as these can be used as an aid in determining an optimum set of parameters for a particular system.

The effect of i-f amplitude and phase distortion of the signal is reflected in the value of the signal loss factor k_n. Two factors cause a loss in signal: (1) a decrease in the modulation index and (2) a decrease in the average envelope amplitude. As seen in the analysis,

Table I—Performance Characteristics of Square-Law Detection System

Input C/N Ratio	Output-Signal-to-Noise Ratio $(S/N)_1$				
$(C/N)_1$ (db)	One Signal Plus Noise (db)	Two Signals Plus Noise (db)	Three Signals Plus Noise (db)	Four Signals Plus Noise (db)	Five Signals Plus Noise (db)
—15	3.7	— 4.5	— 7.2	— 8.8	— 10.0
—10	13.5	5.4	2.8	1.1	0.0
— 5	23.1	15.4	12.7	11.1	9.9
0	31.8	25.1	22.6	21.0	19.9
+ 5	39.3	34.4	32.2	30.8	29.7
+10	45.5	42.8	41.1	40.0	39.0

$f_1 = 1000$ Hz $\quad B_v = 6$ Hz $\quad B = 50$ kHz $\quad \Delta f = 15$ kHz $\quad .03162 \leq (C/N)_1 \leq 10$ $\quad (C/N)_k = 10,\ k = 2, 3, 4, 5$

Table II—Signal-to-Noise Ratio of Stronger Signal

$(C/N)_1$ (db)	Output-Signal-to-Noise Ratio $(C/N)_2$			
	Two Signals Plus Noise (db)	Three Signals Plus Noise (db)	Four Signals Plus Noise (db)	Five Signals Plus Noise (db)
—10	45.4	42.8	41.1	40.0
+10	42.8	41.2	40.0	39.0

$f_2 = 1210$ Hz $\quad B_v = 6$ Hz $\quad B = 50$ kHz $\quad \Delta f = 15$ kHz $\quad (C/N)_k = 10$ $\quad k = 2, 3, 4, 5$

after passage through square-law detection, the signal component is proportional to the product of the square of the envelope and the detected modulation. Assuming a 4-pole Chebishev band-pass filter with 1 db ripple as given in Appendix I, the instantaneous frequency

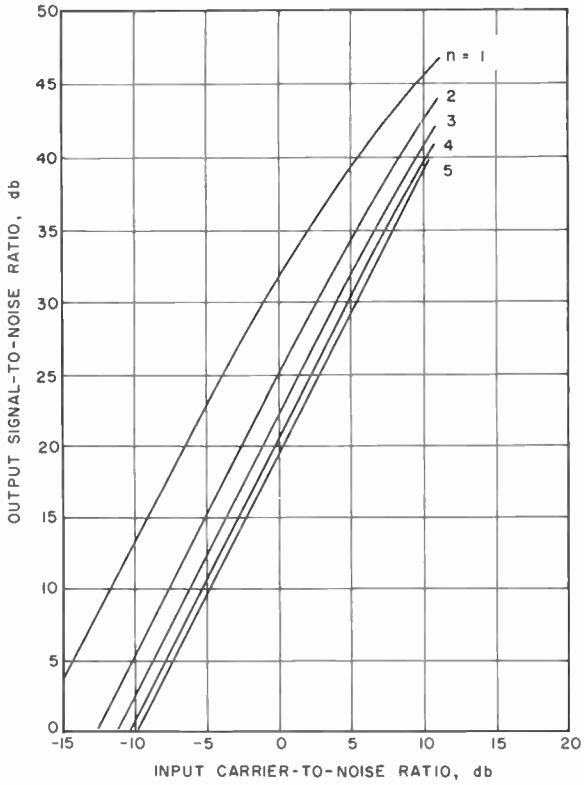

Fig. 3—Output S/N versus input C/N as a function of n, the number of signals: $B = 50$ kHz, $\Delta f = 15$ kHz, $f_1 = 1$ kHz, $B_s = 6$ Hz, $(C/N)_k = +10$ db, and $k = 2, 3, 4, 5$.

ω_i and envelope E (derivative of phase and magnitude of Equation (5), respectively) were calculated for various carrier offsets. A harmonic analysis was made of the quantity $(E^2\omega_i)$ to determine the fundamental component. The value of k_a is the normalized fundamental amplitude and is tabulated in Table III. Using Equation (59) and Table III, the output signal-to-noise ratio has been calculated for the case of a single signal with various amounts of carrier detuning. These results are given in Table IV. Since all signal-cross-noise terms have been included in this computation, the high carrier-to-noise cases with large

Table III—Signal Loss Factor (1-db ripple filter)

ζ_1 (kHz)	k_0	k^2_0	$-10 \log k^2_0$ (db)
0	1.000	1.000	0
9	.892	.801	.96
18	.835	.697	1.57
27	.600	.360	4.44
36	.474	.225	6.48

carrier offsets will be slightly pessimistic. For the weak-signal case the results will not be affected noticeably by inclusion of all signal-cross-noise terms since their contribution is small compared to the noise-cross-noise term.

Conclusions

The important theoretical performance characteristics of a multiple-signal FM detection system have been determined as an aid in

Table IV—Calculated S/N Ratios as Function of Carrier Offset ζ and Input C/N

ζ_1 (kHz)	C/N (db)			
	−15	−10	0	+10
0	5.5	15.4	34.1	48.7
9	4.5	14.3	32.6	46.3
18	3.8	13.5	30.7	43.1
27	1.8	10.3	26.2	37.8
36	−1.4	7.8	22.7	33.7

System Parameters $B = 77$ kHz, $f = \Delta 18$ kHz, $B_s = 4$ Hz, $f_s = 3$ kHz

the design of a practical system. Equations for the output signal-to-noise ratio have been derived as functions of the various system parameters such as i-f bandwidth, frequency deviation, signal frequency, and audio filter bandwidth. The single-signal and multiple-signal signal-to-noise ratios are shown as functions of the input carrier-to-

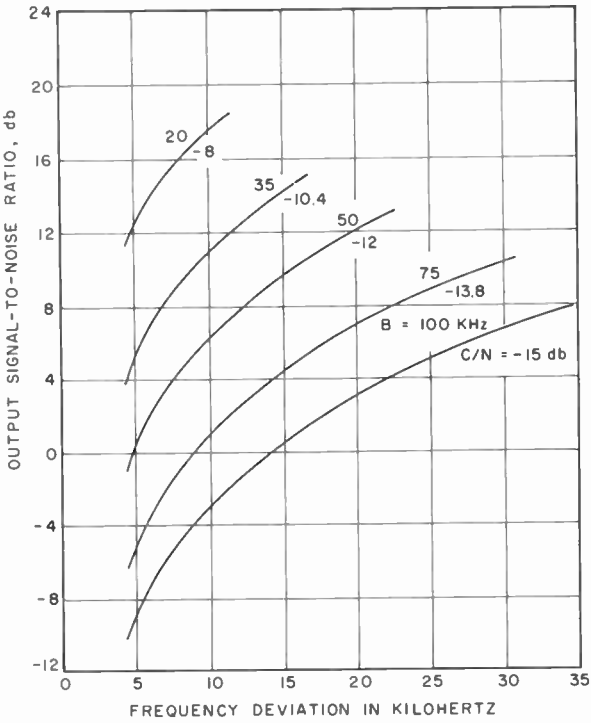

Fig. 4—Output S/N versus frequency deviation as a function of system bandwidth, one signal plus noise (constant noise power density in i-f): $B_v = 6$ Hz, $f_1 = 1$ kHz.

noise ratio. These illustrate the signal-suppression effect of the detection system and indicate the usable dynamic range of a given system. Effect of non-ideal filters and carrier offset on the system performance has also been shown.

Acknowledgments

The author acknowledges the contributions made to the study through discussions with F. Assadourian, A. Axelrod, and G. Lieberman.

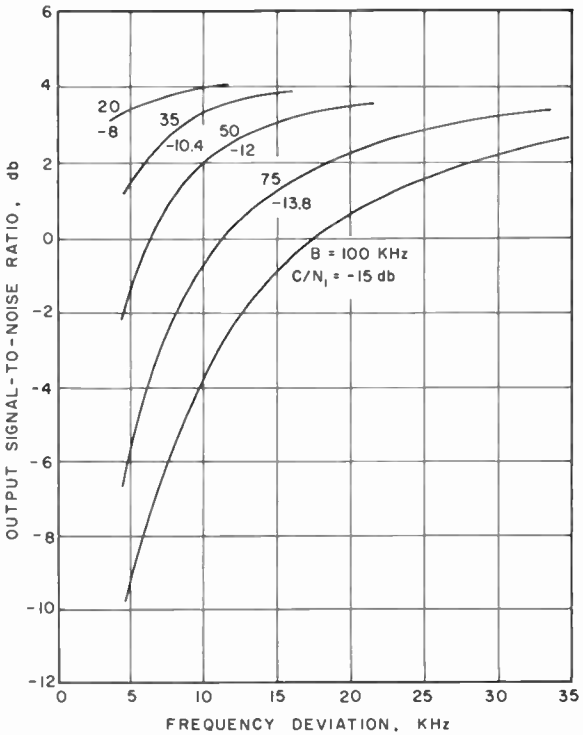

Fig. 5—Output S/N versus frequency deviation as a function of system bandwidth for two signals plus noise (constant noise power density in i-f): $B_v = 6$ Hz, $f_1 = 1$ kHz, $(C/N)_2 = (C/N)_1 + 20$ db.

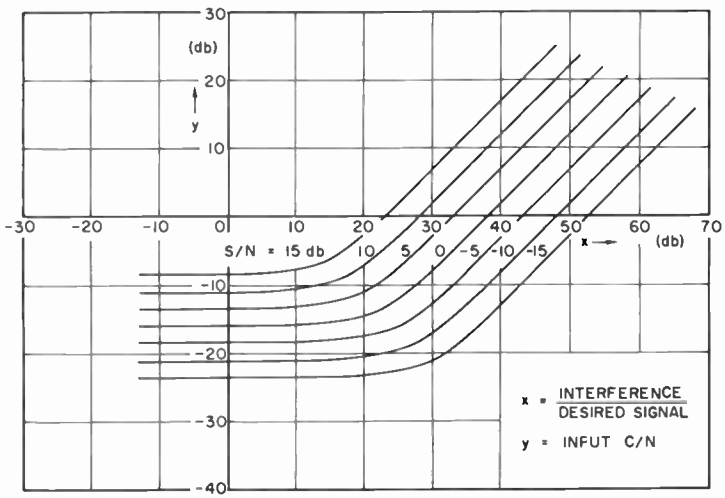

Fig. 6—Output S/N as a function of input C/N and interfering signal: $B = 75$ kHz, $B_v = 6$ Hz, $\Delta f = 15$ kHz, and $f_1 = 1$ kHz.

Appendix I—Circuit Element Values and Filter Transfer Function

Circuit Element Values

For a 4-pole filter with 1 db ripple the attenuation characteristics are 25 db at 127 kHz and 56 db at 254 kHz, where the indicated frequencies are measured from the filter center frequency. The element values for the series representation of the Chebishev filter shown in Figure 7 can be determined[5] and are

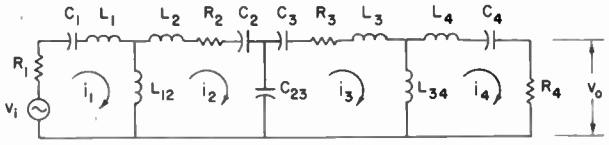

Fig. 7—Four-pole filter.

$$
\begin{aligned}
C_1 &= C_4 = 13.976604 \text{ pF},\\
C_2 &= C_3 = 14.027700 \text{ pF},\\
L_1 &= L_2 = L_3 = L_4 = 13.645568\ \mu\text{H},\\
L_{12} &= L_{34} = 0.0582915\ \mu\text{H},\\
C_{23} &= 3837.0770 \text{ pF},\\
R_1 &= R_4 = 3 \text{ ohms (arbitrary value)},\\
R_2 &= R_3 = 0.0872368 \text{ ohm},
\end{aligned}
$$

assuming a center frequency of 11.500 MHz.

Filter Transfer Function

The circuit equations from Figure 7 are

$$
\begin{aligned}
&i_1\left(R_1 + pL' + \frac{1}{pC_1}\right) - i_2 pL_{12} = V_i,\\
&-i_1 pL_{12} + i_2\left(R_2 + pL' + \frac{1}{pC_1}\right) - i_3\frac{1}{pC_{23}} = 0,\\
&-i_2\frac{1}{pC_{23}} + i_3\left(R_3 + pL' + \frac{1}{pC_1}\right) - i_4 pL_{34} = 0,\\
&-i_3 pL_{34} + i_4\left(R_4 + pL' + \frac{1}{pC_4}\right) = 0,
\end{aligned}
\qquad (65)
$$

[5] *Reference Data for Radio Engineers*, 4th Edition (Federal Handbook) p. 219.

where $L' = L_1 + L_{12}$. These equations can be solved to give

$$\frac{v_o}{v_i} = \frac{ap}{b_4p^4 + b_3p^3 + b_2p^2 + b_1p + b_o + \dfrac{b_{-1}}{p} + \dfrac{b_{-2}}{p^2}}, \tag{66}$$

where

$$\begin{aligned}
a &= L_{12}^2(R_1C_{23}),\\
b_4 &= L_{12}^4 - 2\beta^2L_{12}^2 + \beta^4,\\
b_3 &= 2\beta(R_1 + R_2)(\beta^2 - L_{12}^2),\\
b_2 &= \beta^2(R_1^2 + 4R_1R_2 + R_2^2) - 2R_1R_2L_{12}^2,\\
b_1 &= 2\beta R_1R_2(R_1 + R_2),\\
b_o &= R_1^2R_2^2 - (\beta_2/C_{23}^2),\\
b_{-1} &= 2\beta R_1/C_{23}^2,\\
b_{-2} &= R_1^2/C_{23}^2,\\
\beta &= L'\left(1 - \frac{\omega_o^2}{\omega^2}\right).
\end{aligned}$$

The corresponding amplitude and phase characteristics are

$$T(\omega) = a\omega\left[\left(b_4\omega^4 - b_2\omega^2 + b_o - \frac{b_{-2}}{\omega^2}\right)^2 + \left(-b_3\omega^3 + b_1\omega - \frac{b_{-1}}{\omega}\right)^2\right]^{-1/2} \tag{67}$$

and

$$\theta(\omega) = -\frac{\pi}{2} - \tan^{-1}\frac{-b_3\omega^3 + b_1\omega - \dfrac{b_{-1}}{\omega}}{b_4\omega^4 - b_2\omega^2 + b_0 - \dfrac{b_{-2}}{\omega^2}}, \tag{68}$$

respectively. A plot of Equations (67) and (68) is shown in Figure 8 for the evaluated circuit element values.

Appendix II—Determination of Signal Loss Factor

The normalized detected signal at the output of the discriminator from Equation (17) is given by

$$(e)_s = u\dot{v} - v\dot{u}, \tag{69}$$

where u, $\dot{u}$, v and $\dot{v}$ are defined in Equations (16) to (19). To evaluate the fundamental signal component from Equation (69) explicitly by substitution of u, v, and their derivatives is very involved. The fundamental component can be found by a harmonic analysis of Equation

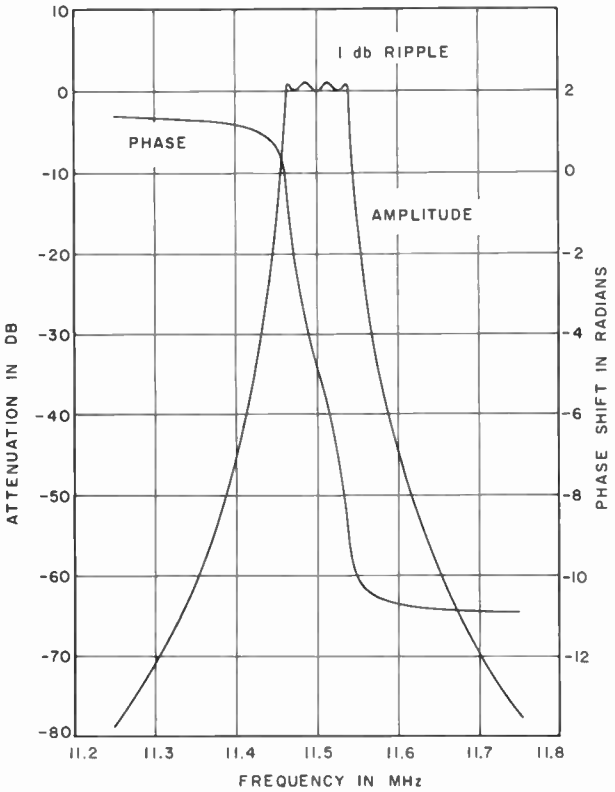

Fig. 8—Amplitude and phase characteristics of i-f filter.

(69). Since the instantaneous angular frequency of the complex envelope can be expressed as

$$\omega_i = \frac{d}{dt}\left(\tan^{-1}\frac{u}{v}\right) = \frac{u\dot{v} - v\dot{u}}{u^2 + v^2}, \tag{70}$$

and the corresponding instantaneous envelope as

$$E = [u^2 + v^2]^{1/2}, \tag{71}$$

the discriminator output for signal is seen to be

$$(e)_s = \omega_i(t) E^2(t). \tag{72}$$

The distorted instantaneous frequency and envelope when the carrier is offset 18 kHz in a 1-db pass band ripple filter is shown in Figures 9 and 10. The signal loss factor k_u is defined as

$$k_u = \frac{\text{fundamental of } (e_f)_s \text{ with carrier offset}}{\text{fundamental of } (e_u)_s \text{ with no offset}} \tag{73}$$

Appendix III—Comparison of Gaussian and Rectangular Band-Pass Functions for S/N

The effect of having a gaussian band pass in the i-f instead of the rectangular function assumed in the analysis upon the signal-to-noise ratio is examined. For a gaussian filter with a center frequency much greater than the filter bandwidth, the transfer function can be expressed as

$$H(f) = \exp\left\{ \frac{-\frac{1}{2}(f - f_u)^2 \ln 2}{\left(\frac{1}{2}B\right)^2} \right\} \tag{74}$$

Since $H(f_u) = 1$ and

$$H\left(f_u \pm \frac{1}{2}B\right) = \exp\left(-\frac{1}{2}\ln 2 \right).$$
$$= (2)^{-1/2}. \tag{75}$$

B is the 3-db bandwidth. The noise bandwidth is given by

$$B_N = \frac{1}{H^2(f_c)} \int_{-\infty}^{\infty} H^2(f)\, df$$
$$= \frac{1}{2}(\pi/\ln 2)^{1/2} B = 1.06\, B. \tag{76}$$

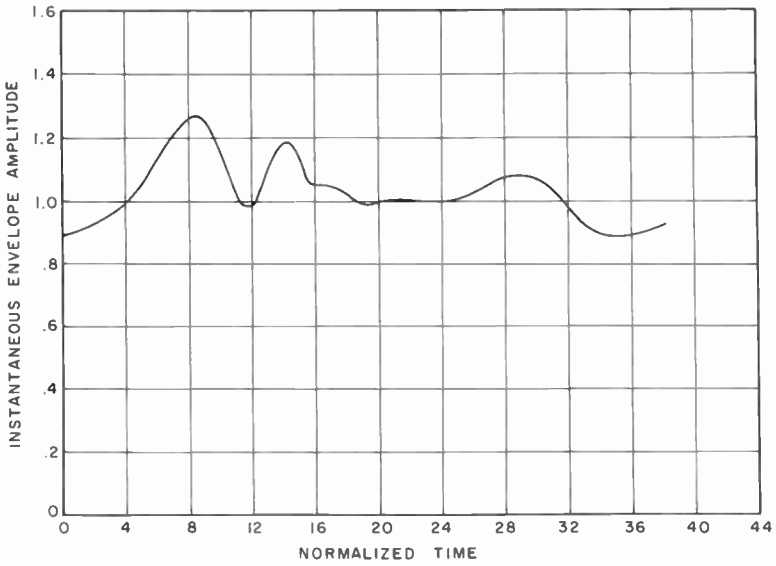

Fig. 9—Instantaneous angular frequency as a function of time: $f_c = 11.518$ MHz, $\zeta_1 = 18$ kHz, B = 77 kHz, and 1 db ripple.

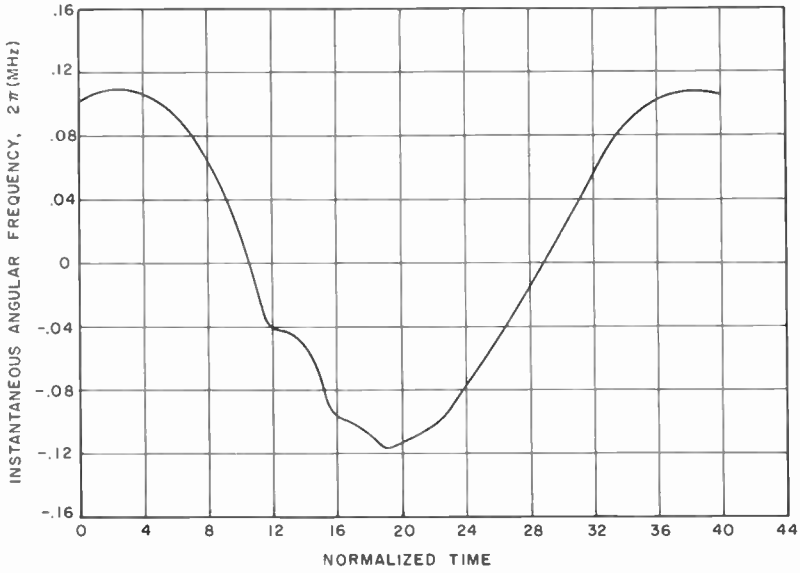

Fig. 10—Instantaneous envelope amplitude of discriminator output: $f_c = 11.518$ MHz, $\zeta_1 = 18$ kHz, $B = 77$ kHz, and 1 db ripple.

Autocorrelation Function

Since the transform of a gaussian function is also gaussian, a normalized autocorrelation function of the form $\exp(-\alpha^2\tau^2)$ has the transform relation

$$\rho(\tau) = \exp\left(-\alpha^2\tau^2\right) \longleftrightarrow \frac{\sqrt{\pi}}{\alpha} \exp\left(-\pi^2 f^2/\alpha^2\right). \tag{77}$$

In terms of the 3-db bandwidth B, the constant α is given by

$$\alpha = \pi B/(2\sqrt{\ln 2}). \tag{78}$$

For low signal-to-noise ratios, the largest term in the denominator of the S/N expression is the term arising from the noise-cross-noise products. The particular term in the autocorrelation function is given by

$$R_{n\times n}(\tau) = 2\sigma^4 B^2 \left[\dot{\rho}^2(\tau) - \rho(\tau)\,\ddot{\rho}(\tau)\right]. \tag{79}$$

When $\rho(\tau)$ is gaussian as in Equation (77),

$$\dot{\rho}(\tau) = -2\tau\alpha^2 \exp\left(-\alpha^2\tau^2\right) \tag{80}$$

$$\ddot{\rho}(\tau) = -2\alpha^2 \exp\left(-\alpha^2\tau^2\right) + 4\tau^2\alpha \exp\left(-\alpha^2\tau^2\right). \tag{81}$$

Using these relations in Equation (79) results in

$$R_{n\times n}(\tau) = 4\sigma^4 B^2\alpha^2 \exp\left(-2\alpha^2\tau^2\right). \tag{82}$$

The corresponding spectrum is then

$$4\sigma^4 B^2\alpha^2 \exp\left(-2\alpha^2\tau^2\right) \longleftrightarrow S_{n\times n}(f)$$
$$\longleftrightarrow 2\sqrt{2\pi}\,\sigma^4 B^2\alpha \exp\left[-\pi^2 f^2/(2\alpha^2)\right]. \tag{83}$$

Noise Power in Output Filter

The noise power in the narrow-band filter of width B_s centered at f_m is

$$P_{n\times n} = 2\int_{f_m - \frac{1}{2}B}^{f_m + \frac{1}{2}B} S_{n\times n}(f)\,df. \tag{84}$$

If we assume that $B_s \ll f_m$, this power can be approximated by

$$P_{n\times n} \cong 4\sqrt{2\pi}\sigma^4 B^2 B_s \alpha \exp\left[-\pi^2 f_m^2/(2\alpha^2)\right]. \tag{85}$$

Substituting the value of α as given by Equation (78) into (85) leads to the noise power

$$P_{n\times n} = \frac{2\sqrt{2\pi}\,\pi\,\sigma^4 B^3 B_s}{\sqrt{\ln 2}} \exp\left(-2(\ln 2) f_m^2/B^2\right). \tag{86}$$

If the modulation frequency is much smaller than the i-f bandwidth, the argument of the exponential in Equation (85) will be close to zero, so that

$$P_{n\times n} = 4\sqrt{2}\left(\frac{1}{2}\sqrt{\frac{\pi}{\ln 2}}\right)\sigma^4 B^3 B_s\,\pi. \tag{87}$$

If it is assumed that $N = \sigma^2 B$, where B is the 3-db bandwidth, then

$$(P_{n\times n})_{\text{gaussian}} = 4\sqrt{2}\,(1.06)\,\pi N^2 B B_s. \tag{88}$$

For the rectangular i-f filter, the corresponding noise power is (Equation (58) with $f_m \ll B$)

$$(P_{n\times n})_{\text{rect}} = (8/3)\,\pi^2 N^2 B B_s. \tag{89}$$

The ratio of these powers becomes

$$\frac{(P_{n\times n})_{\text{rect}}}{(P_{n\times n})_{\text{gaussian}}} = \frac{(8/3)\,\pi^2 N^2 B B_s}{4\sqrt{2}\,(1.06)\,\pi N^2 B B_s} = 1.395 \qquad (1.45 \text{ db}). \tag{90}$$

This means that the rectangular i-f assumption leads to S/N ratios for small signal conditions that are 1.45 db lower than for a gaussian i-f characteristic.

Using the equivalent noise bandwidth $B_N = 1.06\sigma B$ in the definition of the noise power N gives

$$N = 1.06\,\sigma^2 B. \tag{91}$$

The noise power for the gaussian case is then

$$(P_{n\times n})_{\text{gaussian}} = 4\sqrt{2}\,\pi N^2 BB_x^2 \cdot 1.06, \tag{92}$$

and the noise power ratio becomes

$$\frac{(P_{n\times n})_{\text{rect}}}{(P_{n\times n})_{\text{gaussian}}} = 1.57 \qquad (1.96 \text{ db}). \tag{93}$$

Appendix IV

Nonlimiting FM Detection System using Linear Detectors

The performance of the FM detection system when the square-law detectors shown in Figure 1 are replaced by linear envelope detectors is examined. To simplify the analysis, the case of two signals and noise where one of the signals is strong compared to the other and noise, is considered. If the complex envelope function given by Equation (5) is expressed in the polar form

$$u + jv = E \exp [\, j\theta(t)\,], \tag{94}$$

where

$$\theta(t) = \beta \sin \omega_2 t,$$

then the output of the envelope detector for two signals can be expressed as

$$\begin{aligned} |e_{a\pm}| = \frac{1}{2} \Big| & E_1^2 (1 \pm \epsilon_1)^2 + E_2^2 (1 \pm \epsilon_2)^2 + (x \pm k\dot{y})^2 + (y \mp k\dot{x})^2 \\ & + 2E_1 (1 \pm \epsilon_1)(x \pm k\dot{y}) \cos\theta_1 + 2E_2 (1 \pm \epsilon_2)(x \pm k\dot{y}) \cos\theta_2 \\ & + 2E_1 (1 \pm \epsilon_1)(y \mp k\dot{x}) \sin\theta_1 + 2E_2 (1 \pm \epsilon_2)(y \mp k\dot{x}) \sin\theta_2 \\ & + 2E_1 E_2 (1 \pm \epsilon_1)(1 \pm \epsilon_2) \cos(\theta_1 - \theta_2) \Big|^{1/2} \end{aligned} \tag{95}$$

where

$$\epsilon_1 = k\Delta\omega_1 \cos\omega_1 t$$
$$\epsilon_2 = k\Delta\omega_2 \cos\omega_2 t.$$

If it is assumed that E_1 is much larger than E_2 and the noise, then

$$\begin{aligned} e_{a\pm} \cong \frac{1}{2} \Bigg[& E_1 (1 \pm \epsilon_1) + \frac{E_2^2 (1 \pm \epsilon_2)^2}{2E_1 (1 \pm \epsilon_1)} + E_2 (1 \pm \epsilon_2) \cos(\theta_1 - \theta_2) \\ & + (x \pm k\dot{y}) \cos\theta_1 + (y \mp k\dot{x}) \sin\theta \Bigg] \end{aligned} \tag{96}$$

The output of the discriminator circuit becomes

$$e_d = E_1\epsilon_1 + \frac{E_2^2\epsilon_2}{E_1}(1 + \epsilon_1^2 + \epsilon_1^4 + \cdots) + E_2\epsilon_2 \cos(\theta_1 - \theta_2) + k\dot{y}\cos\theta_1 - k\dot{x}\sin\theta_1 . \quad (97)$$

If we assume offset carriers, the term $E_2\epsilon_2 \cos(\theta_1 - \theta_2)$ can be neglected. Also, the terms ϵ_1^2, ϵ_1^4 can be ignored if the modulating frequencies are prime numbers. The output is then

$$e_d = E_1\epsilon_1 + \frac{E_2^2\epsilon_2}{E_1} + k\dot{y}\cos\theta_1 - k\dot{x}\sin\theta_1 . \quad (98)$$

Using the previous method of analysis, the autocorrelation function is given by

$$\frac{1}{k^2}R(\tau) = \frac{1}{2}E_1^2\,\Delta\omega_1^2\cos\omega_1\tau + \frac{1}{2}\frac{E_2^4}{E_1^2}\Delta\omega_2^2\cos\omega_2\tau - \sigma^2 B\,\ddot{\rho}(\tau)\left[J_n^2(\beta_1) + 2\sum_{k=1}^{\infty} J_k^2(\beta_1)\cos k\omega_1\tau\right]. \quad (99)$$

The corresponding power spectrum is

$$\frac{1}{k^2}S(f) = \frac{1}{4}E_1^2\,\Delta\omega_1^2\left[\delta(f - f_1) + \delta(f + f_1)\right] + \frac{1}{4}\frac{E_2^4}{E_1^2}\Delta\omega_2^2\left[\delta(f - f_2) + \delta(f + f_2)\right] + 4\pi^2\sigma^2\left(f^2 + \frac{f_1^2\beta_1^2}{2}\right) \quad (100)$$

Output Signal-to-Noise Ratio

Integrating the power spectrum over the proper pass bands, the output signal-to-noise ratios at f_1 and f_2 are

$$\left(\frac{S}{N}\right)_1 = \frac{(C/N)_1}{\frac{B_n}{B}\left(1 + \frac{2}{\beta_1^2}\right)} \quad (101)$$

and

$$\left(\frac{S}{N}\right)_2 = \frac{a_{21}^2\,(C/N)_2}{\frac{B_s}{B}\left(\frac{\beta_1}{\beta_2}\right)^2\left[\frac{f_1^2}{f_2^2}+\frac{2}{\beta_1^2}\right]} \tag{102}$$

Comparison with the Quadratic Detector

The equations corresponding to (101) and (102) for a system using quadratic detectors are given by

$$\left(\frac{S}{N}\right)_1 = \frac{(C/N)_1}{2\,\frac{B_s}{B}\left(1+\frac{1}{\beta_1^2}\right)} \tag{103}$$

and

$$\left(\frac{S}{N}\right)_2 = \frac{a_{21}^2\,(C/N)_2}{2\,\frac{B_s}{B}\left(1+\frac{1}{\beta_2^2}\right)} \tag{104}$$

when $(C/N)_1$ is large so that the signal-cross-noise term is much larger than the noise-cross-noise term and $\Delta f_1 = \Delta f_2$. These results show that for the case of one strong signal and one weak signal in noise, the linear detector will result in a 3-db improvement over the system using a square-law detector. The factor $a_{21}^2 = E_2^2/E_1^2$ shows that there are signal suppression effects in both cases.

Correction

In the paper entitled "Analysis of Noncoherent FSK Systems with Large Ratios of Frequency Uncertainty," by A. B. Glenn, which appeared in the June 1966 issue of RCA Review, the author inadvertently neglected to acknowledge significant contributions of J. W. Modestino of the AVCO Corporation, Wilmington, Mass. His contributions were primarily in the analyses of linear and square-law detectors for binary FSK.

RCA Technical Papers

Second Quarter, 1966

Any request of copies of papers listed herein should be addressed to the publication to which credited.

"The Air Force Eastern Test Range Real-Time Telemetry Data System," H. W. Trigg, *Trans. IEEE PTGCOM* (April) 1966

"Atmospheric-Noise FSK Error Probabilities for an Envelope-Detection Receiver," H. E. White, *Trans. IEEE PTGCOM* (April) 1966

"Dislocations and Precipitates in GaAs Injection Lasers," M. S. Abrahams and C. J. Buiocchi, *Jour. Appl. Phys.* (April) 1966

"Display and Storage Tubes," M. D. Harsh, *Electronic Industries* (April) 1966

"Effect of Higher Absorption in Non-Lasing GaAs Diodes at 300°K," T. Gonda, M. F. Lamorte, P. Nyul, and H. Junker, *IEEE Jour. Quantum Electronics* (April) 1966

"Electrical Conductivity of 0-2 Monolayers of Cesium on Sapphire at 77°K," J. D. Levine, *Jour. Appl. Phys.* (Communications) (April) 1966

"A Goal: Spurious-Signal Immunity of Solid-State AM/FM Tuners," R. V. Fournier, C. H. Lee, and J. A. Kuklis, *Trans. IEEE PTGBTR* (April) 1966

"Lateral Traveling Solvent Growth in Indium Arsenide," H. P. Kleinknecht, *Jour. Appl. Phys.* (April) 1966

"Low-Energy Proton Bombardment of GaAs and Si Solar Cells," J. J. Wysocki, P. Rappaport, E. Davison, and J. J. Loferski, *Trans. IEEE PTGED* (April) 1966

"On the Mechanization of Creative Processes," S. Amarel, *IEEE* (April) 1966

"A Note Regarding the Dishal Method of Adjusting Multiple-Resonant-Circuit Filters," J. H. Pratt, *Proc. IEEE* (Letters) (April) 1966

"Parametric Amplification with Superconducting Films," P. Bura, *Proc. IEEE* (Letters) (April) 1966

"A Speech Channel Evaluation Divorced from Talker-Listener Influence," B. E. Keiser and Coauthor, *Trans. IEEE PTGCOM* (April) 1966

"Photoemission of Electrons from Silicon and Gold into Silicon Dioxide," A. M. Goodman, *Phys. Rev.* (15 April) 1966

"Theory and Observation of Intrinsic Surface States on Ionic Crystals," J. D. Levine and P. Mark, *Phys. Rev.* (15 April) 1966

"Parallel and Perpendicular Magnetic Transitions of Superconducting Films and Foils of Lead," G. D. Cody and R. E. Miller, *Phys. Rev. Letters* (18 April) 1966

"Single Component Changes Bandpass Into General Filter," R. Kurzrok, *Electronics* (April 18) 1966

"Radio-Frequency Resistance in the Mixed State for Subcritical Currents," J. I. Gittleman and B. Rosenblum, *Phys. Rev. Letters* (25 April) 1966

"Color Films for Color Telivision, Live Color Cameras, and Lighting for Color," H. N. Kozanowski, *Trans. IEEE PTGBTR* (May) 1966
"Comments on the NTSC System," G. H. Brown, *Trans. IEEE PTGBTR* (May) 1966
"Comments on the Special Issue," C. J. Hirsch, *Trans. IEEE PTGBTR* (May) 1966
"Large Wavelength Changes with Cavity Q in Injection Lasers," G. C. Dousmanis and D. L. Staebler, *Jour. Appl. Phys.* (May) 1966
"Lasers Can Do It Now," H. J. Watters, *Signal* (May) 1966
"Low-Energy Proton Damage in Partially Shielded Solar Cells," G. J. Brucker, W. Dennehy, A. G. Holmes-Siedle, and Co-author, *Proc. IEEE* (Proc. Letters) (May) 1966
"Physics Curricula and Industrial R & D or the Neglected 42%," J. Vollmer, *Amer. Jour. Phys.* (May) 1966
"Comment on 'Radiation Resistance of a Linear Current Filament in a Simple Anisotropic Medium,'" H. Staras, *Trans. IEEE PTGAP* (Communications) (May) 1966
"Spaceborne Transmitter for Direct Color Television Transmission from Satellites," J. D. Kiesling, *Trans. IEEE PTGBTR* (May) 1966
"Surface Layer of $BaTiO_3$," D. R. Callaby, *Jour. Appl. Phys.* (May) 1966
"Vacuum Evaporation of BAg_2Te," R. Dalven, *Jour. Appl. Phys.* (May) 1966
"New Target for Radar: Sharper Vision with Optics," A. J. Talamini, Jr. and E. C. Farnett, *Electronics* (Readers Comment) (May 30) 1966
"Analog-FM versus Digital-PSK Transmission," J. W. Whelan, *Trans. IEEE PTGCOM* (June) 1966
"Analysis of Noncoherent FSK Systems with Large Ratios of Frequency Uncertainties to Information Rates," A. B. Glenn, *RCA Review* (June) 1966
"Characteristics of Evaporated Antimony Films as a Function of the Antimony Source," A. H. Sommer, *Jour. Appl. Phys.* (June) 1966
"Color TV Tape Player, TR-3," M. C. Kirkas, *Broadcast News* (June) 1966
"Coupling Seismometers and Amplifiers for Maximum Signal-to-Noise Ratio," D. S. McCoy, *Trans. IEEE PTGGE* (June).. 1966
"Demodulator Threshold Performance and Error Rates in Angle-Modulated Digital Signals," J. Klapper, *RCA Review* (June) 1966
"The Effect of the Integrator-Dump Circuit on PCM/FM Error Rates," J. Klapper, *Trans. IEEE PTGCOM* (Correspondence) (June) 1966
"Encapsulated Germanium γ-Ray Spectrometers," P. P. Webb, R. M. Green, and Coauthors, *Trans. IEEE PTGNS* (June) 1966
"A Ferroelectric Field Effect Device," P. M. Heyman and G. H. Heilmeier, *Proc. IEEE* (June) 1966
"Field Effect Transistors Based on Silk Screened CdS Layers," W. Witt, F. Huber, and W. Laznovsky, *Proc. IEEE* (Letters) (June) 1966
"General Four-Resonator Filters at Microwave Frequencies," R. M. Kurzrok, *Trans. IEEE PTGMTT* (Correspondence (June) .. 1966
"The Generalized Transfer Function and Pole-Zero Migrations in Switched Networks," A. Acampora, *RCA Review* (June) ... 1966
"The IC Comes to TV," G. F. Corne, Jr., *Radio-Electronics* (June).. 1966
"The Langmuir Current Limit for Differing Axial and Radio Electron-Beam Temperatures in High-Resolution Image Devices," J. Lurie, *RCA Review* (June) 1966
"Low-Energy Proton Irradiation of Coated and Uncoated Thin-Film CdS and Single-Crystal Si Solar Cells," G. J. Brucker, W. L. C. Hui, and G. T. Noel, *Proc. IEEE* (Letters) (June) 1966
"Measurements of Magnetostrictive Coefficients by Means of an Optical Diffraction Technique," H. Weinstein, *Trans. IEEE PTGMAG* (June) 1966

"Microwave Generation from Photoconductive Mixing of Amplified Spontaneous Radiation," M. C. Steele, *RCA Review* (June). 1966
"Microwave Power Generation Using Overlay Transistors," H. C. Lee, *RCA Review* (June) 1966
"Multiple-Access Considerations for Communication Satellites," F. Assadourian and D. L. Jacoby, *RCA Review* (June) 1966
"Orientation Effect in GaAs Injection Lasers," M. S. Abrahams and J. I. Pankove, *Jour. Appl. Phys.* (June) 1966
"Performance of a Photomultiplier with a Porous Transmission Dynode," H. M. Smith, J. E. Ruedy, and G. A. Morton, *Trans. IEEE PTGNS* (June) 1966
"Thermal and Electrical Transport in InAs-GaAs Alloys," E. F. Hockings, I. Kudman, T. E. Seidel, C. M. Schmelz, and E. F. Steigmeier, *Jour. Appl. Phys.* (June) 1966
"Two San Juan TV Stations Share Same Superturnstile Antenna," B. K. Kellom, *Broadcast News* (June) 1966
"Vortexes Are Creating a Stir in the Superconductor Field," J. Pearl, *Electronics* (June 13) 1966
"Required Reading," V. E. Hills, *Electronics* (Readers Comment) (June 27) 1966

AUTHORS

MARTIN CAULTON received the Bachelor's degree in 1950, the M.S. in 1952, and the Ph.D. degree in 1954, all in Physics, from Rensselaer Polytechnic Institute. He was an instructor in Physics from 1950 to 1953 while at Rensselaer, and did part of his doctoral work at the Brookhaven National Laboratories, in high-energy nuclear physics, where he was research associate from 1953 to 1954. From 1954 to 1955 he was a Fullbright scholar at the Imperial College of Science and Technology in London. From 1955 to 1958 he was a member of the Technical Staff at Bell Telephone Laboratories working in research and development on low-noise microwave tubes. In 1958 he became assistant professor of physics at Union College, Schenectady, New York. Since joining RCA Laboratories in 1960, he has been engaged in work on microwave power tubes, multivelocity flow problems in electron beams, and microwave solid-state devices. Dr. Caulton is co-author of a textbook on physical electronics and is also adjunct professor of electrical engineering at Drexel Institute of Technology.

FRANK J. FEYDER received the B.S. degree in Electrical Engineering in 1955 from Newark College of Engineering. He joined RCA in 1947 and served in various assignments while attending evening classes at Newark College of Engineering. In 1953, he transferred into the Test Engineering department where he was responsible for the Qualification Approval program on military tube types, worked on testing problems, and prepared specifications on industrial and premium tube types. In 1958, Mr. Feyder became Engineering Leader in the Test Engineering Department where he was responsible for both electrical and environmental testing on Industrial, Military and Premium tube types. In January 1962, he was transferred as Engineering Leader into the Industrial Tube Application Laboratory and later the Nuvistor Development Department. In his present position, Mr. Feyder is responsible for Qualification Approval and military specifications on receiving tubes, the Measurement Standards Laboratory for tubes, and the Semiconductor Engineering Life Test unit.

Mr. Feyder is a member of the Institute of Electrical and Electronics Engineers.

HAROLD M. FINN received the BEE degree from the City College of N. Y. 1950, the M.S. degree in E.E. from the University of Maryland in 1955, and the Ph.D. degree from the University of Pennsylvania in 1965. Since 1950, Dr. Finn has been engaged in research and development of industrial control, radar, and communications systems while employed at the Engineering and Research Corp., Melpar, and the Emerson Research Laboratories. He joined the Missile and Surface Radar Division of RCA in 1959 where he is engaged in the development and application of signal detection theory. Dr. Finn is a member of Tau Beta Pi, Eta Kappa Nu, and is a senior member of the Institute of Electrical and Electronics Engineers.

JOHN J. HUGHES joined ITT Federal Laboratories in 1950, where he worked in the Chemical, Countermeasures, Microwave Tube Departments. From 1958 to 1961 he was assigned to Associated Testing Laboratories as a representative of ITT, working on environmental testing of microwave tubes. In 1962 he joined RCA Electronic Components and Devices, Harrison, New Jersey, where he was a production foreman in the Microwave Tube Division. In 1963 he joined RCA Laboratories, Princeton, N. J., where he has worked on plasma tube studies, klystron design and integrated solid-state microwave techniques. Mr. Hughes is a member of the Institute of Electrical and Electronics Engineers. He attended the 7th Army Electronics School in Germany and is presently taking courses at Fairleigh Dickinson University.

R. E. JOHNSON (See *RCA Review*, Vol. XXVII, March 1966, p. 172.)

ROBERT S. JOHNSON received his B.S. degree in mathematics in 1950 and his M.S. degree in mathematics in 1951, both from Northwestern University. In 1953, he joined the Institute for Cooperative Research at the University of Pennsylvania where he was assigned to projects BIGBEN and CARAMU. He received his Ph.D. degree in mathematics from the University of Pennsylvania in 1959. He joined RCA in 1959 as a numerical analyst and scientific programmer, and has worked primarily in the areas of orbital mechanics, optimization techniques, and systems simulation. He was responsible for the numerical analysis and programming of the PAGE, LEMIP, and EAST programs. He is a member of the American Mathematical Society and of S.I.A.M.